2013-09-24

Application of Field Performance Data in Developing Simple Analytical Models to Predict the Performance of Steam Assisted Gravity Drainage

Chan, Richard

UNIVERSITY OF CALGARY

Application of Field Performance Data in Developing Simple Analytical Models to Predict the Performance of Steam Assisted Gravity Drainage.

by

Richard Chan

A THESIS

SUBMITTED TO THE FACULTY OF GRADUATE STUDIES

IN PARTIAL FULFILMENT OF THE REQUIREMENTS FOR THE

DEGREE OF MASTER OF ENGINEERING

DEPARTMENT OF CHEMICAL AND PETROLEUM ENGINEERING

CALGARY, ALBERTA

SEPTEMBER, 2013

Abstract

A simple analytical model is developed in this paper to predict the performance of steam assisted gravity drainage (SAGD) operations. The oil drainage portion of the model is based on the work of Butler et al. (1981, 1998) to describe individual phases of SAGD operation. The steam consumption portion of the model builds on the work of various authors which include Reis (1992), Edmunds et al. (2007) and Miura et al. (2010), in which the various components of heat consumption within the reservoir are considered to determine steam injection requirements.

This model extends existing models presented in literature, and accurately parameterizes model inputs using lab measured data and field performance data (including 4D seismic). The model is validated with over 10 years of field performance data, which previously has not been possible over such a long time frame owing to the fact that SAGD is a relatively new technology.

Acknowledgements

The author would like to thank:

- His supervisor, Dr. Ian Gates for his guidance and mentorship throughout this project.
- Management and staff at Suncor Energy Inc. and AJM-Deloitte for their support.
- Frank Sun for his assistance with the seismic interpretation component of this study.

Table of Contents

List of Tables

List of Figures and Illustrations

List of Symbols, Abbreviations and Nomenclature

Symbol	Definition
a	Fraction of Total Heated Area
A	Overburden Area
A_{ob}	Area of Overburden Exposed to Steam
b	Cardwell and Parsons Permeability Exponent
B2	Butler Dimensionless Similarity Group
c	Exponential Constant For Overburden Area
c_o	Specific Heat Capacity of Oil
c_r	Specific Heat Capacity of Reservoir Sand
c_w	Specific Heat Capacity of Water
C_{vo}	Overburden Volumetric Heat Capacity
C_{vr}	Initial Reservoir Volumetric Heat Capacity
CSOR	Cumulative Steam Oil Ratio
f_{st}	Steam Quality
f_w	Fractional Flow of Water
g	Acceleration due to Gravity
h	Pay Thickness
h_s	Vertical Thickness of Steam Chamber
H_c	Heat Contained in Steam Chamber
H_{lv}	Latent Heat of Condensation of Steam
H_o	Cumulative Overburden Heat Loss
H_w	Sensible Heat of Water
H_∞	Cumulative Heat Loss to Semi Infinite Plane
K	Permeability
k_h	Effective Horizontal Permeability
k_o	Effective Oil Permeability
k_{ro}	Oil Relative Permeability
k_t	Reservoir Thermal Conductivity
$k_{t,ob}$	Overburden Thermal Conductivity
k_v	Effective Vertical Permeability
L	Well length
L_v	Latent Heat of Vaporization
m	Butler Viscosity Coefficient
M	Volumetric Heat Capacity
M_R	Reservoir Volumetric Heat Capacity
P	Pressure
q*	Dimensionless Flow Rate
q	Flow rate
q_{cum}	Cumulative Oil Production
q'_L	Heat Loss Rate to Overburden
q_r	Enthalpy Injection Rate to Preheat Reservoir

q_{sz}	Enthalpy Injection Rate to Maintain Steam Zone
Q	Cumulative Oil Production
Q_c	Cumulative Heat Ahead of Chamber
Q_L	Cumulative Heat Loss to Overburden
Q_r	Total Enthalpy Ahead of Steam Zone
S_l	Liquid Saturation
S_o	Oil Saturation
S_{oi}	Initial Oil Saturation
S_{or}	Residual Oil Saturation
t'	Butler Dimensionless Time Similarity Group
t^*	Dimensionless Time
T	Temperature
T^*	Dimensionless Temperature
T_R	Initial Reservoir Temperature
T_S	Steam Temperature
U	Average Steam Chamber Interface Velocity
u_m	Maximum Steam Chamber Interface Velocity
V_{sz}	Steam Zone Volume at Time t
W	Horizontal Distance to No Flow Boundary
w_s	Half Width of Steam Zone
x	Horizontal Position of Steam Chamber
y	Vertical Position of Steam Chamber
z	Distance Into Overburden
α	Thermal Diffusivity
β	Butler Fitting Factor For Rising Phase
β	Shape Factor for Miura Model
γ	Butler Shape Factor For Rising Phase
γ_o	Oil Specific Gravity (API)
ε	Perpendicular Distance from Chamber Interface
η	Cordinate Parallel to Steam/Oil Interface (Reis)
η_s	Reservoir Effective Sweep Efficiency
Θ	Chamber Interface Angle to Horizontal
λ	Time at Which Area 'a' is exposed (Edmunds)
μ	Dynamic Viscosity
μ_o	Oil Viscosity
μ_{os60}	Oil Viscosity at 60^{o}C below Steam Temperature
μ_w	Water Viscosity
ν	Kinematic Viscosity
ν_s	Kinematic Viscosity at Steam Temperature
ν_{os}	Kinematic Oil Viscosity at Steam Temperature
φ	Porosity
ρ_o	Oil Density
$\rho_{o,sc}$	Oil Viscosity at Standard Conditions
T	Time Since Steam Zone Reached Specified Width

CHAPTER 1: INTRODUCTION

1.1 Overview of Bitumen Resources and Steam Assisted Gravity Drainage

Alberta has one of the largest crude bitumen accumulations in the world (AER, 2012). The initial in-place resource of crude bitumen, defined by geological factors such as the porosity and oil saturation, was over 1.8 trillion barrels as of the end of 2011 (AER, 2012). Established reserves, in other words, the volume of bitumen capable of being recovered under current market economics and existing technology, are estimated to be roughly one-tenth of the total resource at 177 billion barrels. Of this volume, only 8.1 billion barrels has been produced to date. To make the reserves of bitumen relative to reserves of conventional oil versus the amount produced in 2011 more clear, the distribution is displayed in Figure 1.1.1.

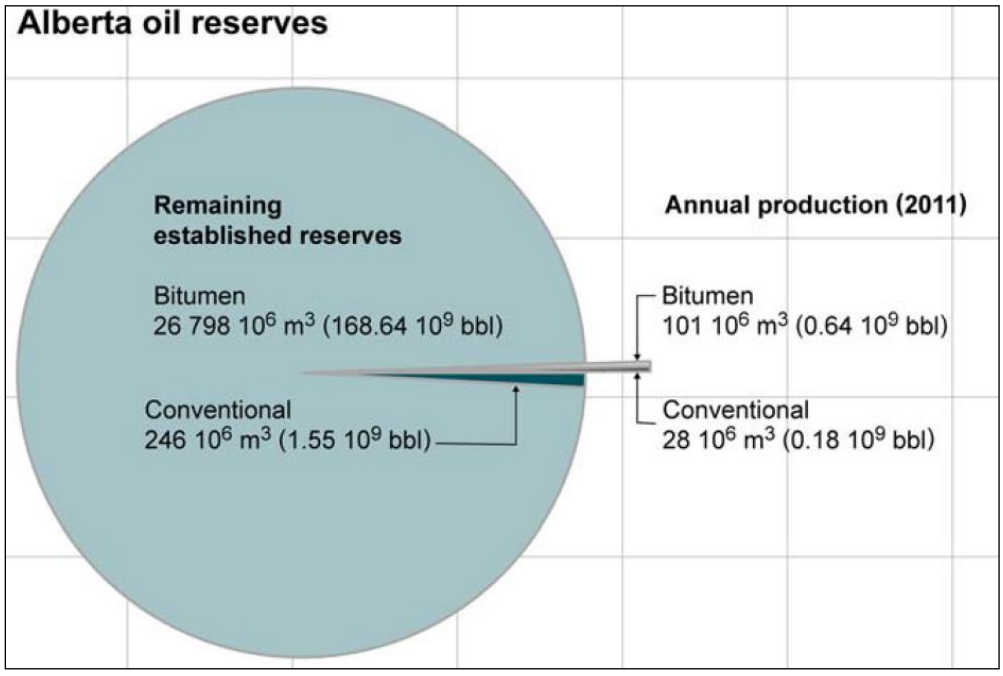

Figure 1.1.1: Comparison of Alberta bitumen to conventional oil reserves (courtesy of AER, 2012).

The oil sands area within Alberta is broken into three main areas: Peace River, Athabasca, and Cold Lake. Steam assisted gravity drainage (SAGD) is the preferred in situ technique used to recover bitumen for new projects in the Athabasca oil sands area. In this process, displayed schematically in Figure 1.1.2, two horizontal, parallel wells are used. The top well is the injection well which injects steam into the oil column whereas the bottom well is the production well through which mobilized oil and steam condensate flows from the reservoir to the surface.

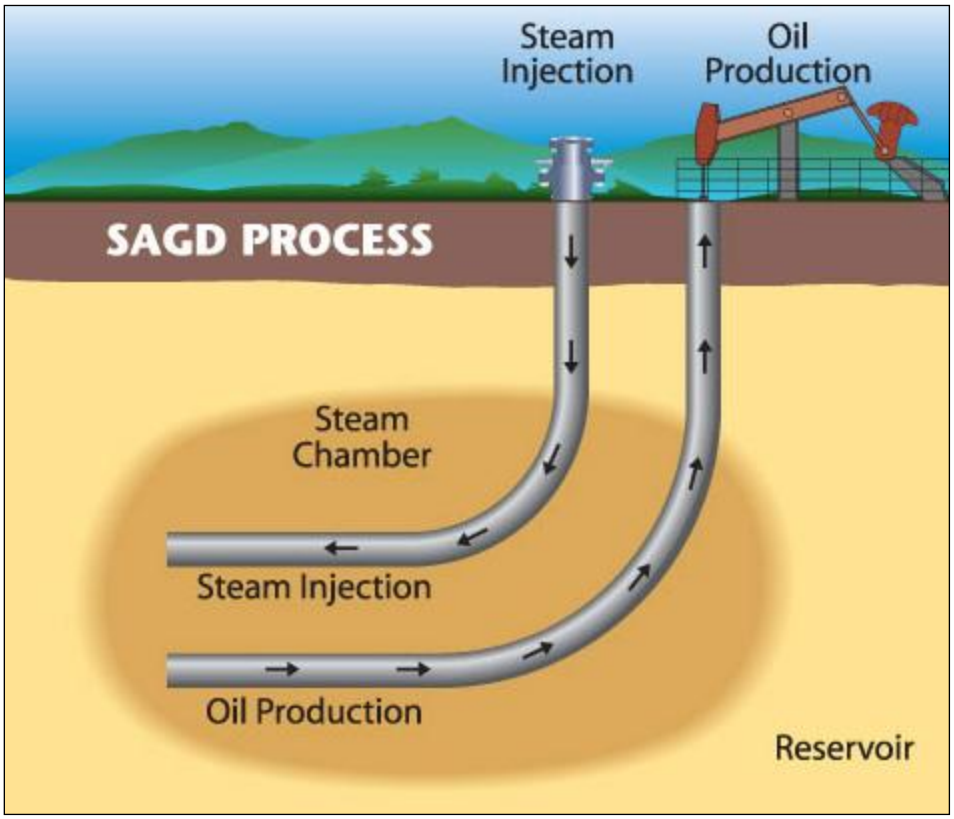

Figure 1.1.2: Schematic of the SAGD process (courtesy of The Oil Sands Developers Group, 2013).

The injected steam flows from the injection well to the outer edge of the steam chamber where it condenses and releases its latent heat to the oil sand at the chamber edge. The viscosity of the oil, which is typically over 1 million cP at original conditions, drops to less than 10 cP and can move through the reservoir under the action of gravity to the base of the steam chamber where the production well sits. Before fluids can be produced by the lower well, steam is typically injected into both the producer and injector well to establish communication and oil mobility between the wells.

The basic concept of SAGD is based on steam rise and the fall of heavier fluids (oil and steam condensate). As steam is continuously injected near the base of the reservoir, a chamber is formed within the reservoir. Steam flows to the edges of the chamber and condenses, releasing heat energy into the reservoir and mobilizing the bitumen. The liquids drain by gravity into the lower well, creating space for more steam to flow in.

Bitumen Production from Suncor's Firebag reservoir, the subject reservoir studied in this thesis, is from the McMurray formation, which is almost completely located within the Athabasca oil sands area. The bitumen in the McMurray formation makes up 45% of the total in-place crude bitumen volumes in Alberta. The net pay thickness map of the McMurray Formation is shown in Figure 1.1.3. For reference, the Firebag project is shown in the figure. The MacKay River project is also shown which is immediately adjacent to the underground test facility (UTF). The Alberta Oilsands Technology and Research Authority (AOSTRA) operated UTF pilot in the 1980's to evaluate recovery using horizontal well technology by drilling from underground shafts and tunnels. Research performed at the UTF was key to developing SAGD technology

and testing the feasibility of the SAGD process in the McMurray formation. For most industrial oil sands operators in the McMurray Formation, the minimum oil column thickness, often referred to as the minimum pay, is set equal to 10m. This pay cut off is used to determine those areas for commercial in situ development and the calculation of established bitumen reserves.

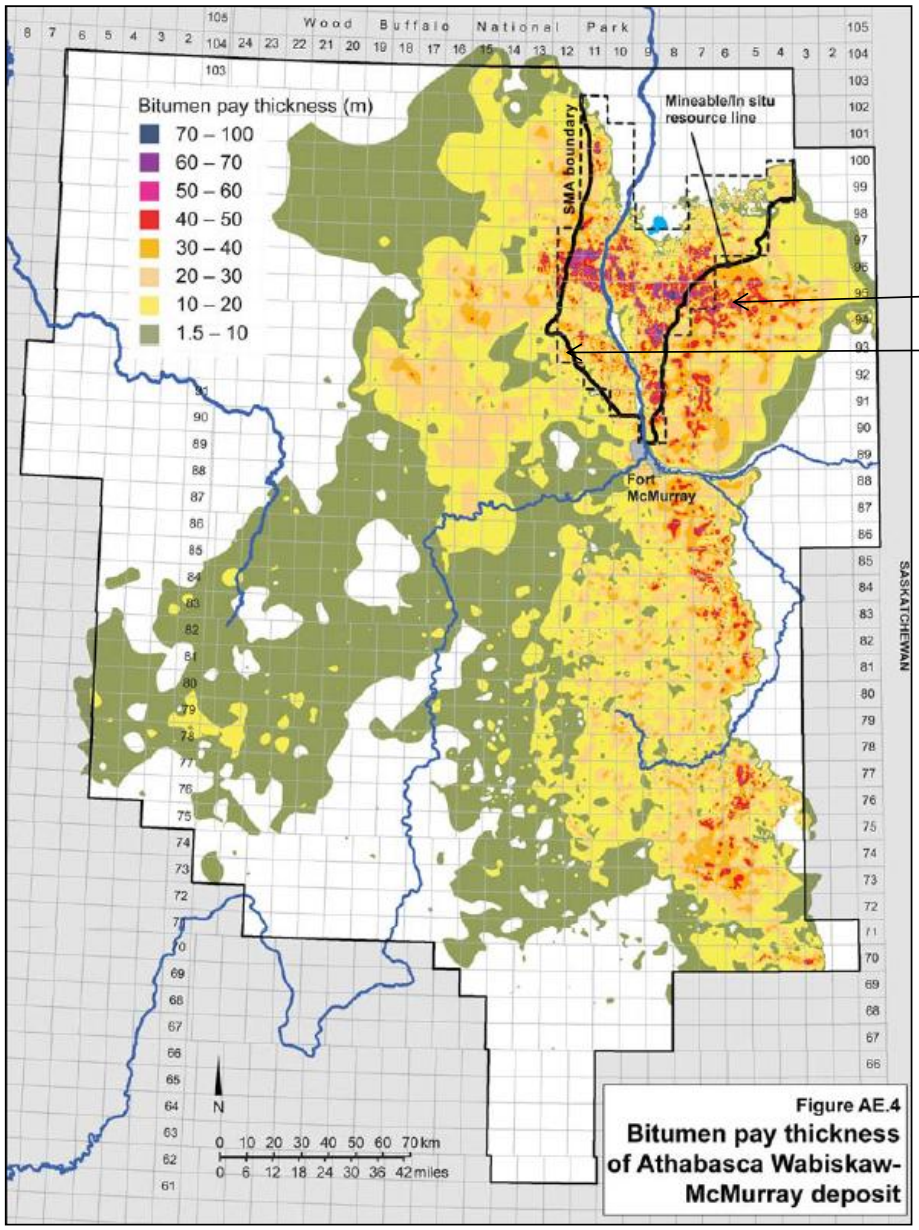

Firebag

MacKay River and UTF

Figure 1.1.3: Net pay thickness map of the McMurray bitumen deposit (courtesy of AER, 2012). Economic limit cutoff for net pay thickness is 10-20m.

In 2011, bitumen accounted for 78 per cent of Alberta's total crude oil and raw bitumen production and is expected to be a larger proportion of the total going forward. It is expected that as time progresses, in situ production will continue to be a larger component of bitumen production since approximately 80% of the established bitumen reserves are outside the relatively shallow (less than about 70 m) mineable areas and due to their depth, they must be extracted by using in situ methods. The Alberta Energy Regulator (AER), formerly the Energy and Resources Conservation Board (ERCB) has created a forecast for bitumen production based on the outstanding applications and projected applications for future oilsands projects, shown in Figure 1.1.4. The projection reveals that the production from in situ bitumen projects is projected to surpass that from mining projects by 2015.

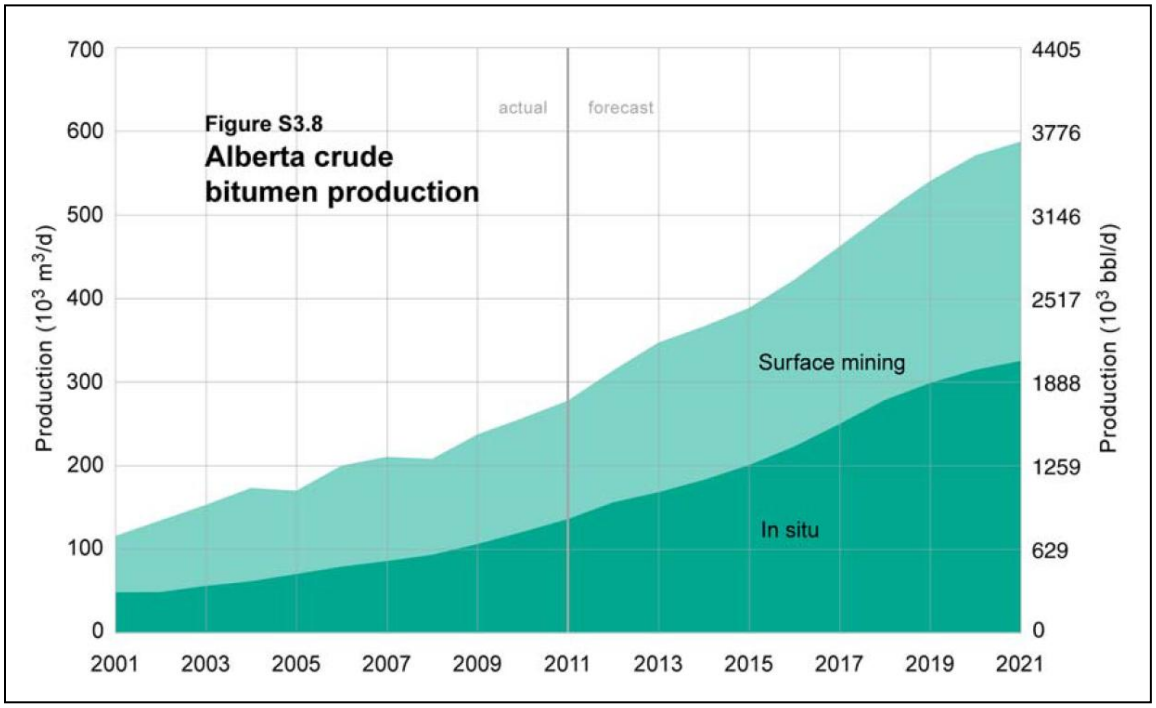

Figure 1.1.4: Surface mining and in situ oil production forecast (courtesy of AER, 2012).

1.2 Suncor Firebag Property

Suncor owns and operates the Firebag property which is located approximately 65 km north of Fort McMurray. Within the AER approved Firebag project area alone, there is over 8 billion barrels of bitumen in place at Firebag (Suncor, 2012). Delineation drilling has shown that there is much more commercially developable bitumen resource outside of this area. At Firebag, there are currently 117 well pairs and 18 infill wells that are producing from nine SAGD well pads in various stages of production. The most recent expansion (Stage 4) of Firebag was commissioned in late 2012 bringing the current capacity to 180,000 barrels of bitumen per day.

SAGD Well Pads 101, 102, 103, and 104, with locations displayed in Figure 1.2.1, have a significant amount of production history having started up in 2003, 2003, 2005, and 2009

respectively. Pads 105, 107, 108, 106, and 116 are relatively new pads, with the former three pads starting up in 2011 and the latter two pads starting up in 2012. With the exception of Pad 107, the production from these five newer well pads has not yet ramped up to peak production levels.

Numerical simulation has been used extensively in the petroleum industry to predict SAGD performance. With a properly built model and accurate inputs, simulation can be used to understand the physics and forecast the performance of the SAGD process. However thermal reservoir simulation on a field level is very time intensive due to the amount of time and resources required to create the geological model, to convert the geological model to a reservoir simulation model, the computational time required to run the simulation, and the time required to analyze the results of the model. Su et al. (2013) reports on pad scale reservoir simulation models consisting of between 7 and 9 SAGD well pairs taking over four weeks to simulate 6 years of performance in point bar systems with a detailed characterization of the various geological facies and features. These models consist of about 10 million grid blocks but the results demonstrate that models of this order of resolution are required to enable accurate prediction of the SAGD process and well pair interactions. Thus, to simulate field scale operations consisting of many SAGD pads are not currently practical.

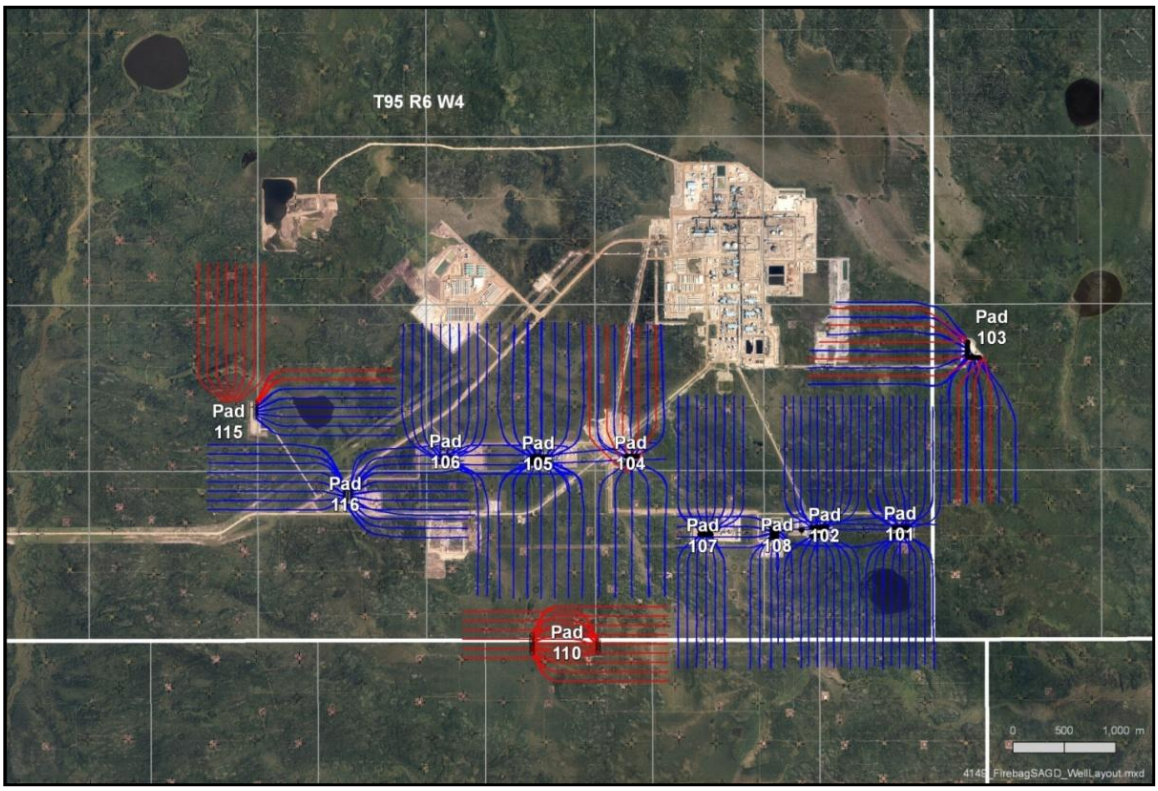

Figure 1.2.1: Layout of Firebag well pads (courtesy of Suncor, 2012).

Analytical methods, such as Butler's simple model (Butler, 1997) are not as comprehensive as simulation in terms of input data and analysis potential, but they can be used to quickly generate performance predictions and related sensitivities. This can serve to aid and expedite decisions where it is not practical to employ full reservoir simulation. Now that there is a significant amount of SAGD performance related data available (the first commercial projects in Alberta started up in Alberta in the late 1990's), empirical analysis of this data can be used to help improve the reliability of analytical methods especially when the models have adjustable parameters that can be calibrated to improve the capability of the models to predict and forecast SAGD performance.

Here, in the research documented in this thesis, an analytical model is developed to predict SAGD performance related to oil drainage and steam injection. The model is developed by using SAGD performance data from the Firebag project. However, the methodology developed here can be applied to similar projects. Validation of this analytical model is performed by comparing the results against historical production and injection volumes for the wells with significant production history at Firebag.

CHAPTER 2: LITERATURE REVIEW

2.1 Analytical Models for Steam Assisted Gravity Drainage

Butler et al. (1981) reported on an analytical model, often referred to as Butler's model, and a scaled model experiment for the steam-assisted gravity drainage (SAGD) process. Their work considered the sideways growth of a chamber in a reservoir that is limited in height but unbounded laterally. Since the focus of their study is on lateral steam chamber growth, it was assumed that the steam chamber height was equivalent to the full reservoir thickness from the onset of SAGD. This is known not to be the case and as a consequence, Butler's model does not provide a completely accurate depiction of the recovery process.

Butler's model describes the oil flow rate of the SAGD process based on Darcy's fluid flow equation with the assumptions that the velocity of the steam chamber interface is constant and that heat transfer is by conduction at steady state conditions. The one dimensional Fourier heat conduction equation was transformed such that the distance variable was measured from the front rather than a fixed origin, as shown in Figure 2.1.1. A solution that satisfied the boundary conditions was developed that assumed the form of an exponential function described by:

$$T^* = \frac{T-T_R}{T_S-T_R} = e^{-\frac{U\varepsilon}{\alpha}} \qquad (2.1.1)$$

Where T_R is the original reservoir temperature, T_S is the steam temperature, U is the speed of the translating steam chamber, α is the thermal diffusivity of the oil sands, and ε is a coordinate referenced to the edge of the steam chamber. The flow rate within an incremental element $d\varepsilon$ shown in Figure 2.1.1 is given by:

$$q = kg\sin(\theta)\int_0^{\infty}\frac{d\varepsilon}{\nu} \qquad (2.1.2)$$

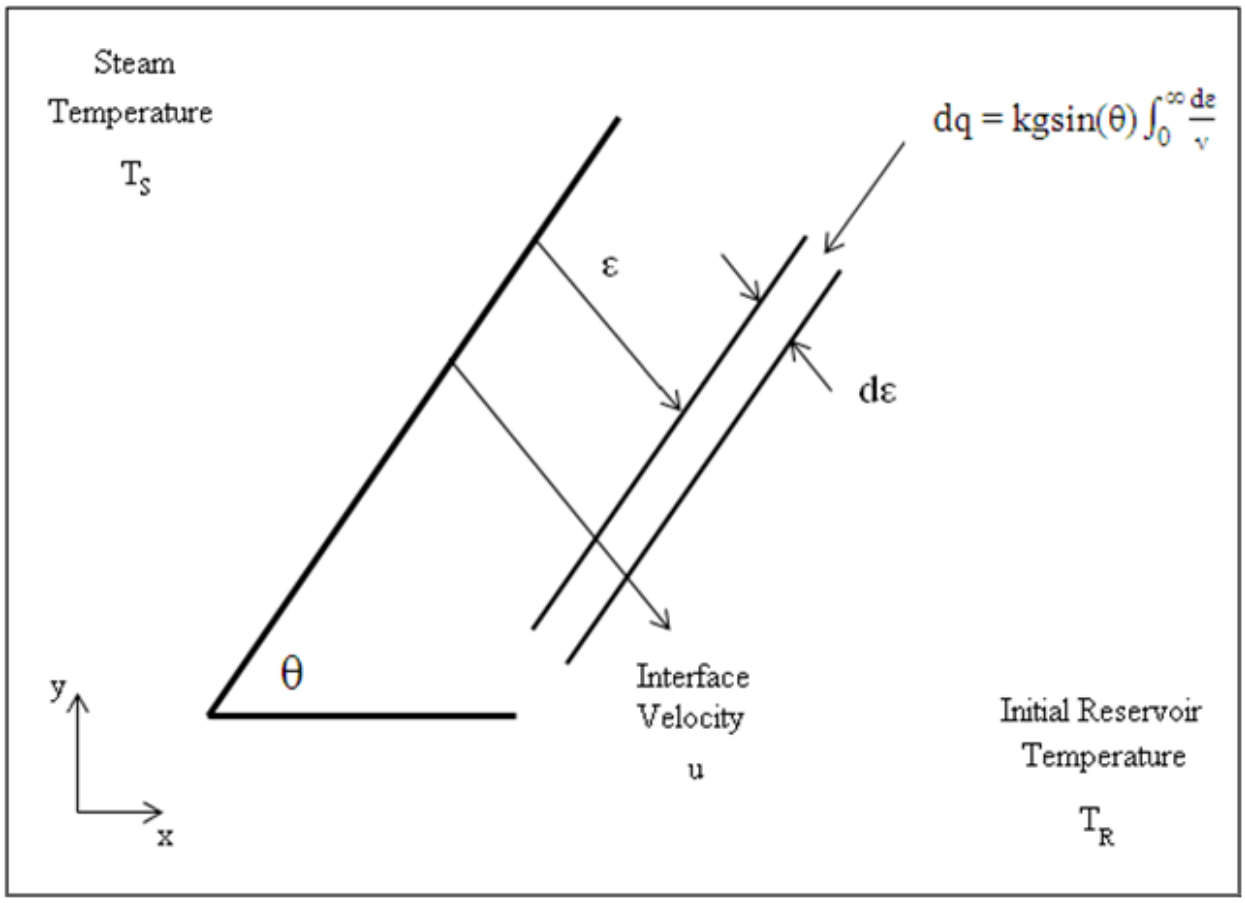

Figure 2.1.1: Cross section of reservoir element at the steam zone interface.

Butler showed that the kinematic viscosity ($\nu=\mu/\rho$, where μ is the dynamic viscosity and ρ is the density) of the bitumen could be well represented by a correlation of the form:

$$\frac{\nu_s}{\nu} = \left(\frac{T-T_R}{T_{S-T_R}}\right)^m \qquad (2.1.3)$$

where *m* is a parameter that describes the change of the viscosity of oil with temperature. Substituting equation (2.1.1) into equation (2.1.3) and then expressing the kinematic viscosity in terms of ε results in an expression for $1/\nu$. This is then substituted into equation 2.1.2 to result in:

$$q = \frac{kg\alpha\sin\theta}{m\nu_s u} \qquad (2.1.4)$$

Consideration of material balance and geometry of the steam chamber allows the unknown variables, that is, steam chamber interface velocity, *u*, and angle of the steam chamber interface, θ, to be replaced with known variables. For the material balance consideration, the drainage rate is directly related to the change in volume of the steam chamber. For a unit length, the drainage rate is directly related to the change in area of the steam chamber. Based on steam chamber geometry, the change in drainage rate *dq* is given by:

$$dq = \varphi S_o \frac{dx}{dt}\, dy \qquad (2.1.5)$$

It should be noted that the advance of the steam chamber is only in the x (cross-well pair) direction, i.e. the height of the steam chamber is not changing with time. In addition, the velocity of the steam chamber in the x direction is:

$$\frac{dx}{dt} = \frac{u}{\sin(\theta)} \qquad (2.1.6)$$

The substitution of equations 2.1.5 and 2.1.6 into equation 2.1.4 yields:

$$\sqrt{\frac{2\varphi S_o kg\alpha(h-y)}{m\nu_s}} \qquad (2.1.7)$$

which describes the drainage rate of oil for one side of the steam chamber. Later work by Butler revised the coefficient of this expression to better represent the SAGD process and this is described later in this paper.

Butler acknowledged that the oil saturation in the steam chamber is neglected in the theory; however the use of a reduced initial oil saturation can be used to compensate. Butler also described that the oil saturation could be estimated using the integrated form of Cardwell et al. (1942):

$$S_{or} = \frac{b-1}{b}\left(\frac{v_s \varphi h_s}{b k_v g t}\right)^{\frac{1}{b-1}} \qquad (2.1.8)$$

with a typical value of 3.5 for the relative permeability exponent, b. Cardwell's equation assumes a homogeneous reservoir, and neglects capillary pressure effects.

Butler conducted scaled laboratory experiments in a model of glass beads (29 cm long by 11 cm high by 2.5 cm thick) that emulated the horizontal well SAGD process at atmospheric pressure. A wire mesh bounded one side of the model and allowed for steam to be injected near the top and produced fluids allowed to drain out the bottom as shown in Figure 2.1.2. The results from the model approximated the theoretical predictions described above quite closely as shown in Figure 2.1.3.

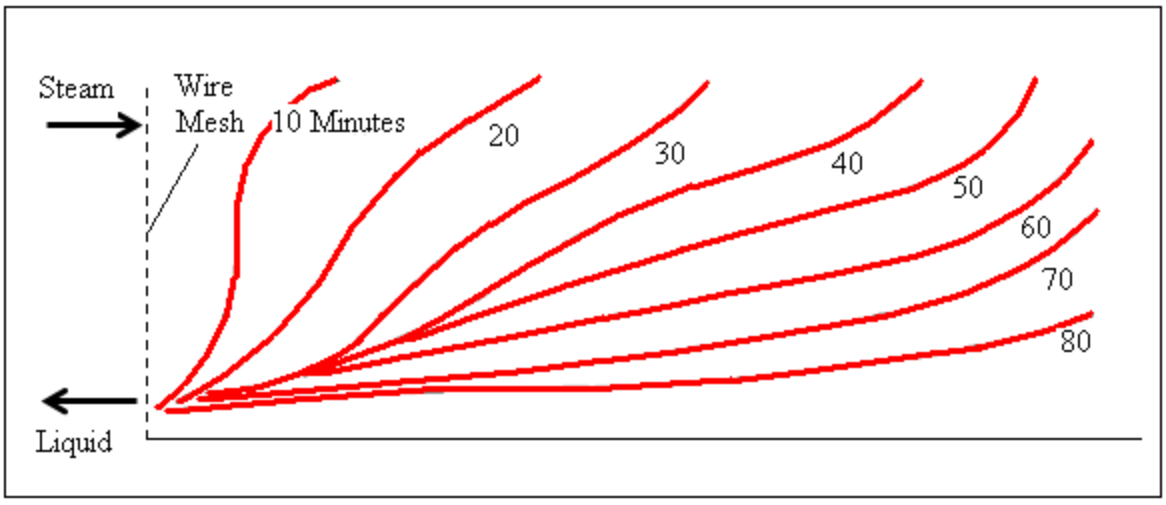

Figure 2.1.2: Diagram of glass sided model showing lateral steam chamber growth with time.

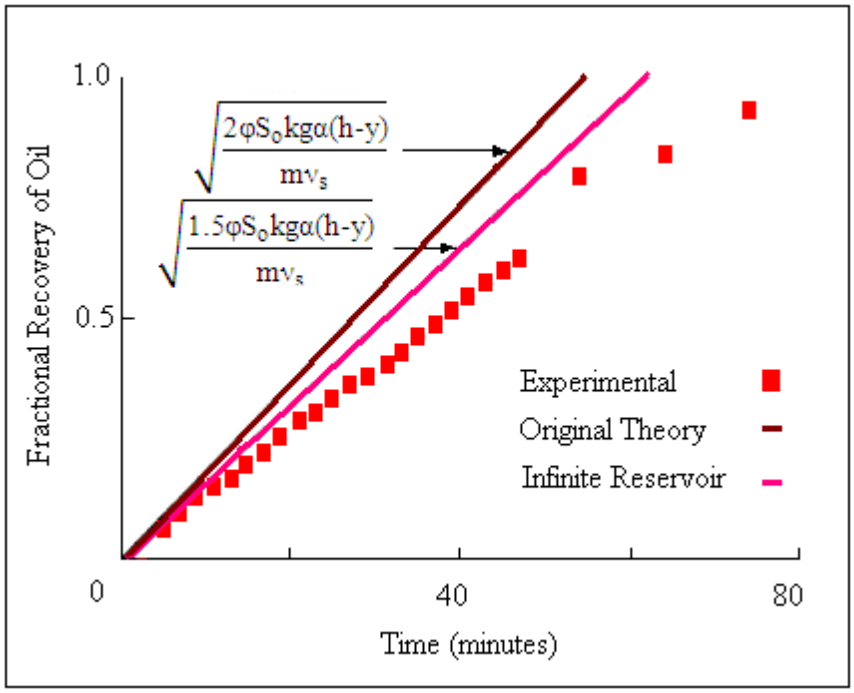

Figure 2.1.3: Theoretical oil rate predictions and experimental oil rates associated with lateral steam chamber growth.

From the drainage theory, Butler derived two similarity groups to scale between laboratory and field values. The first group, the dimensionless time group *t'*, was calculated using a material balance relationship and dimensionless positions for x and y to allow for time scaling (i.e. X = x/h and Y = y/h). This revealed that 10 minutes for the model would be equivalent to 1.6 years in the field. The dimensionless time was given by:

$$t' = \frac{t}{h}\sqrt{\frac{kg\alpha}{\varphi S_o v_s mh}} \qquad (2.1.9)$$

The second dimensional similarity group, B_2, was created to reconcile the case where a high thermal diffusivity could be used to offset a low reservoir permeability. This was done by honouring the dimensionless Fourier number and resulted in:

$$B_2 = \frac{mkgh}{\varphi S_o \alpha \nu_s} \qquad (2.1.10)$$

B_2 relates the factors which control the drainage of oil at and beyond the interface arising from thermal conduction. A large value of B_2 results in gravity drainage of a relatively thin, rapidly draining, layer of oil with only a small amount of heat penetrating beyond the interface. A small value of B_2 represents a thick, slowly moving, column of oil.

Butler et al. conducted an additional experiment at reservoir pressure by using vertical wells. After making the allowance for radial flow (rather than linear flow), it was demonstrated that at expected SAGD operation pressures, the production rates were still of the same order as the prediction from equation 2.1.7. Thus, the results confirmed Butler's gravity drainage model at laboratory scale.

Butler (1984, 1998) also performed work to describe the viscosity coefficient, m, in more detail. In general, oils with lower viscosity have lower values of m which result in higher oil drainage rates. The calculated value of m is shown as a function of temperature for hypothetical oils that are similar to Athabasca, Cold Lake, and Lloydminster in Figure 2.1.4. The equation for *m*, which accounts for reservoir temperature and describes the relationship between temperature and crude oil viscosity, is given by:

$$m = \left[\nu_s \int_{T_R}^{T_s} \left(\frac{\frac{1}{\nu} - \frac{1}{\nu_R}}{T - T_R} \right) dT \right]^{-1} \qquad (2.1.11)$$

Equation 2.1.7 developed in Butler's original analytical model predicts that the entire steam interface moves away from the producer well as shown in Figure 2.1.5. As a result, the oil drainage rate is over predicted in this model since any oil that flows along the edge of the steam

chamber to the bottom of the reservoir is assumed to be produced by the well. In reality, since gravity is the driving force for oil drainage, there is no pressure differential available to transport bitumen horizontally through the reservoir once it reaches the bottom of the steam chamber.

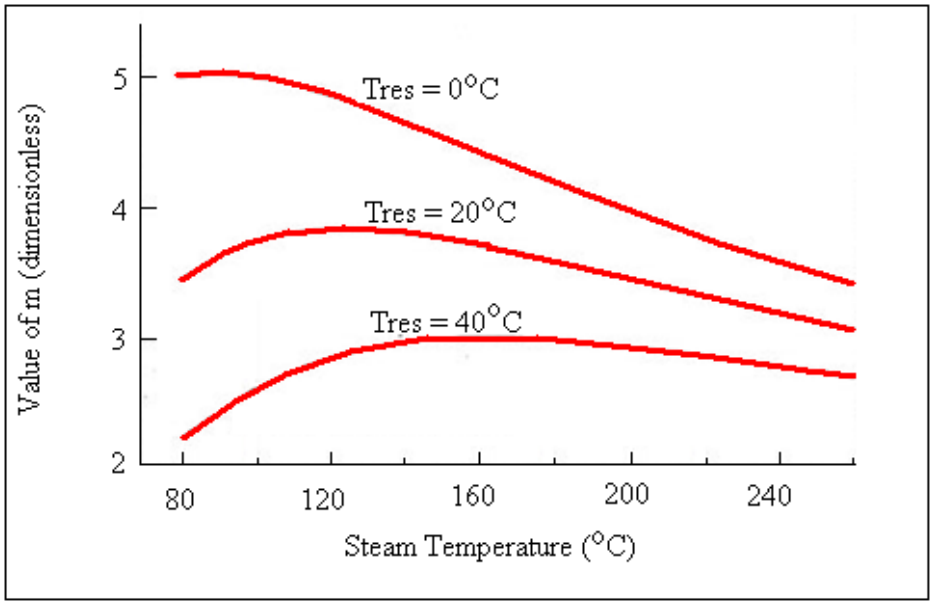

Figure 2.1.4: Viscosity coefficient as a function of temperature for hypothetical heavy oils.

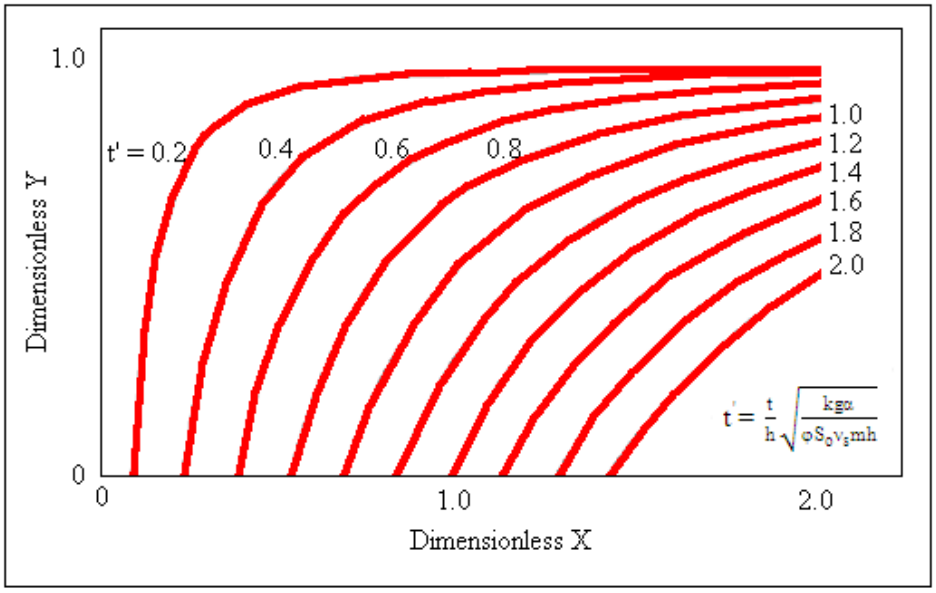

Figure 2.1.5: Steam chamber interface curves shown on dimensionless position scale.

This was recognized and addressed by Butler and Stephens (1981) in an extension to the original model. There were two changes made to the model: the interface curves were now fixed at one end to the producer well and the confining effects of a no-flow boundary halfway between adjacent horizontal wells in a SAGD pattern were now considered.

To adjust the interface curves so that they are fixed at the producer well, the "talus" slope was approximated at a particular time with the use of tangent lines from the producer well to the interface curves from Figure 2.1.6. This approximation is referred to as the TANDRAIN assumption. The net impact of the new TANDRAIN interface curves is a reduction in recovery of approximately 13% when compared to the previous model. This is reflected in the drainage rate equation by changing the constant in Equation 2.1.7 from 2 to 1.5. A graphical representation of this reduction is shown in Figure 2.1.7 at a dimensionless time of T=0.5.

It should also be noted that LINDRAIN, a variation of the derivation of the TANDRAIN equation, assumes that the interface is a straight line directly to the top of the reservoir. The interface becomes longer with a shallower slope as the steam chamber grows. The drainage rate equation that is obtained is similar to that of the TANDRAIN model (Equation 2.1.7) with the exception that the constant of 1.5 is replaced with a constant equal to 1.3

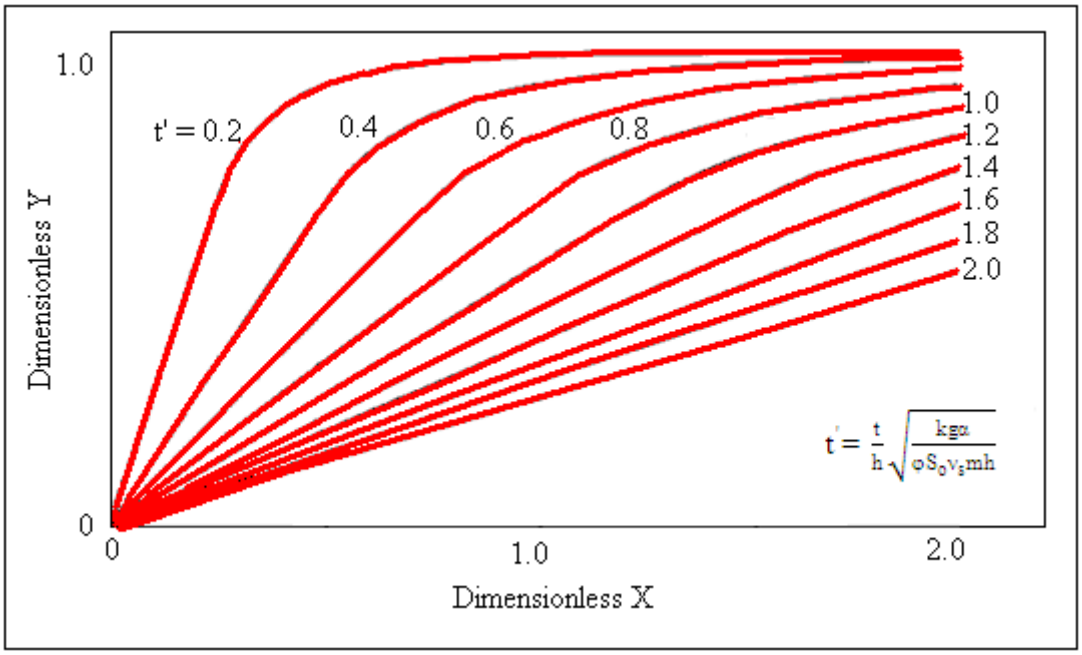

Figure 2.1.6: TANDRAIN steam chamber interface curves shown on dimensionless position scale.

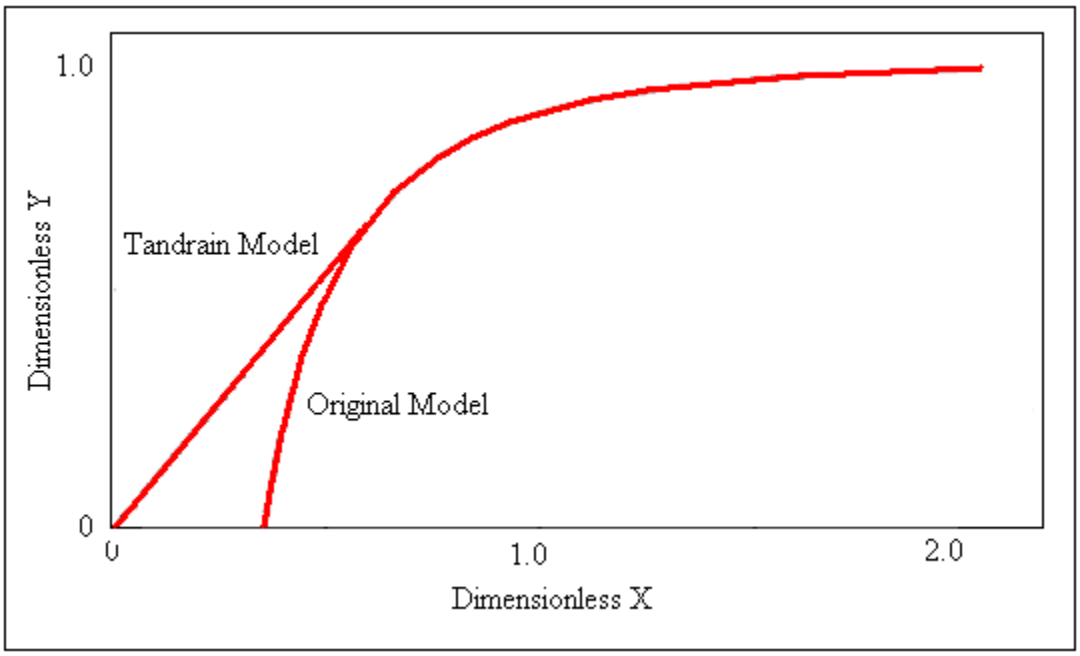

Figure 2.1.7: Impact of TANDRAIN assumption on recovery at a dimensionless time of 0.5.

To account for the effects of the no-flow boundary, Butler employed a numerical approach to calculate the vertical position of the steam chamber interface with time. At the start, the steam chamber interface at the no-flow boundary was at the full reservoir height, however as the reservoir is depleted, the reservoir height that provides the driving force decreased with time. The curves calculated by this numerical approach are shown in Figure 2.1.8.

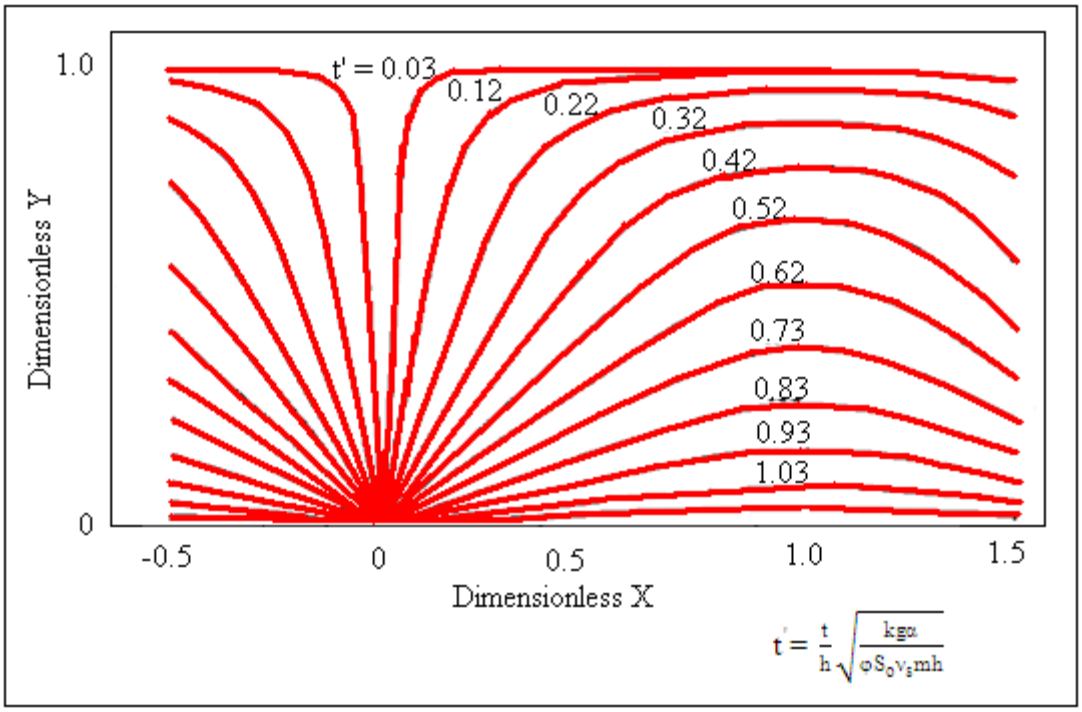

Figure 2.1.8: Steam chamber interface curves from the TANDRAIN model for various dimensionless times.

A simple approximation to the numerical approach is given by (Butler, 1981):

$$q = \frac{\sqrt{3}}{2} - \frac{\sqrt{2}}{3} t^{*2} \qquad (2.1.12)$$

Equation 2.1.12 satisfies the condition that $\int q^* dt^* = 1$ to ensure that the total amount of oil produced from the reservoir does not exceed the oil initially in place. It also results in a very

good fit when compared to the numerical solution as shown in Figure 2.1.9. Figure 2.1.10 shows the comparison between the original model, the TANDRAIN model, and the experimental data.

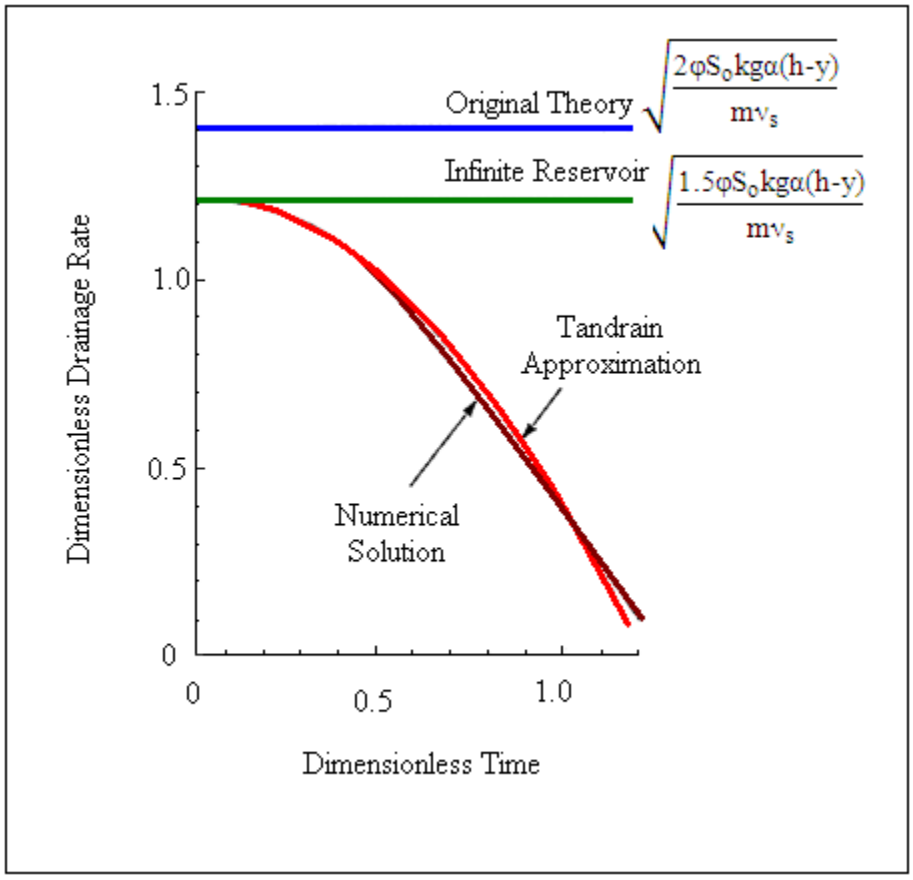

Figure 2.1.9: Comparison of the simplified approximation with the TANDRAIN numerical solution.

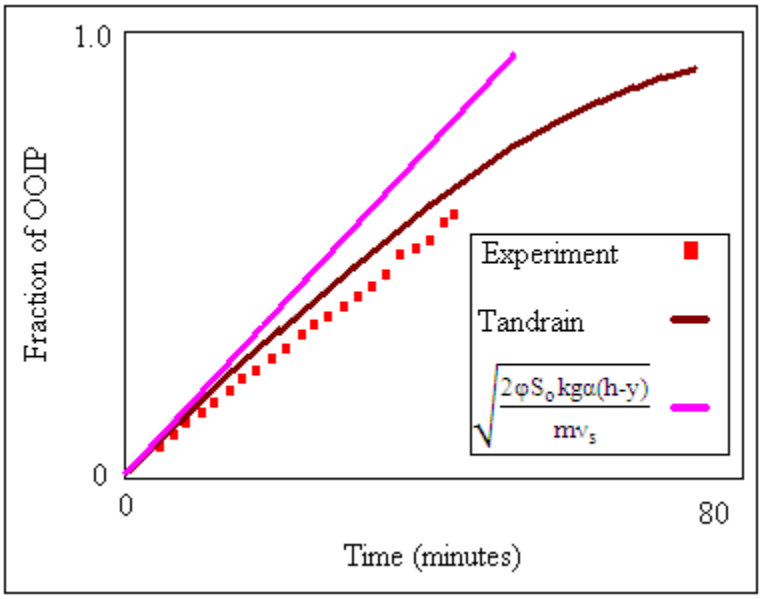

Figure 2.1.10: Comparison of oil recovery with time between original Butler model, TANDRAIN model, and experimental data.

It should be noted that the dimensionless time t* is different than t' for the confined case in Equation 2.1.9. $\boldsymbol{\nu}$ The dimensionless time is multiplied by the well spacing ratio *w/H* so that it does not appear in other equations in the numerical problem. The new dimensionless time is given by:

$$t^* = \frac{t}{w}\sqrt{\frac{kg\alpha}{\varphi S_o v_s mh}} \qquad (2.1.13)$$

To validate the theory, Butler used an improved laboratory apparatus for the experiments. The model was now 36 cm wide by 26 cm high by 2.5 cm thick and packed with a coarse grained sand. The steam inlet and oil outlets are now both positioned inside the model. They are placed near the bottom of the reservoir with the steam inlet 2 cm above the outlet for the produced oil. The experiment was carried out at atmospheric pressure and the grain size of the sand was chosen so that the permeability would preserve the scaling of the model to the field. The

dimensionless groups B_2 and t' derived earlier were both used again to scale from laboratory to field results.

Butler et al. (1981) considered oil drainage rate as a function of steam chamber growth in the vertical direction. It was found that drainage rate increased during this vertical growth phase. For this analysis, the assumption made was that the steam zone was circular in shape so that the growth rate was the same as the increase in radius. An expression as a function of time was developed to predict the growth of the steam chamber in the vertical direction.

A revision to the expression describing drainage rate in the vertical growth phase was provided by Butler (1998). The assumption is that the chamber remains geometrically similar as it rises which is justified through experiments with visual models. A factor, β, was included in Equation 2.1.7 to take into account the flow rate for different chamber heights. Another constant, γ, is also introduced to describe the shape of the chamber. The area of the chamber is γh^2, so in effect, γ is simply a shape factor relating the width of the chamber to the height. The expression that then describes the height of the chamber as a function of time is then:

$$h = \left(\frac{9}{4}\frac{\beta}{\gamma^2}\right)^{\frac{1}{3}} \left(\frac{kg\alpha}{mv_s\varphi\Delta S_o}\right)^{\frac{1}{3}} t^{\frac{2}{3}} \qquad (2.1.14)$$

A scaled model experiment was performed in which the chamber height was determined by a series of thermocouples above the production well. Based on the thermocouple data, the height of the steam chamber as a function of time was found to follow:

$$h = 2\left(\frac{kg\alpha}{mv_s\varphi\Delta S_o}\right)^{\frac{1}{3}} t^{\frac{4}{3}} \qquad (2.1.15)$$

The comparison between the theoretical and experimental data for chamber height is shown in Figure 2.1.11.

The theoretical chamber height given by Equation 2.1.15 is then substituted into the expression for the cumulative oil produced given by Equation 2.1.16 which yields:

$$Q = \int_0^t q\,dt = \gamma\varphi\Delta S_o h^2 \qquad (2.1.16)$$

and

$$q_{cum} = 4\gamma \left(\frac{kg\alpha}{m\nu_s}\right)^{\frac{1}{3}} (\varphi\Delta S_o)^{\frac{1}{3}} t^{\frac{4}{3}} \qquad (2.1.17)$$

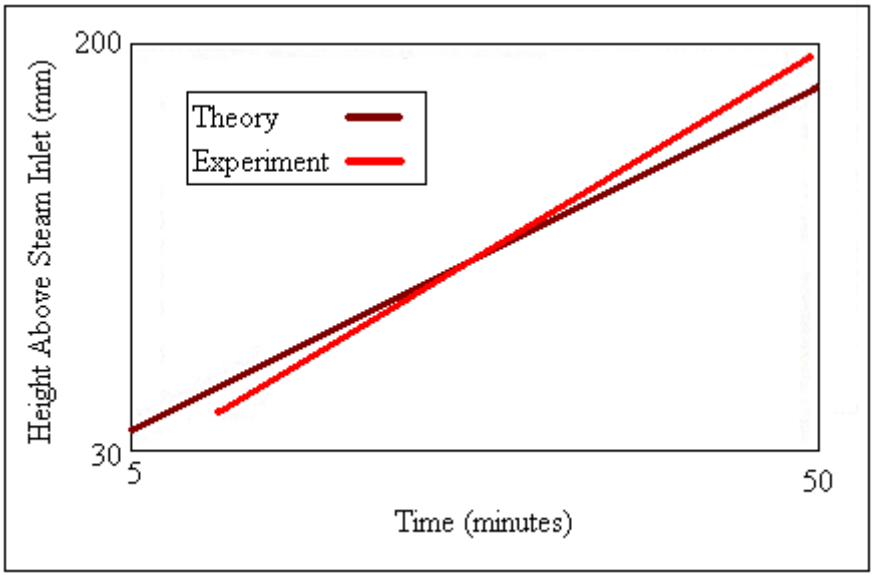

Figure 2.1.11: Comparison between theoretical and experimental data for chamber height as a function of time.

From Equation 2.1.17, to match the experimental cumulative production as shown in Figure 2.1.12, the value of γ is determined to be equal to 9/16.

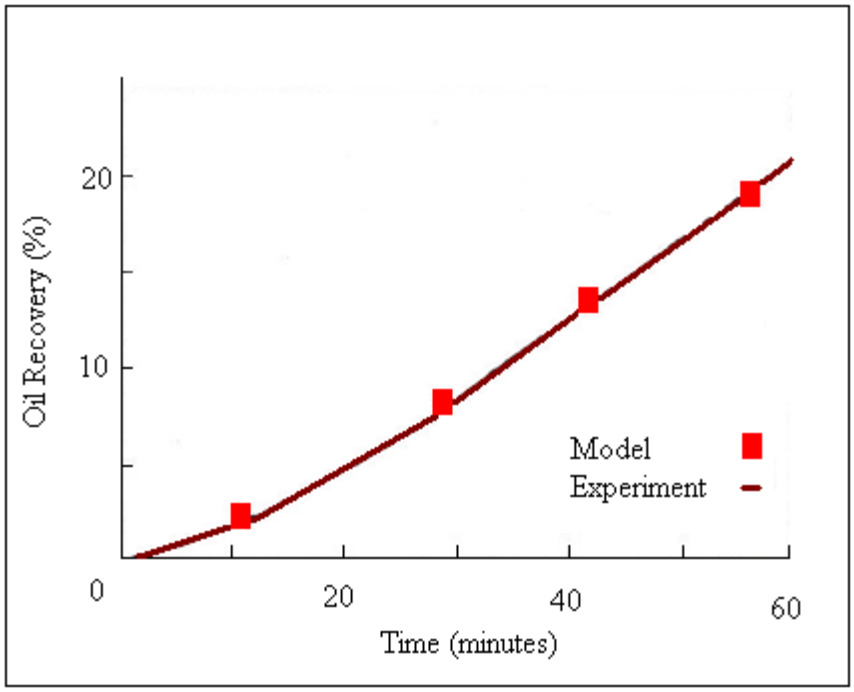

Figure 2.1.12: Comparison of cumulative production between the model and experiment.

The instantaneous production rate is then derived by differentiating Equation 2.1.17 with respect to time:

$$q=3\left(\frac{kg\alpha}{mv_s}\right)^{\frac{2}{3}}(\varphi\Delta S_o)^{\frac{1}{3}}t^{\frac{1}{3}} \qquad (2.1.18)$$

The value of β can then be determined by approximating the chamber shape to be a sector of a circle as shown in Figure 2.1.13. Based on this geometry and with a value for γ = 9/16 or 0.5625, the angle subtended by the sides of the sector is equal to 64°. This results in a value of β equal to 9/8 or 1.125.

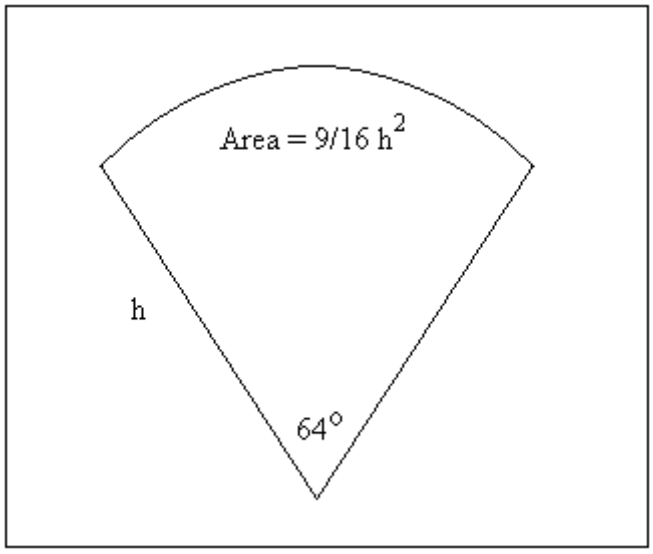

Figure 2.1.13: Sector of circle representing steam chamber.

It was recognized by Butler that Equation 2.1.15 can still be used to determine the oil drainage rate during the rising chamber phase until the point at which the drainage rate is equivalent to the drainage rate for the lateral spreading phase.

Reis (1992) developed an analytical model that could be used to predict oil rate and steam-to-oil ratio (SOR) performance for the SAGD process. Reis used the solution for the temperature distribution for conduction at a fixed velocity into a solid with a fixed surface temperature as given by:

$$T^* = \frac{T-T_R}{T_R-T_S} = \frac{1}{2}\left(\text{erfc}\left(\frac{\varepsilon-ut}{2\sqrt{\alpha t}}\right) + e^{\frac{u\varepsilon}{\alpha}}\left[\text{erfc}\left(\frac{\varepsilon+ut}{2\sqrt{\alpha t}}\right)\right]\right) \qquad (2.1.19)$$

This surface is exposed to a stepwise increase in temperature from $T^*=0$ to $T^*=1$ at time $t=0$.

To adapt Equation 2.1.19 for steady state conditions, it is first noted that for the SAGD process, the thickness over which the temperature varies (ξ) is small and therefore negligible compared to the term *ut* which represents the steam chamber width. For large values of *t*, a simplification of Equation 2.1.19 can be performed since erfc(∞) = 0. Equation 2.1.19 then becomes the same equation used by Butler derived from the one dimensional Fourier heat conduction equation:

$$\frac{T-T_R}{T_S-T_R} = e^{\frac{-u\varepsilon}{\alpha}} \qquad (2.1.20)$$

The expression for the oil rate used by Reis is derived from the same temperature distribution that Butler used and employed the assumptions with regard to Darcy's law for fluid flow, and material balance based on steam chamber geometry. A modification was made by Reis to the term for the velocity of the steam chamber front. Instead of using the average velocity, *u*, the maximum velocity, u_m, was used in conjunction with a dimensionless temperature coefficient, *a*. As a result, the expression for the oil rate was similar to that proposed by Butler. By using a value of *a* equal to 0.4, Reis could match Butler's experimental work giving:

$$q_o = \sqrt{\frac{\varphi \Delta S_o k_o g h \alpha}{2 a v_{os} m}} \qquad (2.1.21)$$

As can be seen, the only difference between the derivation by Reis (1992) and Butler (1981) is the value of the constant within the square root. With *a*=0.4, the constant within the square root has a value equal to 1.2. The value of the constant derived by Butler's original work was 2, and this value was subsequently revised by Butler to 1.5 using the TANDRAIN assumption and then to 1.3 using the LINDRAIN assumption. Butler acknowledged the TANDRAIN model resulted in a drainage rate that was high and that the LINDRAIN assumption would be more realistic.

The assumption made by Reis (1992) was based on the steam zone geometry; he assumed that heat losses to the underburden are negligible and that to maintain the steam zone at a constant temperature the required enthalpy is supplied as latent heat. The total heat requirements to maintain the steam zone was broken down into three components: the enthalpy required to expand the steam zone, the enthalpy to preheat the reservoir ahead of the steam zone, and the enthalpy lost to the overburden.

The enthalpy required to expand the steam zone was based on the volume of the steam chamber multiplied by the volumetric heat capacity of the reservoir and the increase in temperature between steam temperature and initial reservoir conditions. The corresponding enthalpy injection rate is given by:

$$q_{sz} = \frac{1}{2} M_R \Delta T h \frac{dw_s}{dt} \qquad (2.1.22)$$

The injected enthalpy rate to maintain the steam zone is then given by:

$$q_{sz} = M_R \Delta T \sqrt{\frac{k_o g h \alpha}{2\varphi \Delta S_o a v_{os} m}} \qquad (2.1.23)$$

The enthalpy required to preheat the reservoir ahead of the steam zone was based on an energy balance on the oil zone:

$$d^2 q_R = M_R (T - T_i) d\varepsilon d\eta \qquad (2.1.24)$$

Substituting the expression for the temperature distribution (Equation 2.1.20) into Equation 2.1.24 gives:

$$d^2 q_R = M_R \Delta T e^{\frac{-a u_m \varepsilon}{\alpha}} d\varepsilon d\eta \qquad (2.1.25)$$

which can be integrating from $\xi=0$ to $\xi=\infty$ to give:

$$dq_R = \frac{M_R \Delta T \alpha}{a u_m} d\eta \quad (2.1.26)$$

The maximum velocity of the steam zone interface is found based on geometry and material balance:

$$u_m = \sin(\theta) \frac{dw_s}{dt} = \sqrt{\frac{2k_o g \alpha}{\varphi \Delta S_o a v_{os} m h}} \quad (2.1.27)$$

The vertical length of the interface can be expressed in terms of its height:

$$d\eta = \frac{dy}{\sin(\theta)} \quad (2.1.28)$$

Substituting the values of steam zone interface velocity and vertical interface length into the Equation 2.1.26 and integrating from y=0 to y=h gives a general expression for the total cumulative enthalpy required to establish the temperature distribution in the reservoir at any time:

$$Q_R = \frac{M_R \Delta T h}{\sin^2(\theta)} \sqrt{\frac{\varphi \Delta S_o v_{os} m h \alpha}{2 a k_o g}} \quad (2.1.29)$$

Differentiating the cumulative enthalpy results in an enthalpy injection rate as follows:

$$\frac{dq_r}{dt} = -2 M_R \Delta T h \sqrt{\frac{\varphi \Delta S_o v_{os} m h \alpha}{2 a k_o g}} \sin^{-3}(\theta) \cos(\theta) \frac{d\theta}{dt} \quad (2.1.30)$$

The steam chamber angle is found based on geometry and material balance and then differentiated with respect to time to give:

$$\frac{d(\theta)}{dt} = -\sin^2(\theta) \frac{1}{h} \sqrt{\frac{2k_o g \alpha}{\varphi \Delta S_o h a v_{os} m}} \quad (2.1.31)$$

The final expression for enthalpy injection rate related to maintain the temperature distribution ahead of the steam chamber front is then:

$$q_R = \frac{4 M_R \Delta T \alpha t}{h a} \sqrt{\frac{\alpha k_o g}{2 \varphi \Delta S_o h a v_{os} m}} \quad (2.1.32)$$

The one-dimensional Fourier's law for heat conduction is used to find the heat loss rate to the overburden:

$$q'_L = k_t \int_0^w \frac{dT\,(t-\tau)}{dz}\,dw \qquad (2.1.33)$$

The temperature profile in the overburden is given by the solution to one-dimensional heat loss into a solid:

$$T - T_i = \Delta T\ \mathrm{erfc}\left(\frac{z}{2\sqrt{\alpha(t-\tau)}}\right) \qquad (2.1.34)$$

The heat loss rate to the overburden is then given by:

$$q'_L = 2\alpha M_R \Delta T \sqrt{\frac{2k_o g t}{\pi\varphi\Delta S_o a \nu_{os} m}} \qquad (2.1.35)$$

When equation 2.1.35 is integrated with respect to time, the expression for cumulative heat loss to the overburden is dictated by:

$$Q_L = \frac{4}{3}\alpha M_R \Delta T \sqrt{\frac{2k_o g}{\pi\varphi\Delta S_o a \nu_{os} m}}\, t^{\frac{3}{2}} \qquad (2.1.36)$$

Since the total heat requirements associated with the expansion of the steam zone, the heat stored in the reservoir ahead of the steam zone, and the enthalpy lost to the overburden were quantified, and the latent heat energy of the steam is known, the steam injection rate required to supply these sources of heat consumption can be determined.

Edmunds and Petersen (2007) developed an analytical model that could be used to predict the cumulative steam-to-oil ratio (cSOR) of SAGD or other steam-based bitumen recovery processes. The nature of the work was similar to the work performed by Reis (1992). A simplification was made to the model by using an empirical constant which accounts for heat

stored below the steam chamber as a factor of the overburden heat loss. The theory was also extended to cyclic steam operations by using an effective temperature for the steam zone.

The model assumed that the geometry of the SAGD steam chamber was similar to a trough with straight edges as shown in Figure 2.1.14. It was noted by the authors that this may not be realistic in a heterogeneous reservoir, however it was also noted that thermal effects tend to straighten the slope of the steam chamber.

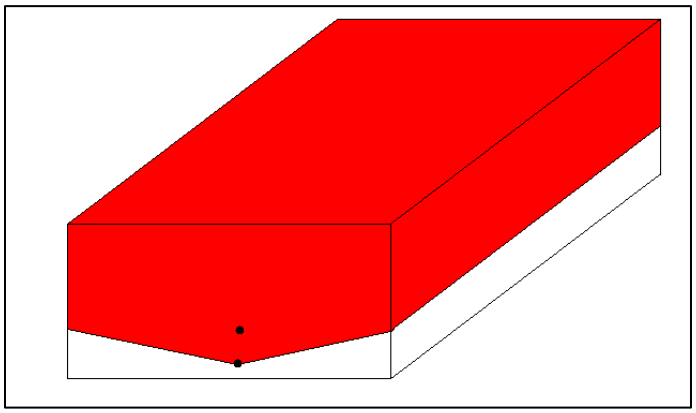

Figure 2.1.14: Trough shaped steam chamber geometry.

The total heat consumption was broken into three components as shown in Figure 2.1.15: overburden heat losses (H_o), heat inside the steam chamber (H_c), and heat stored below the steam chamber and ahead of the steam chamber interface (H_L).

Overburden heat loss was based on Equation 2.1.37, derived by Carslaw et al. (1959) which defined cumulative heat loss to a semi-infinite plane exposed to a step rise in temperature:

$$H_\infty = 2A\Delta T k_t \sqrt{\frac{t}{\pi\alpha}} = 2A\Delta T \sqrt{\frac{k_t C_{vo} t}{\pi}} \qquad (2.1.37)$$

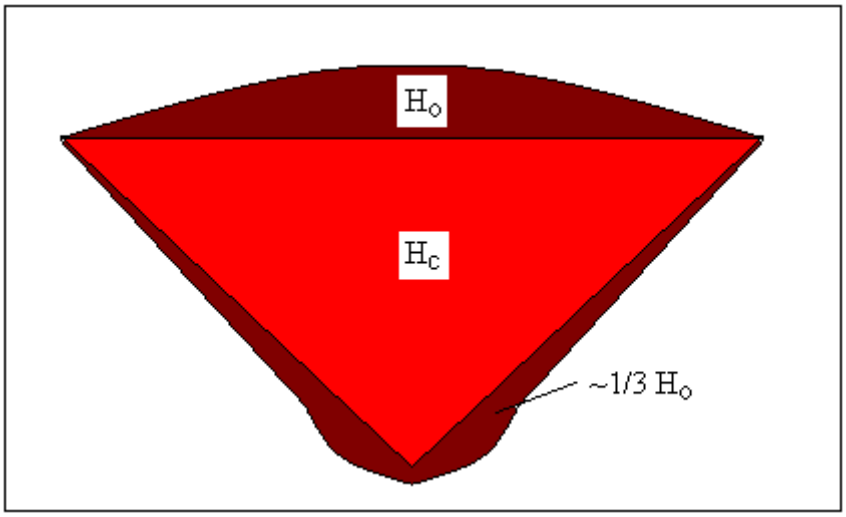

Figure 2.1.15: Heat consumption schematic for SAGD steam chamber.

However, the heated area is not constant and grows with time so a dimensionless parameter, *a*, is introduced which varies from 0 to 1 and represents fractions of the total heated area. A variable, $\lambda(a)$, is also defined as the time at which the area represented by *a* is exposed. The modified expression is then given by:

$$H_o = 2A\Delta T \sqrt{\frac{k_t C_{vo}}{\pi}} \int_0^1 \sqrt{t - \lambda(a)}\, da \qquad (2.1.38)$$

With the assumption that areal expansion is constant with time, $\lambda(a)=at$, then the overburden heat loss is:

$$H_o = \frac{4}{3} A\Delta T \sqrt{\frac{k_t C_{vo} t}{\pi}} \qquad (2.1.39)$$

Since the steam chamber volume and volumetric heat capacity are known, the heat energy required to heat the reservoir from initial temperature to steam temperature can be calculated:

$$H_c = A\Delta TC_{vr}h\eta_s \quad (2.1.40)$$

The total heat losses that are not related to the overburden and steam chamber are accounted for in the H_L term which is empirically shown to be equal to roughly one third of the overburden heat losses.

When all of the sources of heat consumption are added together, total steam requirements can be calculated. The assumption made in Edmunds et al.'s analysis is that the latent heat of the steam provides these heat requirements and that all the sensible heat is withdrawn from the steam chamber with the produced fluids.

The cumulative oil production is based on the decrease in oil saturation (from initial to residual) within the steam chamber. The final expression used to calculate the cSOR is given by:

$$CSOR = \left(\frac{\Delta T}{H_{lv}\varphi\Delta S_o}\right)\left(C_{vr} + \frac{\sqrt{k_t C_{vo} t}}{h\eta_s}\right) \quad (2.1.41)$$

Edmunds and Petersen conducted a two-dimensional numerical simulation study was conducted and compared to this analytical model with satisfactory results. In addition this model was used to forecast the cSOR profiles of the Foster Creek SAGD, Primrose SAGD, and Cold Lake CSS projects and was able to match historical data with reasonable accuracy. The effective temperature assumption for the CSS project assumed that the effective temperature corresponded to the temperature at the end of each CSS cycle which effectively models the process as a continuous low pressure operation.

Miura et al. (2010) extended the work of Edmunds et al. The revised model was used to forecast CSOR for the Hangingstone project and there was good agreement with historical field

performance. The first modification was the inclusion of a time dependent oil saturation after the work of Cardwell et al. (1942). The second modification was the incorporation of a rising steam chamber phase which employed the equation Butler derived (Equation 2.1.15). The third modification was a shape factor, β, which was used to relate the field production data with the effective sweep efficiency.

$$\eta_s = \frac{V_{sz}}{Ah} = \frac{\beta A h_s}{Ah} = \frac{h_s}{h} \qquad (2.1.42)$$

It was noted by the authors that the physical meaning of this assumption could be a curved steam chamber shape as shown in Figure 2.1.16. The shape factor did not change with time and it was assumed that the steam chamber would maintain the same shape from early SAGD until the steam chamber reached the top of the reservoir.

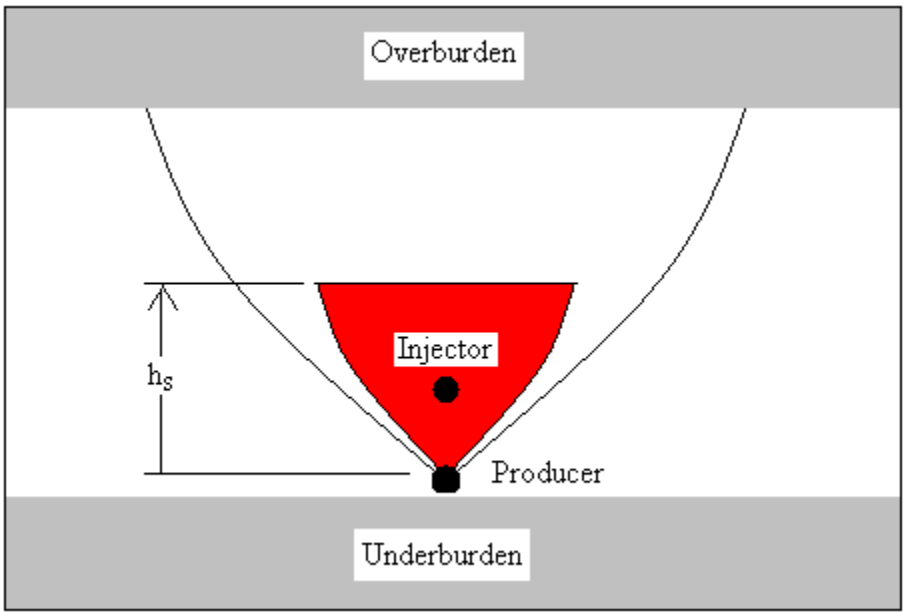

Figure 2.1.16: Schematic of shape factor in relation to steam chamber rising phase.

The fourth modification was the incorporation of subcool operation. In Edmunds and Peterson's original work, it was assumed that only latent heat would supply the heat consumption by the reservoir. However in practice, many SAGD operators operate based on a temperature differential (called Subcool) where the temperature of the produced fluids is lower than the steam injection temperature and this difference is controlled within a specified range. The impact of subcool operation from an enthalpy perspective is that there will be some energy left in the reservoir from sensible heat in addition to the latent heat. The modification is implemented by simply replacing the latent heat term used in the original model with the difference in temperature between the injected steam and produced fluids.

The last modification was related to overstated overburden losses. It was stated by the authors that overburden heat losses would be lower after coalescence of the steam chambers from adjacent well pairs. A correction for excess heat consumption by the overburden was then applied based on steam chamber geometry.

Edmunds et al. (2001) proposed a semi-empirical cSOR function given by:

$$CSOR = \frac{\Delta T}{H_{lv}}\left[A + B\sqrt{t}\right] \qquad (2.1.43)$$

In Equation 2.1.43, *A* is a constant that accounts for heat stored in the steam chamber (it is a function of porosity and movable oil saturation) and *B* is a constant that accounts for conduction losses outside the steam chamber. If steam pressure is reduced, the term $\Delta T/H_{lv}$ is also reduced, however pattern life *t* increases due to slower drainage. The net effect is that regardless of the relative values of factors *A* and *B*, the cSOR is expected to decrease with decreasing steam pressure.

Ito et al. (1998) investigated the recovery mechanisms in SAGD by using numerical simulation. The contribution from each individual parameter from Butler's analytical model (Equation 2.1.7) was analyzed individually and a modified equation was obtained. In Equation 2.1.7, the flow rate was proportional to the square root of each variable. The modified expression by Ito et al. is shown in Equation 2.1.44 where *c* is an empirically obtained constant and μ_{os60} is the oil viscosity at a temperature 60°C lower than steam temperature:

$$q_o = \frac{c h k_h^{0.75} \left(\frac{k_v}{k_h}\right)^{0.40} \Delta S_o \varphi^{0.45}}{\mu_{os60}^{0.33}} \qquad (2.1.44)$$

It was observed that convection heating dominated a narrow region near the steam zone interface where fluid movement is significant. The volume of steam condensate flowing down the edges of the steam chamber is two to five times that of oil and works to transfer heat via convection beyond the chamber edge. Ahead of the steam zone interface, where the reservoir is closer to initial reservoir temperature, there is less fluid mobility and conduction is the dominant mechanism for heat transfer.

Three sources of energy consumption were identified – heat loss to the adjacent strata, heat energy in the produced fluids, and heat accumulated in the reservoir. The steam-to-oil ratio was tied to the accumulated energy in the reservoir. At high steam injection pressures, oil production rates increase due to lower oil viscosity. However, the fraction of energy in the produced fluids is higher, and more energy is required to expand each unit volume of the steam chamber. The net result is that a higher steam-to-oil ratio is associated with higher operating pressure.

It is also noted that in later periods of the well life, condensate from the chamber ceiling can flow ahead of the steam chamber and provide convective heating. In addition, the energy accumulation ahead of the steam chamber is reduced when coalescence of steam chambers occurs, reducing the steam oil ratio.

Sharma and Gates (2011), in an extension of Butler's model, derived an apparent thermal diffusivity in order to describe the effect that convection has at the edge of the steam chamber. The apparent thermal diffusivity was a function of the relative permeability exponents, and the fluid properties (density, specific heat capacity, permeability and viscosity). It was shown that, that convection effects are significant at the edge of the steam chamber as steam condensate carries energy into the oil sand, and that the resultant temperature profile ahead of the steam chamber edge is higher than if conduction was acting alone. The higher temperature reduces the viscosity of the oil, however it also reduces the oil saturation and this results in a decreased mobility due to relative permeability effects. The net result was that there is only a slight increase in oil drainage rate when convection heating is taken into account.

In this study it was shown that the zone in which convection is active is narrower than the zone that conduction acts on and that the convective heat transfer component becomes minor at a distance approximately 3.5m from the edge of the chamber. It is also shown that at higher steam temperatures (and therefore operating pressures), there is a higher convective heat flux component. The work was validated against field data from the Dover Phase B SAGD pilot and shown to be more accurate than the case where heating occurred by conduction alone.

Walter et al. (2008) investigated the applicability of a semi-analytical model based on Butler's SAGD theory as a proxy for a reservoir simulator. This proxy model predicted oil rate, cumulative oil production and steam injection for the SAGD process as a function of time. Reservoir heterogeneity was modeled as a factor that changed with time based on averaging of the input geological grid at the chamber interface position. Calculation of the average relative permeability using a cubic function was also applied.

There were four adjusting parameters that allowed the proxy model to be fitted over a set of simulations run on nine geological realizations. The geological realizations corresponded to nine deciles from the ranking procedures and were believed to cover the range of variability in the geological model. The fitting parameters used allowed changes to be made to the steam injection and to the decline, rising, and spreading phases of production.

Butler (1984) suggested that at the edges of the steam chamber there are steam fingers that penetrate the oil sand ahead of the top of the steam chamber. Butler used a parabolic function to calculate the shape of the rising finger and determined that these fingers could be between 3 and 6 meters in length in Athabasca bitumen reservoirs. The resultant rise rate of the chamber was determined to be strong functions of steam temperature and oil viscosity. Gotawala and Gates (2008) revised the model describing steam fingering at the edge of a steam chamber in a heavy oil reservoir. The revised model includes gas phase properties, additional Maclaurin expansion series terms for the error function approximation, and assumes the maximum rise rate is associated with the middle of the finger.

The model was applied to oils with m values (Butler's viscosity coefficient) of 2 and 4 which would be representative of Lloydminster heavy oil and Athabasca bitumen respectively. It was found that maximum rise rate was much higher than that calculated by Butler and were directly proportional to gas phase mobility and the density difference between the oil and gas phases and inversely proportional to oil saturation and finger steam oil ratio. It was also found that the fingers ranged in length from pore scale to tens of centimeters. When compared to the conductive heating zone of oil sands which is approximated from the thermal diffusivity of oil sands to be 1-3m, it was found that heat transfer by conduction (not heat transfer by steam finger convection) dominates the heat transfer at the edges of the steam chamber.

2.2 Time Lapse 3D Seismic (4D Seismic)

Time lapse three-dimensional (3D) seismic, referred to as 4D seismic, technology has been used for reservoir monitoring of various thermal projects to understand steam chamber extents and conformance by many authors for over the past 15 years. The basic idea behind seismic in this application is the measurement of the attenuation of energy waves that are created using charges at surface. Receivers placed at surface read the low frequency acoustic energy that is refracted from the various layers of earth below. Zhang et al. (1997) applied 4D seismic analysis to the Christina Lake SAGD project and noted that an increase in temperature from 10°C to 240°C causes a decrease in compressional wave velocity by approximately 20%. This weakening of acoustic impedance is caused by both the reduction of bitumen viscosity as well as an increase in the gas saturation (vapour phase of water) as steam is injected. As a result the variation in amplitude of the waves of reflected energy can be mapped and the anomalies interpreted to determine the areal extents of the SAGD steam chamber.

Zhang et al. also compared cross well seismic, which is seismic which has sources and receivers placed inside vertical wells to surface 3D seismic, in which sources and receivers are at surface. Both velocity information (tomography) and the up-going P-wave reflection (reflections from below the source and receiver depths) image to generate the cross well seismic interpretation. The end result is a much higher resolution than that obtained from surface 3D seismic. The resultant cross well seismic interpretation was found to be in agreement with geological data interpreted from the vertical well logs and provided a qualitative indication of unswept zones and steam chamber conformance.

Steam chamber extent has been estimated using 4D seismic in the Hangingstone reservoir by Tanaka et al. (2010). The Hangingstone reservoir is approximately 100km south of the Firebag reservoir, and has comparable reservoir properties. It has been producing oil using SAGD technology since 1999 from the McMurray formation). In this study, a defined boundary of the steam chamber was mapped where temperature is greater than 260°C. P-wave velocity maps were obtained by transforming the seismic travel-time maps and this provided an interpretation of the areal extent of the steam chamber zone. In order to separate pressure effects from temperature effects, these P-wave velocities were applied to a rock physics model developed by Kato et al. (2008), to determine the boundary of the steam chamber area. Assuming reservoir sweep as shown in the diagram in Figure 2.2.1, (with Soi = 0.77, Sor = 0.05) a recovery factor above producer was found to be 84%.

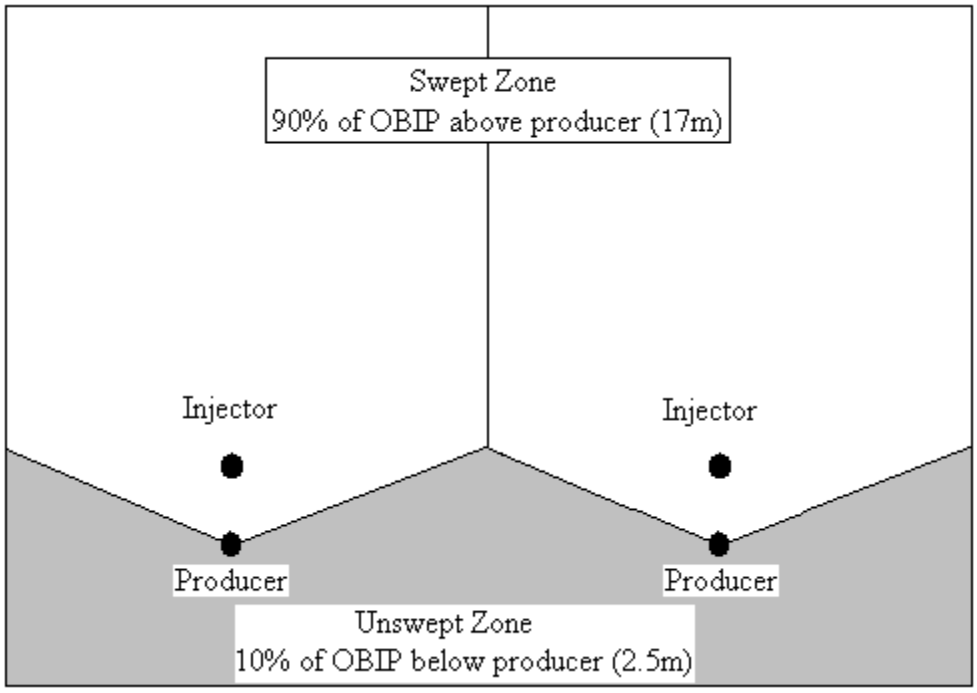

Figure 2.2.1: Steam chamber shape assumption used to measure reservoir sweep.

2.3 Mobile Water

Javad et al. (2010) performed a 2D SAGD laboratory experiment in a pressurized model with dimensions of 71 cm x 41 cm x 14 cm. Superheated steam was injected into a horizontal well 12.7cm from the bottom of the model at a rate that maintained a low pressure drop difference between the producer and injector. Experiments were conducted on two different samples, the first sample was at residual water saturation with a 14.7% initial water saturation and the second sample had an initial water saturation equal to 32%. Even though the sample with the higher initial water saturation had higher permeability and more energy injected, it was found that it had a lower oil recovery factor (by 7%) and a higher cumulative steam oil ratio (by 50%) when compared to the lower water saturation sample. From the data from the 276 thermocouples in the model, temperature contours were plotted to analyze the shape of the steam chamber. It was

found that the steam chamber for the experiment with the higher water saturation was elliptical in shape and grew faster than the circular shaped chamber in the low water saturation experiment. Figure 2.3.1 shows a schematic that compares the difference in chamber shape in the vertical plane located at mid-well between the high and low water saturation cases at late time (approximately 80% of the elapsed time into the experiment or 720 minutes). Based on the shapes, it can be seen that a larger volume of reservoir is contacted in the low water saturation case and more heat is retained in the reservoir. As expected, the thermal efficiency was better in the model with the lower water saturation – it required less steam and there was more accumulated energy within the reservoir.

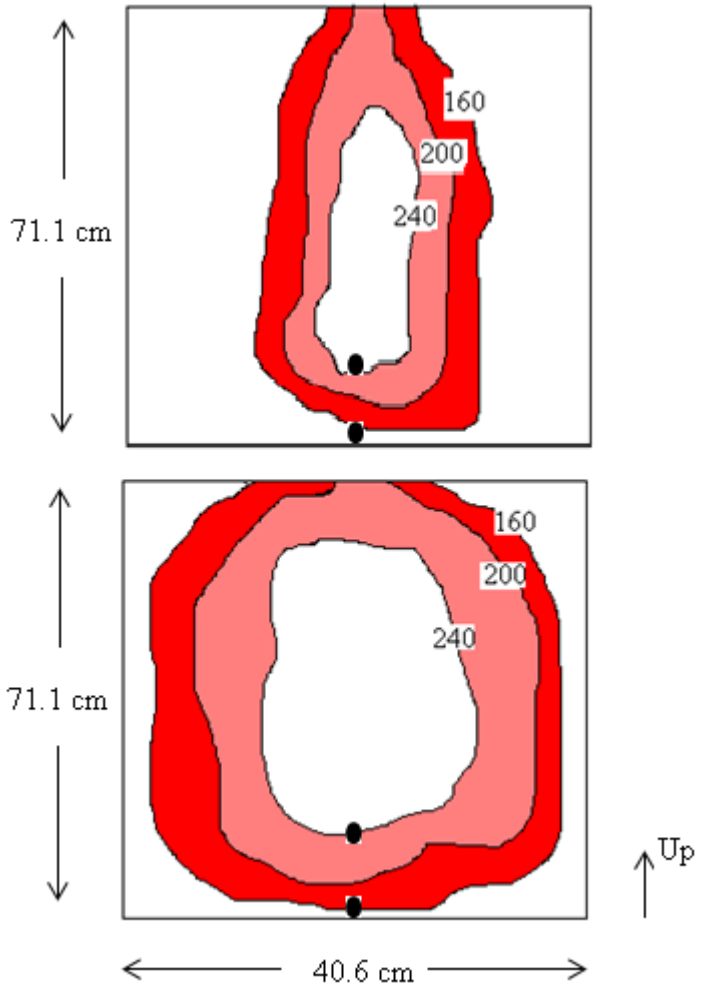

Figure 2.3.1: Schematic comparison of steam chamber growth for case with water mobility (top) and case with no water mobility (bottom) for a vertical cross section. Numbers in the diagram describe the temperature isotherms in ^{o}C.

Doan et al. (1999) used numerical simulation to analyze how the presence of water sand affects the performance of SAGD and how it affects the reservoir heat distribution. In this study, it is mentioned that for maximum efficiency of thermal project, the heat accumulated in the reservoir must be larger than the heat loss and heat produced from the reservoir. The ratio of accumulated heat to the injected heat decreases as steam is continuously injected into the reservoir.

In Doan et al.'s study, various thicknesses of top and bottom water sands were investigated. It was also found that increasing the thickness of the water sand (particularly the top water sand) resulted in much less heat accumulation within the reservoir and a much less efficient process.

When the water sands were confined (limited areal extent), it was found that the confined bottom water layer did not have a significant impact on the thermal efficiency because water coning was avoided by operating the producer at a higher pressure than the bottom water layer. The confined top water layer had a much more negative impact and it was found that there was still enough heat accumulation to offset the heat loss and heat produced from the reservoir which meant the process was still considered efficient.

When unconfined (unlimited areal extent) cases were considered, it was found that increasing the areal extent of the bottom water layer only reduced the recovery slightly. However, increasing the areal extent of the overlying water layer significantly diverts heat away from the oil zone causing steam condensation and reducing the latent heat available to advance the steam front.

In their study, the distance between the horizontal injection and production wells affected the time taken to establish communication between the wells; however it did not have any impact on the ultimate recovery.

2.4 Counter Current Flow

Nasr et al. (1998) performed a study on the counter current aspect of the SAGD process. Experiments were performed by using a cylindrical model 31 cm long x 10 cm in diameter under

adiabatic control. A control system was in place to monitor data from surface thermocouples on the perimeter of the chamber and to use heater bands to maintain the boundary temperature at the temperature of the advancing steam front. This elimination of radial heat losses is very important for accurate measurement of steam front propagation rates.

Counter-current flow, in which the steam front is moving in the direction opposite of the draining condensate, and co-current flow, in which the steam front and draining condensate flow in the same direction, were both investigated. The experiments were conducted using a sand pack with a permeability of 5 Darcies and another sand pack with a permeability of 10 Darcies to ensure repeatability of results.

In the counter-current flow case it was found that the steam front took much longer to propagate the same distance when compared to the co-current flow case. This was due to draining condensate impeding the advance of the steam front as mobilized oil accumulates on the slopes of the steam chamber in a progressively thicker layer. This type of behaviour occurs on the slopes of the steam chamber, however at the ceiling of the steam chamber, oil drains away from the front immediately after it becomes mobile. Figure 2.4.1 below shows a schematic of ceiling drainage and slope drainage in a steam chamber.

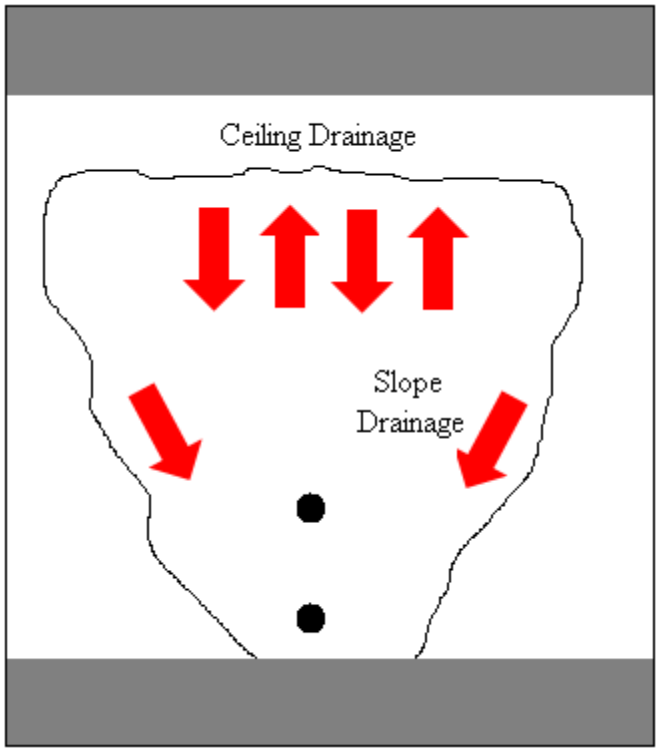

Figure 2.4.1: Schematic of ceiling drainage and slope drainage.

In their study, it was also found that the propagation rates for both permeabilities were a linear function of time (i.e. the front velocities did not change with time). The propagation rates did not appear to be a linear function of permeability.

Resultant relative permeability curves for the counter-current and co-current flow cases were generated by history matching the experimental results with a numerical simulation model. The primary matching parameters were steam front propagation rates and development of temperatures with time. As expected, for any given water saturation the relative permeability curves for the co-current case were higher than the counter-current case.

2.5 Residual Oil Saturation

Walls et al. (2003) investigated residual oil saturation inside the steam chamber during SAGD by modifying relative permeability exponents to match the analytical residual oil saturation presented by Cardwell et al. (1942). It is noted by the author that two flow regimes were observed during the experiment of Cardwell et al.

To obtain a proper match, a hybrid gas-liquid relative permeability curve was generated. The first portion of the curve described the behaviour at the edge of the steam chamber where fluids drain quickly. The second portion of the curve described the behaviour within the steam chamber itself where drainage occurs more slowly. A sensitivity study was performed by using numerical simulation and it was found that higher injection pressures resulted in lower residual oil saturations.

As detailed in the preceding literature review, a considerable amount of research has already been conducted to understand the SAGD process, much of which is theoretical or has been focused at the laboratory scale level. Up until now, validation of theory using field trials has been limited because SAGD is a relatively new technology, and there has not been a large amount of data available. In general, the models described in literature target the understanding of a particular mechanism or issue, and do not unify the individual components that are required to accurately predict SAGD performance at a field level.

For this thesis, an extensive dataset of field performance and reservoir data specific to Firebag was used. This data included 4D seismic interpretation, core studies, viscosity tests, geological

parameters, and monthly fluid and pressure data. All of these sources of data were used to improve the accuracy of input data and to extend the models that have been presented in literature. In particular, this work makes use of in situ measurements such as residual oil saturation and steam chamber velocity using 4D seismic has not been used previously and is significantly different than the lab derived values used in literature. This allows for a more rigorous approach to develop a more robust model for predicting SAGD performance at Firebag with greater certainty.

CHAPTER 3: DEVELOPMENT OF ANALYTICAL MODEL FOR OIL DRAINAGE RATE

Here, a modified version of Butler's models is combined to model SAGD performance throughout its three main stages: rising chamber stage, lateral depletion stage, and coalescing steam chamber stage. Collectively, the analytical expressions presented in the previous section by Butler et al. covers the entire life cycle of a SAGD operation. The oil rate equation, Equation 2.1.18, describes vertical growth of the steam chamber corresponds to early time when steam injection has begun and the chamber is beginning to develop but has not yet reached the top of the reservoir. Since this expression is ever increasing, it is only valid to a maximum drainage rate predicted by the TANDRAIN or LINDRAIN assumptions.

The drainage rate equation from the TANDRAIN or LINDRAIN assumptions, Equation 2.1.7 with the constant equal to 1.5 and 1.3, are valid for the mid-life of the well, after the steam chamber has reached the top of the reservoir and before steam chambers have coalesced with the adjacent steam chambers on a well pattern. As shown below, the LINDRAIN result provides for a lower oil rate and appears to represent the behaviour of field SAGD performance better than that of the TANDRAIN model.

For the late-time phase of the life of a SAGD wellpair when the chambers are merging, the TANDRAIN or LINDRAIN depletion models can be applied to predict the reduction in drainage rate after the steam chambers on a well pattern have coalesced. As shown below, the TANDRAIN model appears to perform better for this stage of the process.

The drainage rate equations for each of the three phases of the analytical model presented by Butler (as described in the Chapter 2) were applied to the Firebag project to determine their suitability in a practical field application. The rising chamber model was used for the vertical growth phase, the LINDRAIN model was used for the lateral growth phase, and the TANDRAIN model was used for the depletion phase. The novelty of the model used here lies in the complete parameterization of the properties required in analytical models versus temperature and the link of the data to log, core, and seismic data. It was determined that the oil drainage rate profile that matches the field data the best is obtained by taking the minimum of the predicted drainage rate for the three phases.

The input variables required for the analytical model are as follows:

- permeability,
- pay thickness,
- porosity,
- initial oil saturation,
- kinematic viscosity,
- thermal diffusivity,
- well length,
- well spacing,
- viscosity exponent, *m*, and
- residual oil saturation.

Each one is described in more detail in the following subsections.

3.1 Permeability

Due to the nature of unconsolidated sandstone, permeability is one of the variables with the largest ranges of uncertainty for bitumen projects. Absolute permeability measurements are

typically derived in lab tests from core samples and generally involve separating the bitumen from the sand and then repacking the sand before the permeability testing is conducted with gas or other fluids. In this process, sand grain geometry is changed and may not be representative of in situ permeability. The source of the core samples for these lab permeability tests are core holes that are typically drilled at a spacing of approximately 16 wells per section which means that there are approximately 400 meters of reservoir between known data points within the reservoir. There can be a high level of variability between these known data points; a given vertical cross section within the reservoir will show a different distribution of high permeability sands as well as low permeability muds and shales.

To obtain a representative value of the absolute permeability for use in the analytical model, the laboratory-derived permeability data from the cored vertical wells from the top of the reservoir to the producing well level have been used to provide a geometric average value of the absolute permeability. The average permeabilities derived from the core data is listed in Table 3.1.1.

Table 3.1.1: Firebag core data generated permeability.

Pad	Core Data Average Permeability (D)
Pad 1	2.35
Pad 2	2.30
Pad 3	2.25
Pad 4	2.40
Pad 7	2.38

The effective permeability is the product of the absolute permeability and the relative permeability. It is also the value that is used in the analytical expressions for calculating oil drainage rate so the relative permeability also needs to be considered. At the steam chamber

interface on the slopes of the steam chamber, where condensate is flowing downwards and steam is flowing upwards, interactions between the various flowing fluids imply that there will be significant relative permeability effects. Butler (1994) suggested a suitable average relative permeability for the oil phase equal to 0.40 is representative of conditions, on average, at the edge of the steam chamber. Reis (1992) also used similar values – in his linear drainage model he assumed the oil relative permeability was 0.48. Here, an inverse cubic relative permeability model based on a fractional flow of water was applied:

$$k_{ro} = \frac{1}{\left(\left[\left(\frac{1}{f_w}-1\right)\frac{\mu_o}{\mu_w}\right]^{\frac{1}{3}}+1\right)^3} \qquad (3.1.1)$$

Since water-to-oil ratios are available from Firebag historical performance, estimates of overall representative values of the oil relative permeabilities, with respect to water, can be estimated. For example, for Pad 101 the production water-to-oil ratios over the life of the pad gives representative oil relative permeabilities with respect to water between 0.36 and 0.49 by using Equation 3.1.1.

The viscosity of water used in Equation 3.1.1 was calculated from (Farouq Ali, 2010):

$$\mu_w = -0.0123274 + \frac{27.1038}{T} - \frac{23527.5}{T^2} + \frac{1.01425\times10^7}{T^3} - \frac{2.17342\times10^9}{T^4} + \frac{1.86935\times10^{11}}{T^5} \qquad (3.1.2)$$

and the oil viscosity was calculated from Equation 3.5.1, described below.

3.2 Pay thickness

To determine pay thickness in the McMurray channel at Firebag, pay cut offs are applied such that only portions of the reservoir that are suitable for recovery by using SAGD are included.

These cut offs are given by gamma ray (GR) <60°API, resistivity > 10 ohm·m, fractional porosity >0.22, and fractional water saturation <0.50 and define the net pay thickness. Portions of the reservoir that are within the McMurray channel but do not meet these cutoffs are not considered to be of sufficiently good quality for recovery by using SAGD.

The original theory was derived from laboratory experiments that did not make a distinction between gross pay and net pay, i.e. the net-to-gross ratio was effectively equal to one since in the experimental apparatus, the oil sand was essentially homogeneous and of good quality. In reality, the net-to-gross ratio is generally less than one because there is the presence of non pay facies, for example, mud, shale, inclined heterolithic strata, and other heterogeneities within the reservoir. It can be argued that gross pay thickness should be used in the model because it would likely be the entire height of the reservoir that provides the driving mechanism under gravity drainage. Using the net pay thickness results in less head available for gravity drainage and therefore a lower oil drainage rate. However, using the gross pay thickness will result in an oil drainage rate that is too high because the presence of non pay facies, in other words, non-productive reservoir rock, within the reservoir will result in slower heating, heat losses to non-productive rock, and retarded oil drainage. Thus, here, it was decided that the suitable pay thickness to be used in the current model is the net pay thickness as provided by the pay cut off criteria listed above.

Another consideration for pay thickness is the continuity of the reservoir pay. Shale or mud barriers that are interpreted to be laterally continuous can prevent steam chamber growth. It is

expected that laterally continuous barriers that are 1 to 2 meters thick can prevent steam rise and reservoir pay thickness above these barriers should not be included.

An wireline type log for a vertical well at Firebag is shown in Figure 3.2.1. The application of cutoffs for porosity, resistivity, saturation, and gamma ray as mentioned above for determining net pay thickness are shown in the figure. The bulk mass fraction of oil (BMFO) from core analysis is also overlain on the wireline logs. Based on the rock and fluid densities for the McMurray formation, a water saturation value of 0.50 corresponds to a BMFO of approximately 8% (as indicated in the figure). It should be noted that there are sections of core that were not successfully retrieved which explains the lack of BMFO data at select intervals throughout the zones logged by the wireline log.

As described above permeability was the parameter that was varied within the model to match the historical oil production rates. A higher permeability with a lower pay thickness would be equivalent to a lower permeability with a higher pay thickness. If using a net pay thickness is an assumption that is too conservative, the vertical permeability will be increased to account for it. This is consistent with the use of the transmissibility, *kh*, the product of the permeability and net pay, sometimes referred to as the flow capacity, commonly used in reservoir engineering analysis.

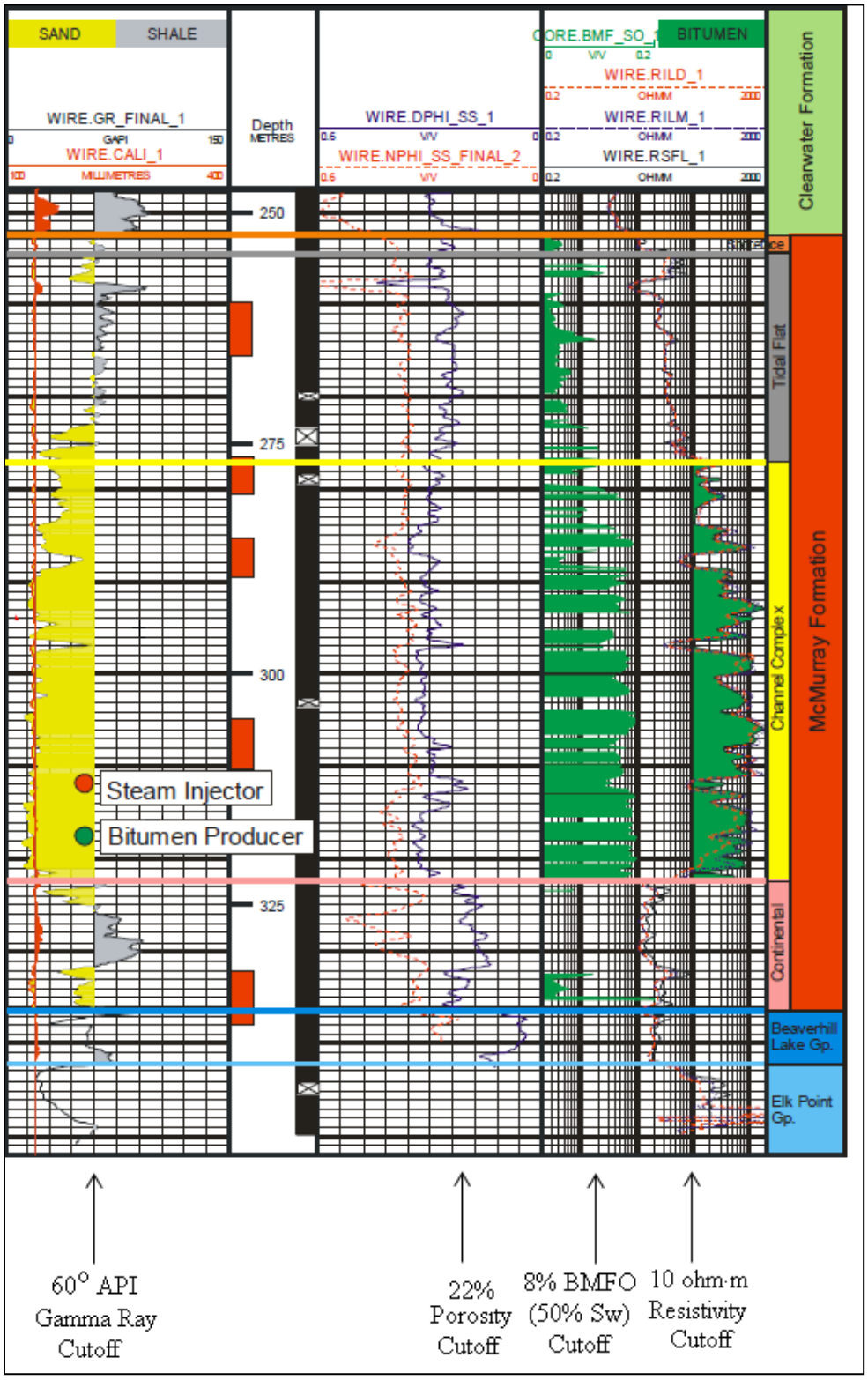

Figure 3.2.1: Wireline logs for a Firebag Type well (gamma, neutron and density porosity, resistivity) with bulk mass fraction of oil from core overlain (courtesy of Suncor, 2012).

3.3 Porosity

The representative value of the porosity is derived from vertical well logs within the Firebag property by using the arithmetic average. Neutron and density porosity logs have both been used in the determination of porosity. The porosity is associated with the net pay so the same cutoffs are applied to the net pay before determining the porosity, that is, GR <60°API, fractional porosity >0.22, and fractional water saturation <0.50. This means that the average porosity is determined from parts of the reservoir where the porosity is greater that 0.22.

As per the 2012 Firebag annual performance presentation made by Suncor to the AER (Suncor, 2012), the porosity generally falls within a fairly narrow range from 0.31 to 0.34 for Pads 101, 102, 103, 104, and 107.

3.4 Initial Oil Saturation

The initial oil saturation is given by unit complement of the initial water saturation, that is, $S_{oi} = 1-S_{wi}$. The total water saturation within the pay zone is derived from vertical well logs by using Simandoux's (AER, 2012) method and core data. Core data provides the bulk mass fraction of oil (BMFO) from analysis of core plugs; the BMFO is converted to the oil saturation by using the densities of oil, water, and reservoir sand. Values for the initial oil saturation range from approximately 0.84 to 0.87 for Pads 101, 102, 103, 104, and 107 as per the 2012 Firebag annual performance presentation made by Suncor to the AER (Suncor, 2012).

3.5 Kinematic Viscosity

The viscosity of Athabasca bitumen has been measured in many published laboratory studies. In December 2005, the first phase of a joint industry project (various operating companies) was conducted by the Alberta Research Council (ARC) on bitumen from Suncor's Mackay River and Cenovus' Christina Lake oil sands properties. The viscosity measurements were limited by the operating range of the viscometer so readings were only available to 150°C in the series of experiments conducted.

The second phase of the study was conducted in May 2007 and the study was expanded to include Surmont bitumen. Viscometer equipment was improved and allowed for readings higher than 150°C. It was found in this study that temperature has a much greater effect on oil viscosity than the degree of methane saturation. Based on this study it is assumed that the contributions from using live oil viscosity are not significant so using dead oil viscosity in oil production model applied here appears to be a valid assumption. It is also noted by Farouq Ali (2010) that the volume of solution gas in very heavy oils is very small and based on his provided correlation, the effect of solution gas would be insignificant when compared to the temperature effect on viscosity. In addition to the ARC studies, other viscosity tests were also conducted by ARC (2005) , Hycal (2006), and the PRI Consortium (1999). Viscosity measurements as a function of temperature were compared between the different sources of information and resulted in very similar findings as shown in Figure 3.5.1. A regression analysis was performed by using a power function and the resultant line of best fit of dynamic viscosity versus temperature yielded a very small determination of coefficient ($R^2 = 0.98$); the correlation is given by an equation of the form:

$$\mu_o = aT^{-b} \qquad (3.5.1)$$

The dynamic viscosity was converted to kinematic viscosity by dividing dynamic viscosity by oil density. The correlation for oil density versus temperature was taken from Farouq Ali (2010):

$$\rho_o = \frac{\rho_{O,SC}}{1+\frac{T-68}{1047}} \qquad (3.5.2)$$

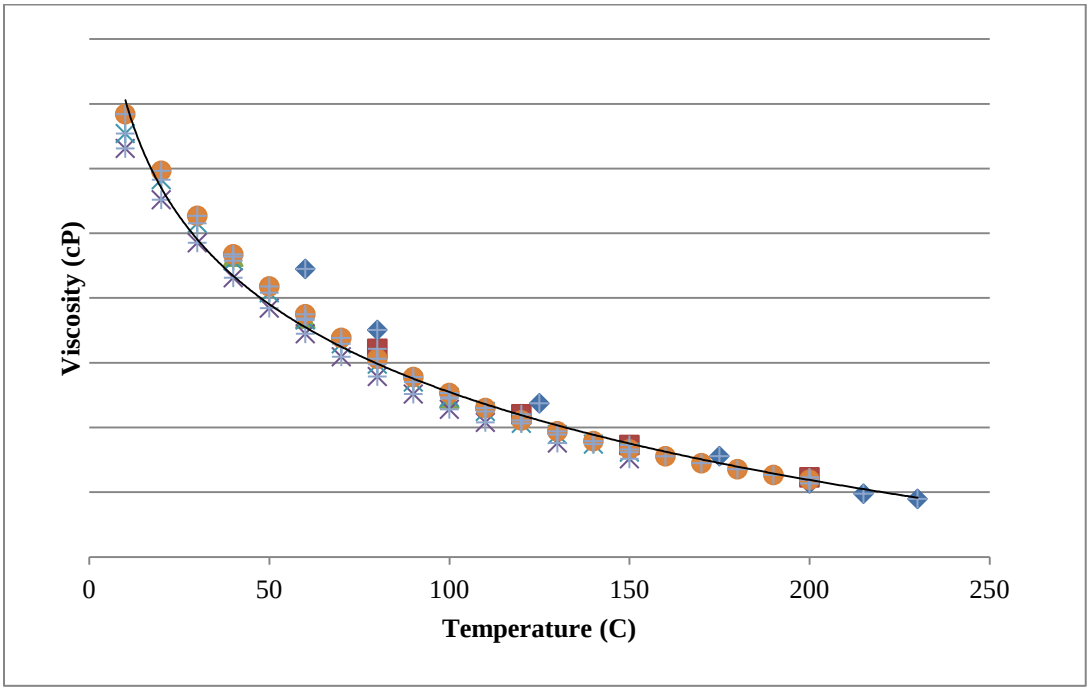

Figure 3.5.1: Profiles of dynamic viscosity as a function of temperature from various lab measurement sources. Y axis intentionally omitted due to confidentiality.

3.6 Thermal Diffusivity

The thermal diffusivity, α, is defined as:

$$\alpha = \frac{k_h}{M} \qquad (3.6.1)$$

where k_h is the thermal conductivity and M is the volumetric heat capacity of the oil sands. The thermal conductivity of oil sand can be estimated from (Tikomirov, 1968):

$$k_{t,ob} = \frac{11.007 e^{0.6[2.65(1-\varphi)+ S_l]}}{(T+273.15)^{0.55}} \quad (3.6.2)$$

where ϕ is the fractional porosity, S_l is the liquid saturation, and T is the temperature in °C and the thermal conductivity is given in units of kW/m^{o}C. In general, the thermal conductivity of reservoir rock decreases as temperature and porosity increase and increases as liquid saturation increases. This thermal conductivity is defined for the overburden and is consistent with the work on thermal conductivities of water-saturated sandstone presented by Somerton (1958). It should be noted that 100% water-saturated sandstone has a thermal conductivity of approximately 2.755 W/m°C.

The volumetric heat capacity, *M*, of fluid-saturated rock is a function of the porosity, density, saturation and specific heat capacity of the fluids within the rock. The reservoir volumetric heat capacity is different from the volumetric heat capacity of the overburden due to different fluid saturations and porosities, however both the reservoir and overburden are governed by the same expression given by:

$$M = \varphi\rho_o c_o S_o + \varphi\rho_w c_w S_w + (1-\varphi)\rho_r c_r \quad (3.6.3)$$

where ρ_*, c_*, and S_* are the density, specific heat capacity, and saturation of phase *, respectively, and the subscripts *o*, *w*, and *r* refer to the oil, water, and rock (sand) phases, respectively. Specific heat capacities of various fluids are functions of temperature and density and they can be estimated from (Farouq Ali, 2010):

$$c_o = \frac{1.6848+0.00391T}{\gamma_o} \quad (3.6.4)$$

$$c_w = 4.3245 - 3.696 \times 10^{-3} T + 2.482 \times 10^{-5} T^2 \quad (3.6.5)$$

For reservoir sand, a constant value is used equal 0.77kJ/kg°C (Somerton, 1958).

3.7 Well Length

Well lengths were obtained from completion data for the wells within the Firebag property. The length of slotted liner of each production well, that is, the length of the well open to flow, was used for the well length. Tables 3.7.1 and 3.7.2 list the well lengths for producer wells used for this study by well pad.

Table 3.7.1: Average well length by pad.

Well Pad	Average Well Length
101	993
102	989
103	1092
104	995
107	949

In addition to a breakdown at the pad level, time-lapse 3D seismic and observation wells have indicated that individual steam chambers have coalesced into larger chambers that span more than one pad. These macro level steam chambers include wells and well pads that have been identified to operate as a single larger steam chamber entity. Well lengths and the wells that comprise each macro level chamber are listed in Table 3.7.2.

Table 3.7.2: Average well length by macro level steam chamber.

Chamber	Average Well Length (m)	Pads Included
NE Chamber	1,038	Pad 101 North, Pad 102 North, Pad 103
South (Base)	1,000	Pad 101 South and 2P6, 2P7, and 2P8
West	968	Pad 104 and 107

Suncor generated 4D seismic interpretations (Suncor, 2010, 2011) shows the coalescing behaviour of these macro level steam chambers in Figures 3.7.1 and 3.7.2. These are included to qualitatively show the chamber growth with time and the colours indicating chamber thickness cannot be compared directly because the scales are not the same between the two figures.

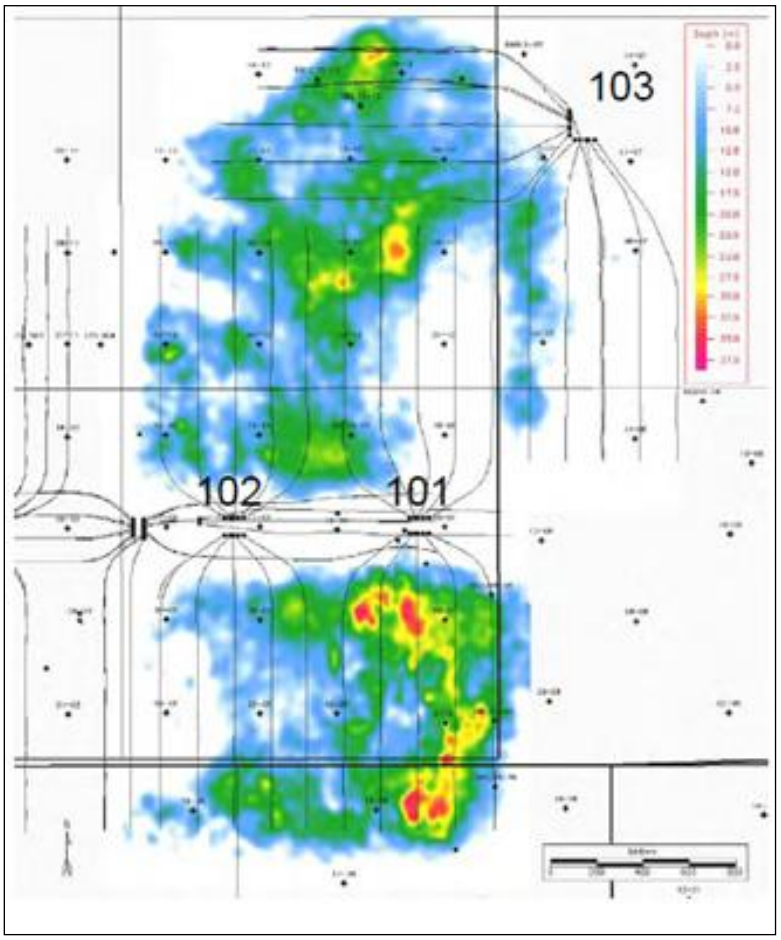

Figure 3.7.1: 4D seismic interpretation of steam chamber thickness for Firebag Pads 101, 102, 103 (courtesy of Suncor, 2010). Chamber thicknesses range from 0 m (white) to 40 m (red).

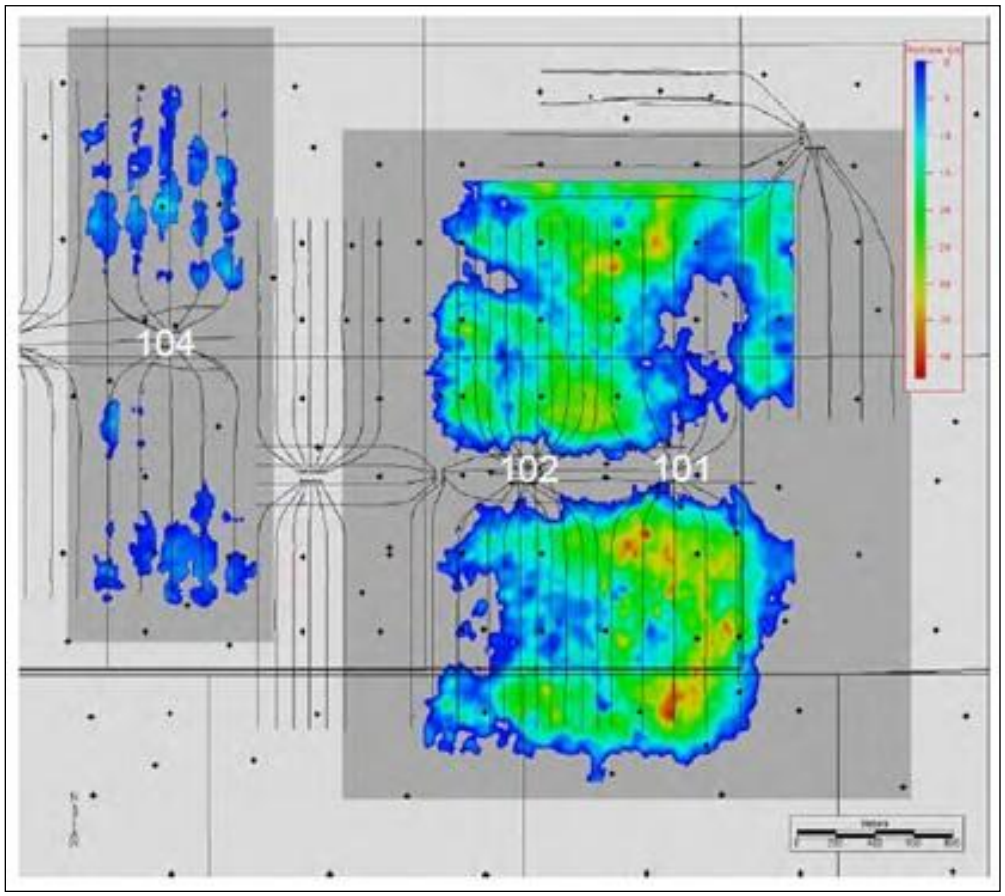

Figure 3.7.2: 4D seismic interpretation of steam chamber thickness for Firebag Pads 101, 102, 104 (courtesy of Suncor, 2011). Chamber thicknesses range from 0 m (blue) to 40 m (red).

It is still too early to see the same coalescing behaviour in the steam chambers for the west pads (Pad 104 and 107) however they are immediately adjacent to each other and the production data that will be shown later in this study appears to validate this assumption.

3.8 Well Spacing

The average inter-well pair spacing on Pads 101 to 104 is constant at about 160 meters whereas the inter-well pair spacing on Pad 107 is equal to about 90 meteres.

3.9 Viscosity Coefficient (m)

As described in Chapter 2, Equation 2.1.11 was presented to permit estimation of the value of *m*, the sensitivity of the change of the oil viscosity with respect to temperature, given the viscosity temperature curve for the oil, the steam temperature, and the initial reservoir temperature.

For the Firebag area, a specific value of *m* can be calculated given the initial reservoir temperature at Firebag, equal to about 8°C, and the expected steam temperature based on the Firebag SAGD operation pressure. The viscosity of the bitumen at reservoir conditions is many orders of magnitude higher than the bitumen at steam temperature so Equation 2.1.11 can be simplified to:

$$\frac{1}{m\nu_s} = \int_{T_R}^{T_S} \frac{dT}{\nu(T-T_R)} \qquad (3.9.1)$$

When the expression for kinematic viscosity for Firebag bitumen, presented above, is substituted into Equation 3.9.1, *m* can be found as a function of temperature by evaluating the above integral. The integral can be evaluated by using numerical integration and yields a relationship between the viscosity coefficient, *m*, and the reservoir temperature as shown in Figure 3.9.1. The operation pressure of the Firebag reservoir yields a fairly narrow range of steam temperatures that result in an approximate range of *m* between 4.10 and 4.15. This is consistent with a value of $m = 4$ which has been suggested by Butler to be a valid assumption for Athabasca bitumen.

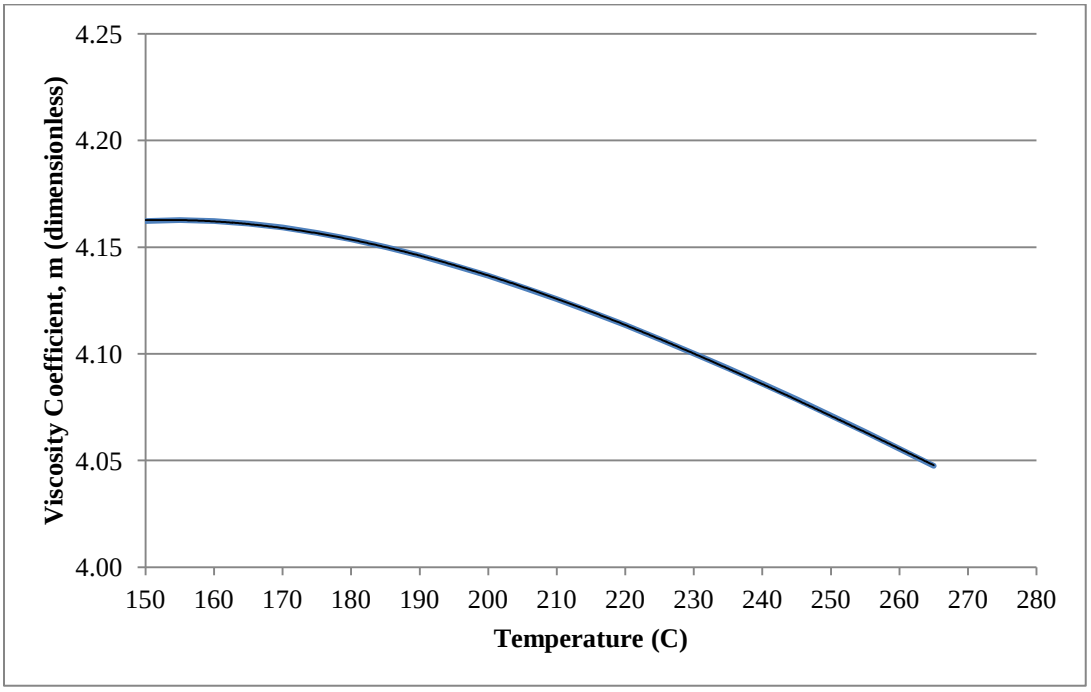

Figure 3.9.1: Butler viscosity coefficient, m, as a function of temperature for Firebag bitumen.

3.10 Residual Oil Saturation

The residual oil saturation in the model was based on a 4D seismic analysis conducted by Frank Sun, a geologist on the Firebag Asset Team at Suncor (Sun, 2012). The volume of the steam chamber for each half pad was determined by time-lapse 3D seismic interpretation of the disturbed zone. The original oil in place was determined by using log and core data for the net pay above the production well. The residual oil saturation was then estimated by subtracting the cumulative oil production from the original bitumen in place within the steam conformance zones.

The SAGD wellpads used in the analysis were Pads 101, 102, 103, and 104 which began operation in 2003, 2003, 2005, and 2009, respectively. Each of these pads were at a different

stage of SAGD production, having produced between 13% and 51% of the original bitumen in place based on continuous net pay. There was no strong correlation between the time elapsed since first production and residual oil saturation as shown in Figure 3.10.1.

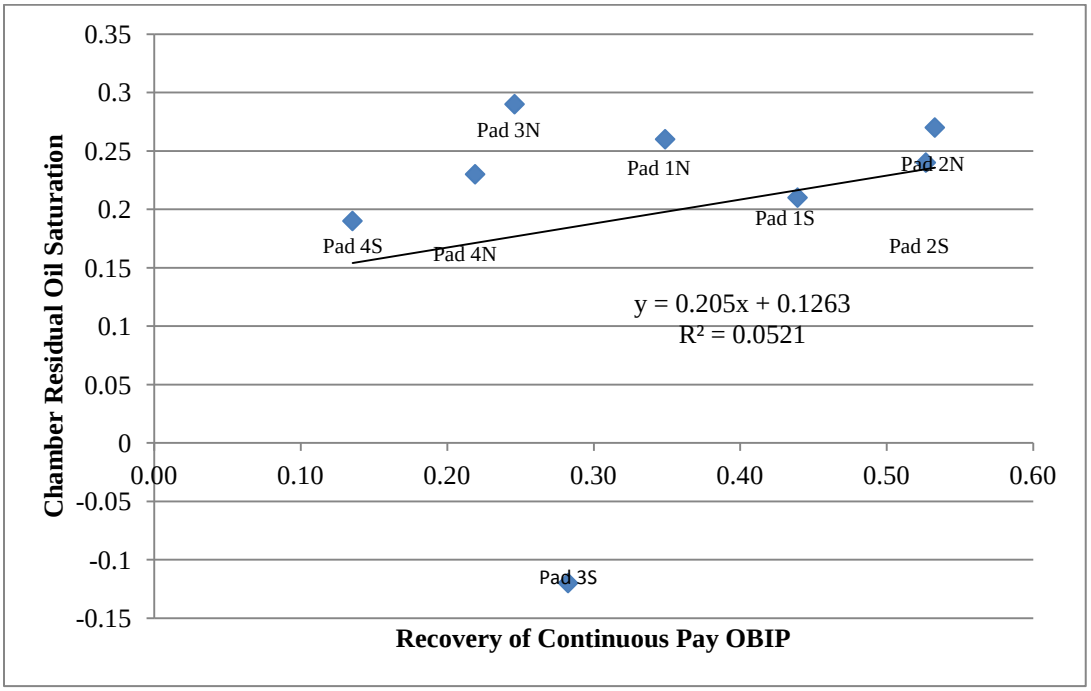

Figure 3.10.1: Residual oil saturation within Firebag half pad steam chambers as a function of cumulative bitumen recovery.

The negative residual oil saturation associated with Pad 103 South is indicative of the pad producing oil from Pad 101 North. The cumulative production from Pad 103 Wellpair 5, which is adjacent to Pad 101 North, is among the highest on Pad 103 South, producing more oil (~679,000 m^3) than the other 4 well pairs on Pad 103 combined (~595,000 m^3). This can also be considered as evidence that there is fluid mobility between the drainage areas of adjacent pads.

The residual oil saturation appears to be relatively independent of time as per the data obtained. This is different than the residual oil saturation suggested by Cardwell et al., estimated from Equation 2.1.8, which when used to forecast a Firebag SAGD well pair results in a residual oil saturation of 0.25 in early time, declining to 0.08 near the middle of life for a typical Firebag SAGD well pair.

The relatively high values of residual oil saturation shown in Figure 3.10.1 appear to contradict analyses performed on cored steam chambers which demonstrate approximately 5-10% or less residual oil saturation. However, the methodology used in this case is an average value throughout the entire steam depletion chamber. There would likely be an oil saturation gradient within the chamber itself; near the injector there would be a lower residual oil saturation and at the top and side edges of the chamber there would be a higher residual oil saturation.

This is supported by the work of Cardwell et al. (1942) which noted the presence of two separate flow regimes in gravity drainage. A numerical simulation study on residual oil saturation in SAGD by Walls et al. (2003) also found that two separate flow regimes needed to be modeled to accurately predict SAGD performance. The first regime is related to the edge of the steam chamber where fluids drain quickly and the second regime is related to the inside of the steam chamber itself where drainage occurs more slowly. The relative permeability curve end points from the counter current drainage analysis performed by Nasr et al. (1998) also suggests that higher residual oil saturations will result from the counter current drainage process in SAGD.

It may be also be expected that the residual oil saturation will begin to decrease further near the end of well as time progresses because the steam chamber edges will disappear as adjacent steam chambers fully coalesce. In addition, the ceiling drainage rate will probably also decrease over time as the steam chamber fully conforms with the top of the reservoir.

3.11 Results

The above parameters for Firebag pads 101, 102, 103, 104, and 107 were input into the model and resultant oil drainage rate profiles were created for each pad. The model was created and executed in Microsoft Excel.

Since permeability is the variable with the highest uncertainty within the analytical model it is used in this study as the single adjustable parameter for matching the historical performance for Firebag wells. The effective vertical permeability that is required to arrive at a match is in the same order as those permeabilities derived from the core data. A comparison between the permeabilities required to realize the match and the permeabilities extracted from the core data is listed in Table 3.11.1.

After the match to historical production data was obtained, the resultant permeability was compared to the oil saturation values of each respective well pad. It was discovered that there was a very strong correlation between effective vertical permeability and initial oil saturation as shown in Figure 3.11.1. This is not surprising considering that the facies contributing to lower oil saturation are generally muds and shales which would reduce vertical permeability.

Table 3.11.1: Comparison of matched permeability with Firebag core data.

Pad	Core Data Average Permeability (D)	Matched Permeability (D)
Pad 1	2.35	2.75
Pad 2	2.30	1.75
Pad 3	2.25	2.20
Pad 4	2.40	2.60
Pad 7	2.38	2.10

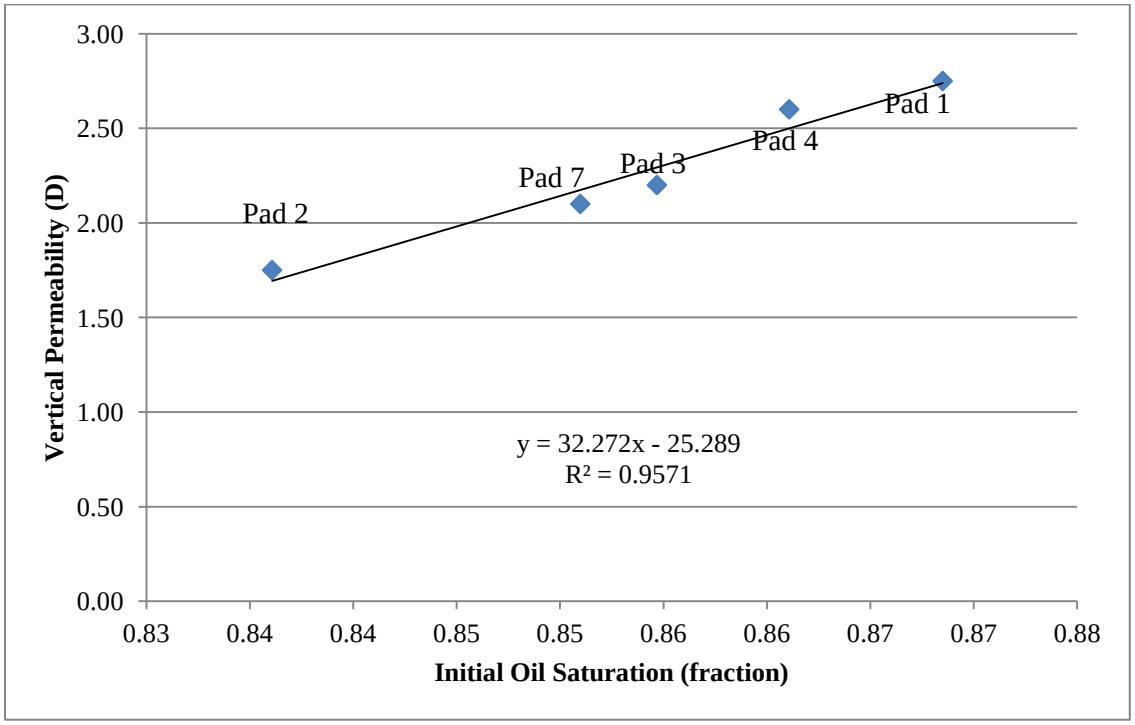

Figure 3.11.1: Vertical permeability as a function of initial reservoir saturation for Firebag producing pads.

Historical SAGD production is subject to fluctuations due to operational issues so the match on instantaneous oil drainage rate will never be predicted exactly by the model since it does not take these issues into account. These issues can include changes in day-to-day operating conditions or even larger issues such as pump repair and maintenance, or even production constraints, for

example, those imposed in 2009 by the AER due to the production of H_2S). A better gauge of a reasonable history match can be seen on the plot of cumulative oil where much of the noise associated with operation has been filtered out.

Figure 3.11.2 shows the oil drainage rate profiles plotted for each of the three phases: growth, spreading, and depletion, (Equations 2.1.18, 2.1.7, and 2.1.12, respectively), described above by using Pad 101 properties at Firebag as an example. The oil drainage rate profiles for the other pads at Firebag are similar in nature. As can be seen, the oil drainage rates for each phase overlap with each other, however the final oil drainage rate profile is obtained by taking the minimum of the predicted drainage rate for the three phases.

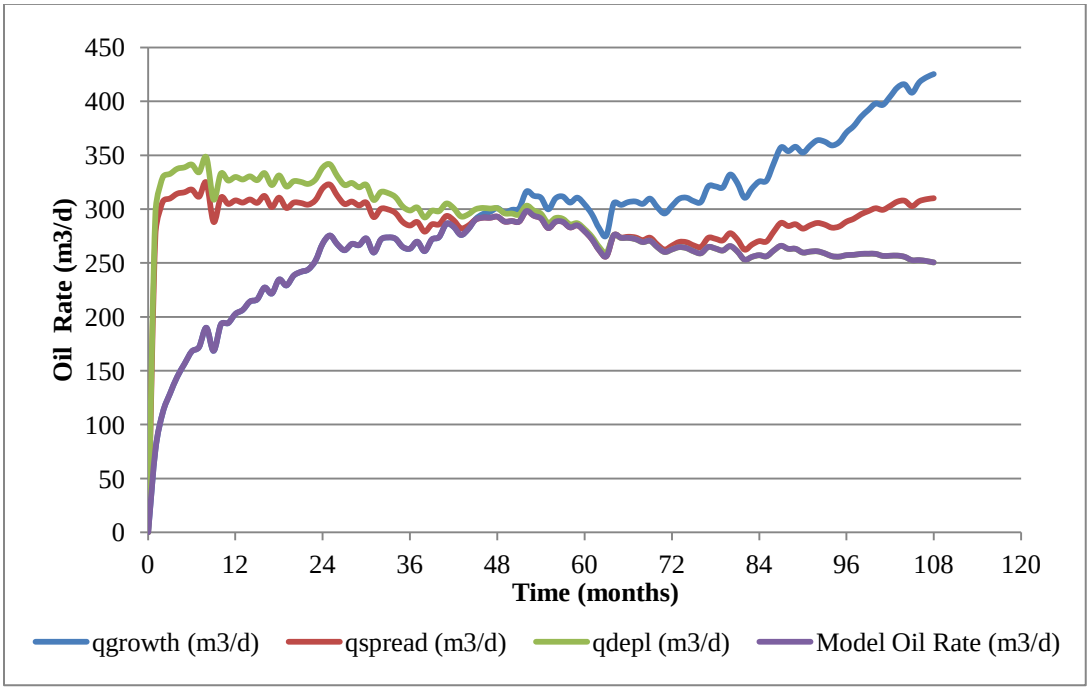

Figure 3.11.2: Final oil drainage profile (and individual components) from the analytical oil drainage model for Firebag Pad 101. Individual components: q_{growth} is associated with Equation 2.1.18, q_{spread} is associated with Equation 2.1.7, and q_{depl} is associated with Equation 2.1.12.

A comparison between actual field data and the analytical model prediction is shown on both an instantaneous and cumulative basis in Figures 3.11.1 through 3.11.5 for Pads 101, 102, 103, 104, and 107. Plots are also included for the macro steam chamber level and are shown in Figures 3.11.6 through 3.11.8. The groupings for the macro steam chamber level are described in Section 3.7.

It should be mentioned that due to the lack of pressure history in the early life of the Firebag property (prior to 2005), reasonable values have been assumed but they are not actual measured data. For this reason, less emphasis should be placed on the match in the oil rate for the first two years of Pads 101 and 102. The historical production shown in the plots below have been normalized to the first production date for all of the well pads and macro level steam chambers. This has been done to reflect the fact that not all wells on a pad are started up at the same time and results in a more accurate reflection of actual field performance. The plots are shown for a single well pair for each pad or macro level steam chamber. Each single well pair plot uses arithmetically averaged input parameters for all of the individual wells in each pad or macro level chamber (i.e. pay thickness, permeability, well length, porosity, liquid saturations). The historical data is normalized such that the production for each well begins at time 0 even though the wells may have started up at different times.

The combined analytical models take detailed input parameters that vary with temperature into account which reflects variable operating pressure. Due to the simple nature of the closed form expressions of the analytical model, it is not expected that there will be a perfect match to the actual field history. Operational issues and equipment/measurement limitations cannot be

completely captured by any model. However, based on the reasonable matches that are obtained, it appears that the theory behind the analytical model is sufficient for capturing the primary mechanisms that are involved in the SAGD process.

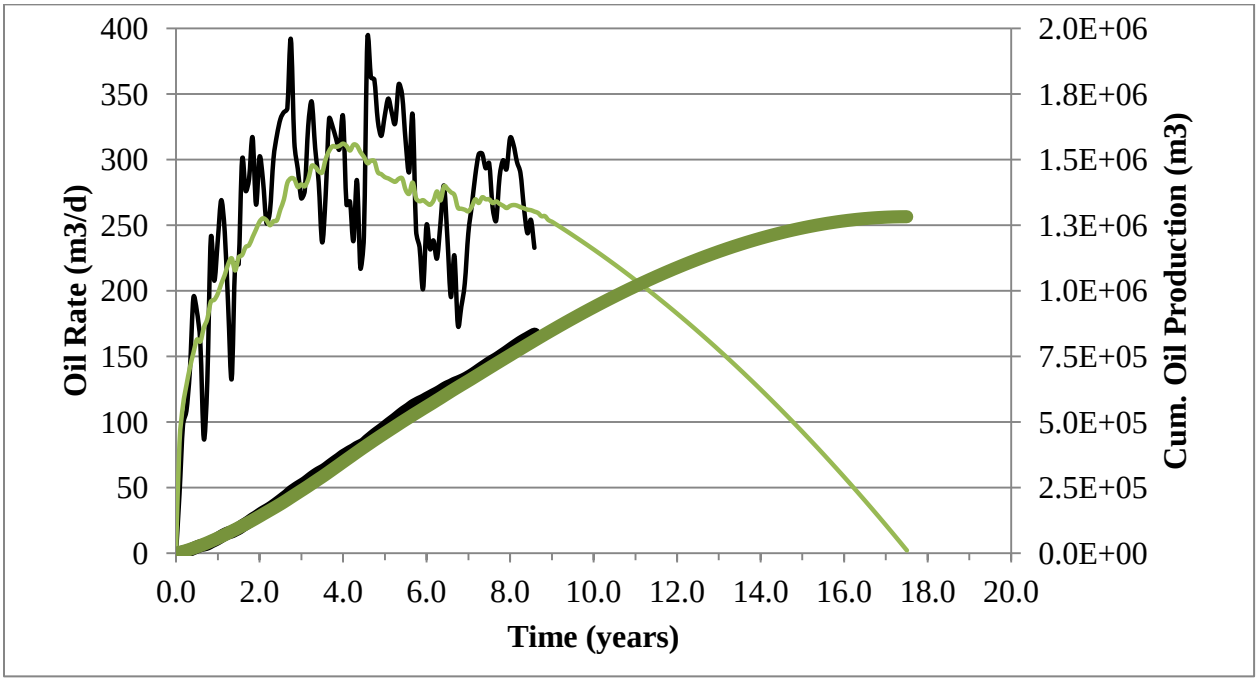

Figure 3.11.3: Comparison of historical production to oil drainage rate from analytical model for Firebag Pad 101 .

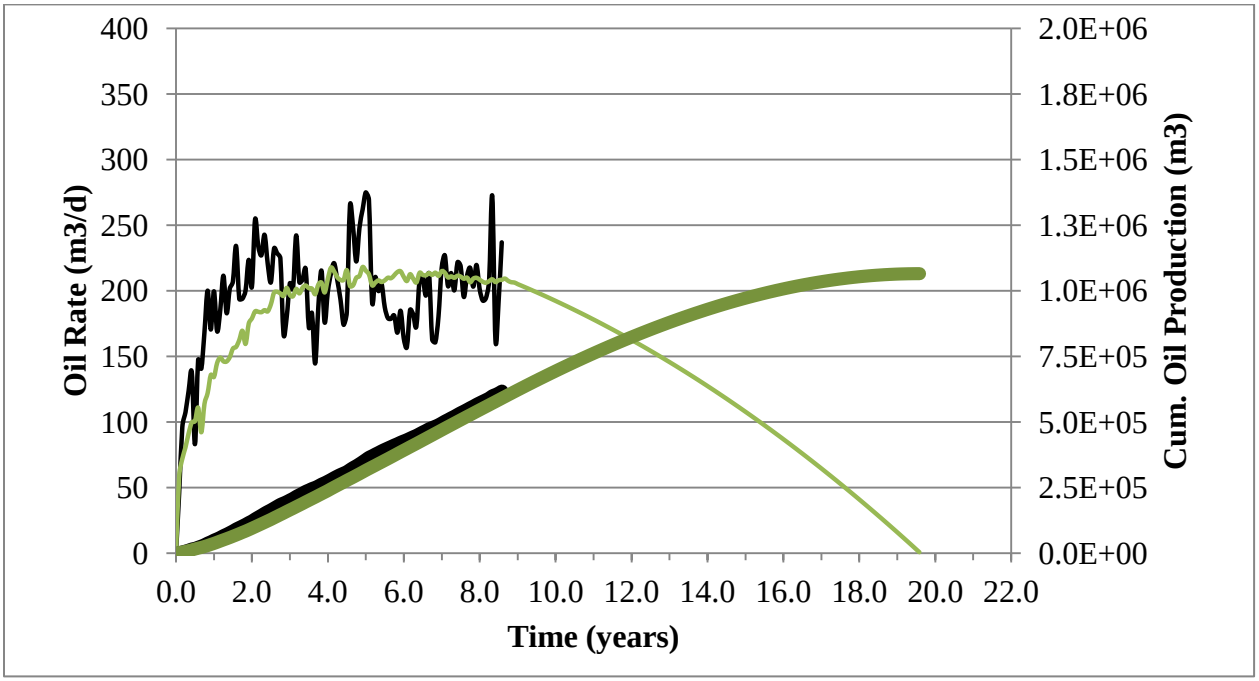

Figure 3.11.4: Comparison of historical production to oil drainage rate from analytical model for Firebag Pad 102.

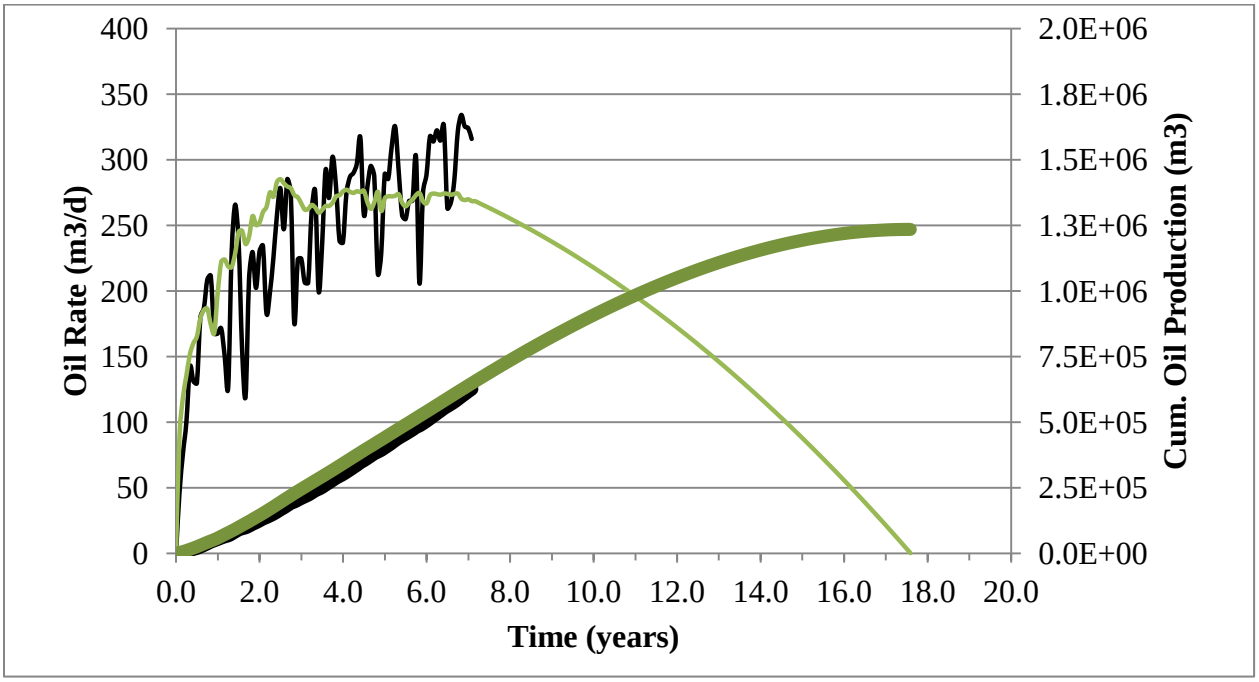

Figure 3.11.5: Comparison of historical production to oil drainage rate from analytical model for Firebag Pad 103.

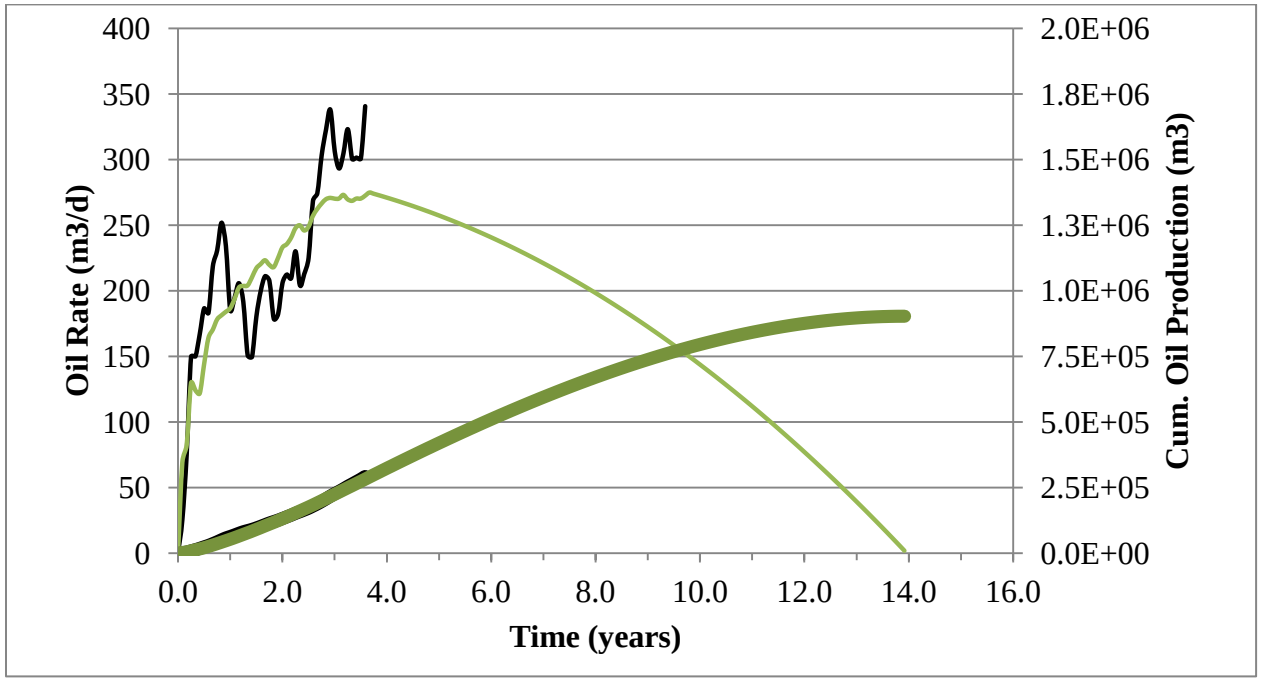

Figure 3.11.6: Comparison of historical production to oil drainage rate from analytical model for Firebag Pad 104.

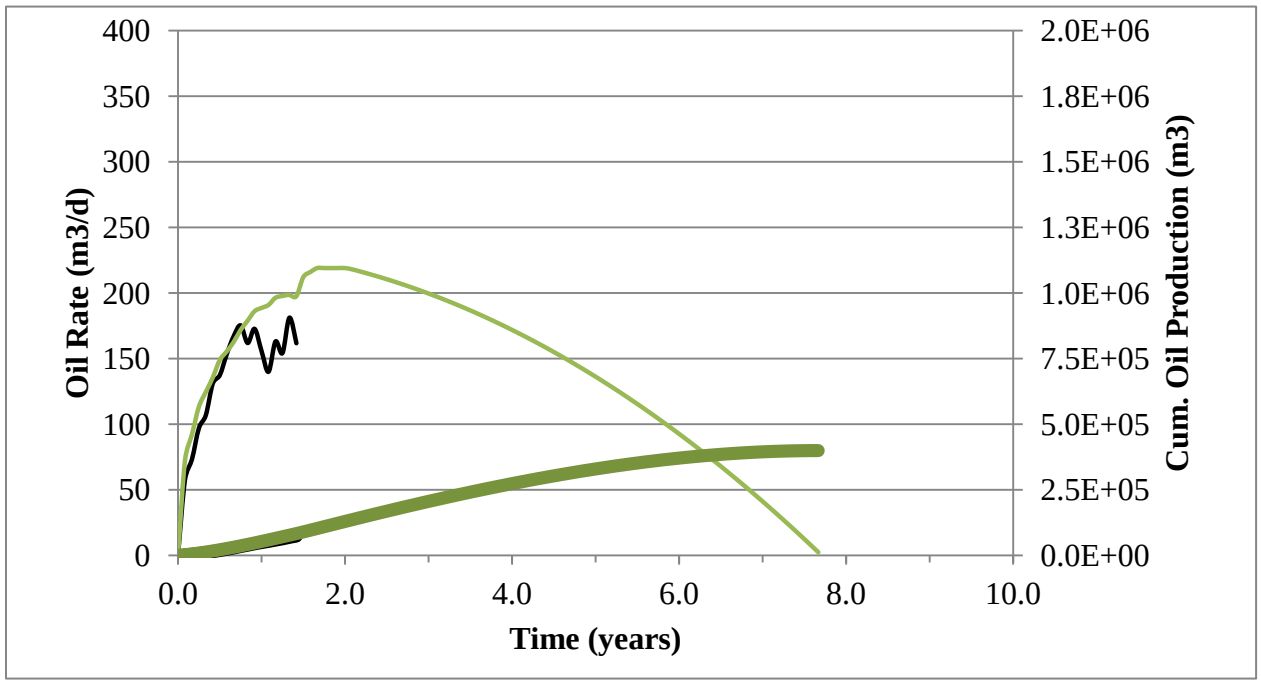

Figure 3.11.7: Comparison of historical production to oil drainage rate from analytical model for Firebag Pad 107.

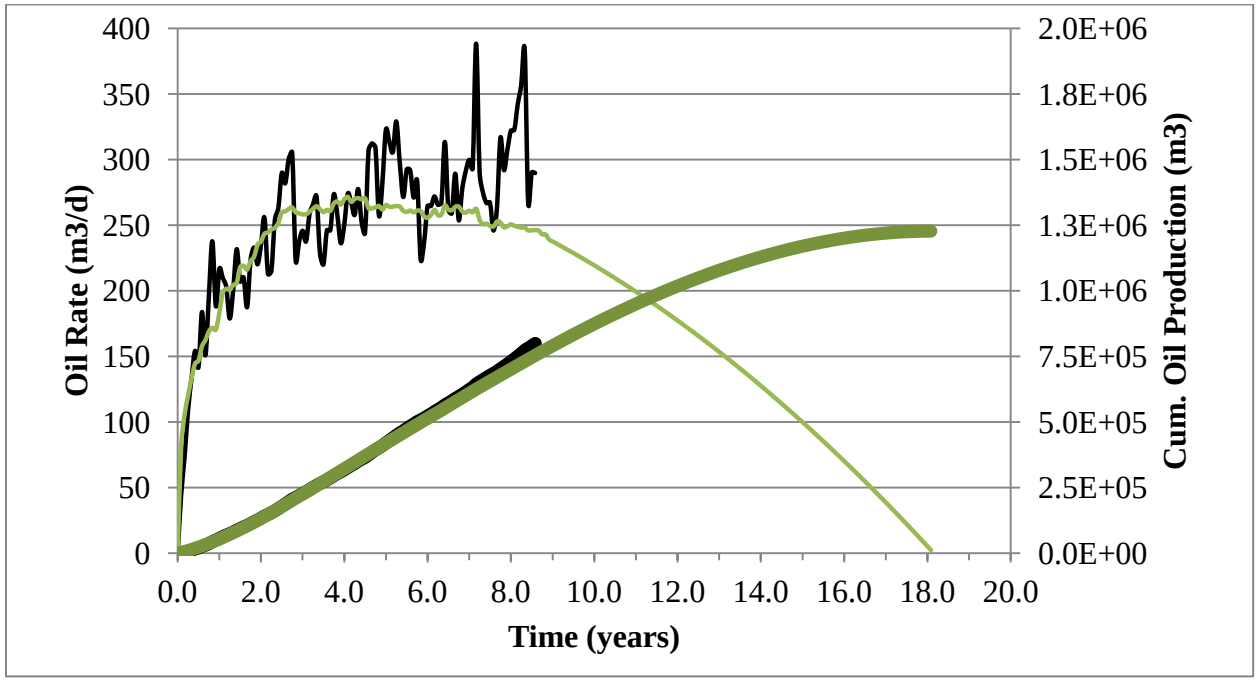

Figure 3.11.8: Comparison of historical production to oil drainage rate from analytical model for Firebag northeast macro level steam chamber.

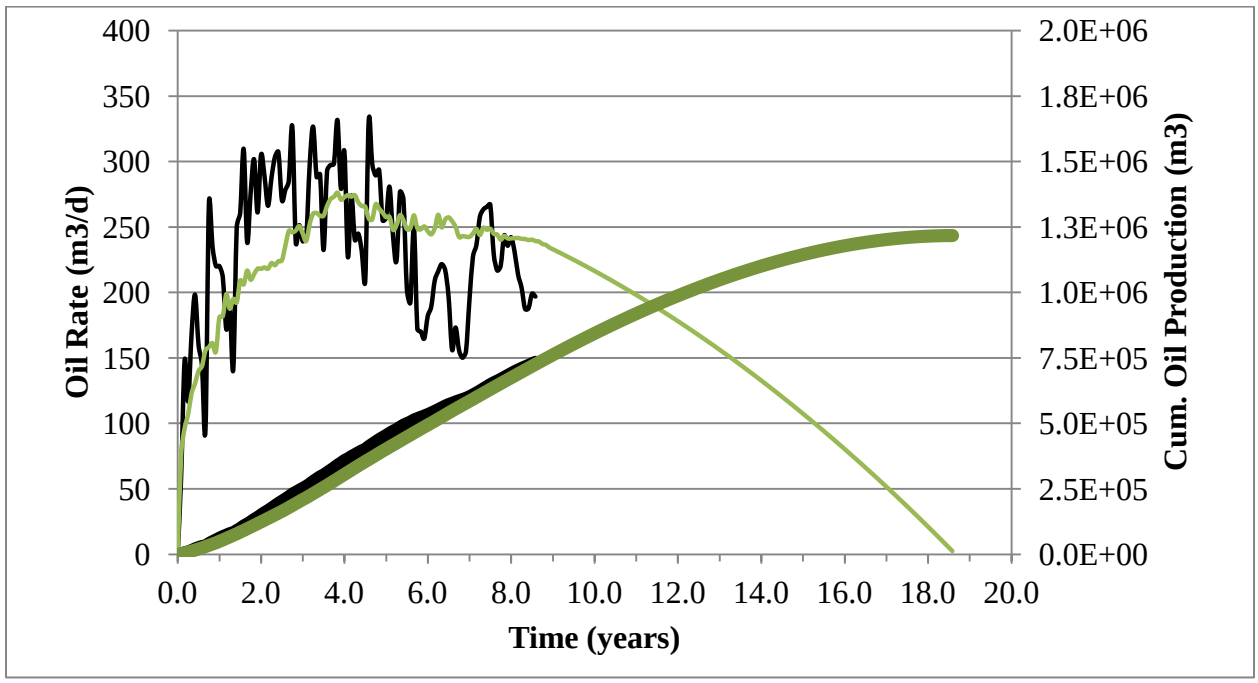

Figure 3.11.9: Comparison of historical production to oil drainage rate from analytical model for Firebag south macro level steam chamber.

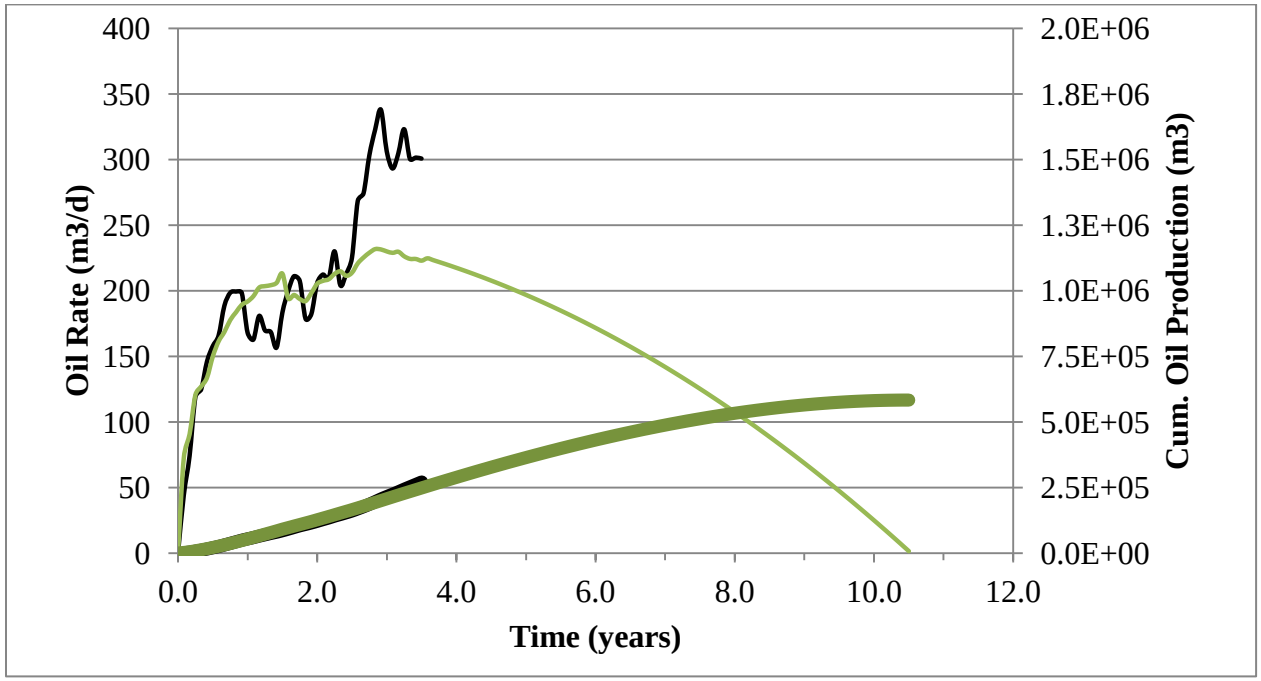

Figure 3.11.10: Comparison of historical production to oil drainage rate from analytical model for Firebag west macro level steam chamber.

CHAPTER 4: DEVELOPMENT OF ANALYTICAL MODEL FOR HEAT CONSUMPTION

An analytical model has been developed to model heat consumption and distribution for the Firebag SAGD operation. It is based on the same idea as the original model proposed by Reis (1992) in which total heat requirements for the SAGD process were quantified for three main sources of heat consumption:

- heat associated with expansion of the steam chamber,
- heat stored in the reservoir ahead of the steam zone, and
- heat lost to the overburden.

Reis' model was adapted by Edmunds and Peterson (2007) to use an analytical expression for the overburden heat loss from Carslaw et al. (1959), as well as an empirically derived factor to account for overburden heat losses to describe heat losses ahead of the steam zone.

Miura et al. (2010) built on the Edmunds and Peterson's work with several small revisions including:

- the expression from Cardwell et al. (1942) for time dependent residual oil saturation,
- a rising chamber phase from the expression derived by Butler (1998) for chamber height,
- a shape factor for a curved steam chamber,
- incorporation of subcool into the enthalpy calculations, and
- reduction in overburden heat losses after coalescence.

In this thesis, an analysis and comparison of the above calculation methods for quantifying heat consumption is performed. The final heat consumption model quantifies the heat consumption associated with the steam chamber expansion, the heat ahead of the steam zone, and the heat lost

to the overburden. The heat loss to the underburden and due to convective losses has also been grouped and quantified as a single heat consumption term.

In addition, several improvements were made to adapt the model for the Firebag property: the calculated thermal properties, fluid properties, reservoir properties, and values related to steam chamber geometry are specific to Firebag. 4D seismic has also been applied to determine steam chamber related data and to conceptually verify the heat consumption model that has been developed.

4.1 Permeability

Absolute permeability is a matched parameter that is the same value as that obtained from the oil drainage model described in Chapter 3. Also, as described in Chapter 3, relative permeability is expressed by a cubic function based on the viscosities of oil and water and the fractional flow of water given by the production water-to-oil ratio.

4.2 Residual Oil Saturation

Residual oil saturation values used in this model are the same as those used in the oil drainage model listed in Chapter 3 in which values were determined on a pad level using 4D seismic analysis.

4.3 Viscosity

Viscosity values used in this model are the same as those in the oil drainage model in Chapter 3. As mentioned in the previous chapter, dynamic viscosity is Firebag specific and in calculating the kinematic oil viscosity, the oil density has been corrected for temperature.

4.4 Heat Capacity and Thermal Conductivity

Values for heat capacity and thermal conductivity are the same as that used in the oil drainage model. Specific heat capacities for oil and water are calculated based on Equations 3.6.4 and 3.6.5 as presented in Chapter 3. The volumetric heat capacity of the reservoir and overburden are calculated from Equation 3.6.3. The thermal conductivity is calculated by using Equation 3.6.2.

4.5 Enthalpy Calculations and Steam Table Properties

High precision polynomial approximations are used to calculate steam enthalpies for the heat consumption model (Farouq Ali, 2010). The expressions for the latent heat of vaporization, L_V, sensible heat of liquid water at saturated conditions, H_w, and steam saturation temperature, T_S, corresponding to a given pressure are given by:

$$L_v = \sqrt{7184500+11048.6T-88.4050T^2+0.162561T^3-1.21377\times10^{-4}T^4} \qquad (4.5.1)$$

$$h_w = 23665.2-366.232T+2.26952T^2-0.00730365T^3+1.30241\times10^{-5}T^4-1.22103\times10^{-8}T^5+4.70878\times10^{-12}T^6 \qquad (4.5.2)$$

$$T_s = 280.034+14.0856(\ln P)+1.38075(\ln P)^2-0.101806(\ln P)^3+0.019017(\ln P)^4 \qquad (4.5.3)$$

The absolute residuals for the above polynomial approximations are less than 1% for $305 \leq T \leq 620$K and 0.611 kPa $\leq P \leq 22.12$ MPa (Farouq Ali, 2010).

Steam quality has also been incorporated into the model so that the heat injection can be more accurately calculated. A lower steam quality reduces the enthalpy injected into the reservoir. The enthalpy carried by the steam, H_{LV}, is reduced proportionally by the steam quality, f_{st}:

$$H_{Lv} = f_{st} L_v \qquad (4.5.4)$$

A steam trap (or subcool operation) has also been incorporated into the model. The implementation of this is done as a temperature difference between the injected steam and the produced fluids. Larger values of subcool mean that fluids are produced to the surface at lower temperatures than injection temperatures and that a higher proportion of the injected enthalpy is being left in the reservoir.

4.6 Volumetric Sweep Efficiency

In this model, the effective sweep efficiency of the reservoir is calculated from the withdrawal of oil from the reservoir. If the oil drainage rate and the individual saturations of oil and water within the reservoir are known, the reservoir volume (and therefore the steam chamber volume) can be determined. The volumetric sweep efficiency of a triangular shaped chamber will always be equal to 0.5 since a triangle occupies half of a rectangular cross sectional reservoir area. The plot displayed in Figure 4.6.2 shows the profile of the volumetric sweep efficiency, η, as a function of time. As can be seen, after the final match on historical oil rate and steam rate is obtained, the resultant sweep efficiency is approximately 40% initially and declines to approximately 30% before increasing almost linearly. A sweep efficiency of less than 50%

would suggest that the top of the steam chamber is wider at the top but skinnier in shape than a purely triangular shaped steam chamber as depicted in the simple diagram below.

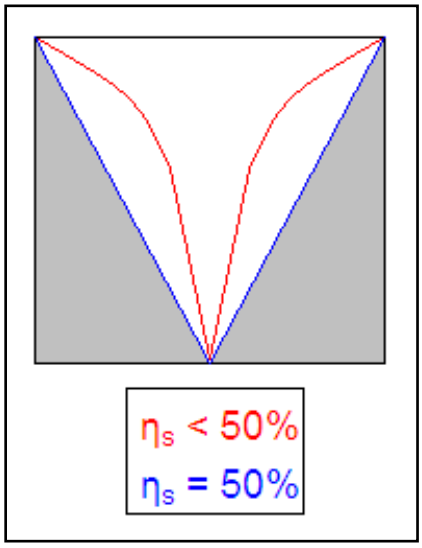

Figure 4.6.1: Volumetric sweep efficiency of various steam chamber shapes.

This is consistent with steam chamber shapes from Butler's TANDRAIN model. It is also consistent with the observations of laboratory SAGD experiments conducted by Javad et al. (2010) which shows skinnier steam chambers (see Figure 2.3.1) with fast vertical growth when there is some mobile water present in the reservoir which is suspected to be the case in the Firebag reservoir.

As time progresses, the volumetric sweep efficiency reaches 50% at which point significant coalescence is expected to have occurred between adjacent steam chambers. This is confirmed by and consistent with the time at which adjacent steam chambers interpreted from 4D seismic show significant coalescence as is evidenced in Figures 3.7.1, 3.7.2 and 4.7.1.

As the sweep efficiency exceeds 50%, the chambers are now growing downwards as opposed to laterally. A comparison with the chamber interface angle which is plotted with respect to time in the next section for Pad 101 validates the profile of the volumetric sweep efficiency. The interface angle starts at a steep angle (which is consistent with a skinny steam chamber) and over time flattens out to a shallower angle, approaching 30 degrees after approximately 10 years of life. Although only shown for Pad 101, this volumetric sweep efficiency profile has been generated and is similar for the other pads at Firebag.

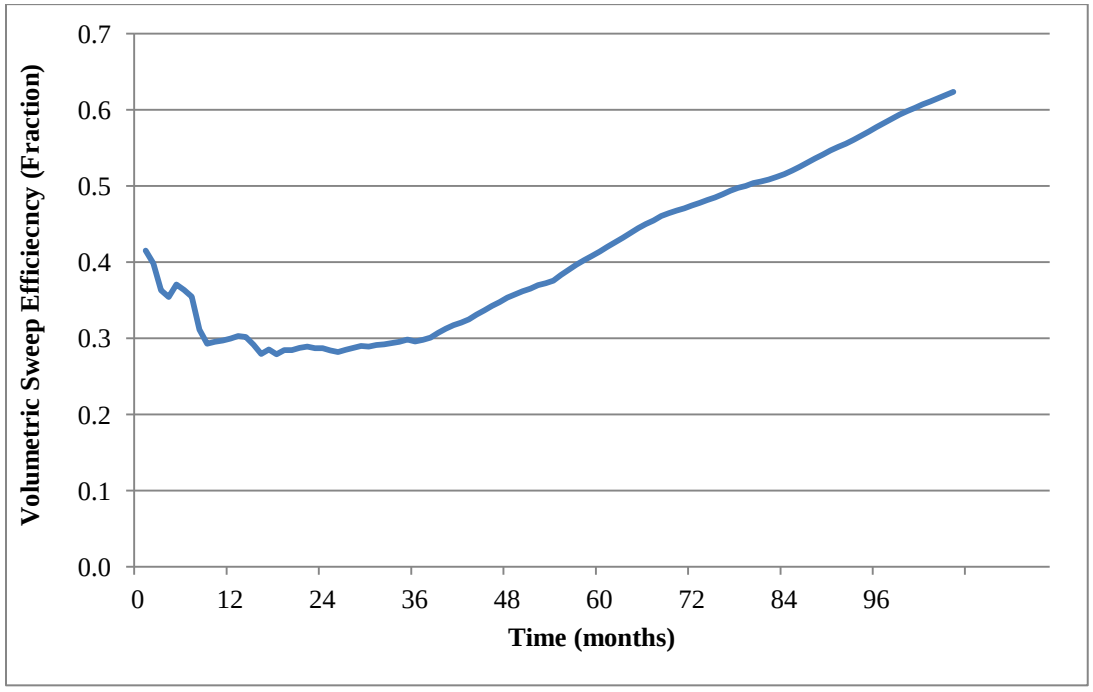

Figure 4.6.2: Reservoir volumetric sweep efficiency as a function of time for Firebag Pad 101.

4.7 Steam Chamber Velocity

An assumption used to derive the analytical expressions for heat consumption is that the velocity of the steam chamber front is constant with respect to time. However, time-lapse seismic has

shown that this is not likely the case at Firebag. Time-lapse seismic interpretation of the steam chamber has shown that there is a higher velocity at initial time which decreases as time progresses.

The application of time-lapse seismic to quantify SAGD steam chamber extent is not new, but as far as the author is aware, it has not yet been used to quantify steam chamber velocity. If the time between individual 3D seismic shots is regular enough, and the change in steam chamber area can be quantified, the velocity of the steam chamber front can be estimated with reasonable certainty.

Pads 104 and 107 are the only well pads at Firebag where all of wells on the pad have been started up at approximately the same time, and where there is consistent time-lapse seismic data since start-up. For Pad 104, seismic data has been available every year since the baseline seismic shot in 2009. Pad 107 has only been in operation since 2011 so only 1 year of time-lapse data is available.

The year over year increase in steam chamber area has been calculated on an individual well pair basis by Frank Sun, a geologist on the Firebag Asset Team at Suncor (Sun, 2012). Development of the steam chamber over time is shown in Figure 4.7.1 which is compiled from images from the Suncor ERCB Performance presentation (Suncor, 2011, 2012). It should be noted that the scales between the left and right images in Figure 4.7.1 are not the same (i.e. the colours in the left image do not represent the same chamber thicknesses as the same colours in the right image).

The intent is to show the qualitative change in chamber development between the two subsequent 3D seismic shots.

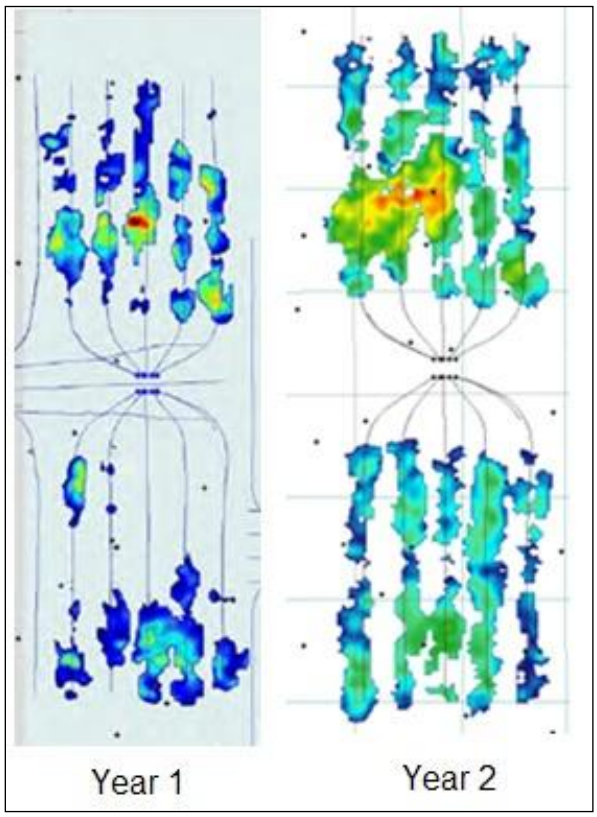

Figure 4.7.1: Suncor year over year 4D seismic interpretation of Pad 104 steam chambers (courtesy of Suncor, 2011, 2012).

By using geometry related assumptions that are consistent with the heat consumption model, that is, the steam chamber is approximately triangular in shape, and since the well length and increase in area are known, the average steam chamber velocity can be determined. The data plotted in Figure 4.7.2 reveal that the velocities of the steam chamber front of the individual well pairs for Pad 104 and 107 are of order of 4 to 13 cm/day. As can be seen there is a fairly large range of

chamber velocities from one well pair to the next on a particular pad which reflects the geological hetereogeneity in the reservoir.

A number of reservoir and operation related factors can affect the development of the steam chamber for any individual well. By averaging the velocities for an entire pad, the impact of these localized factors can be minimized. A relationship for average steam chamber velocity is shown for Pads 104 and 107 in Figures 4.7.3 and 4.7.4.

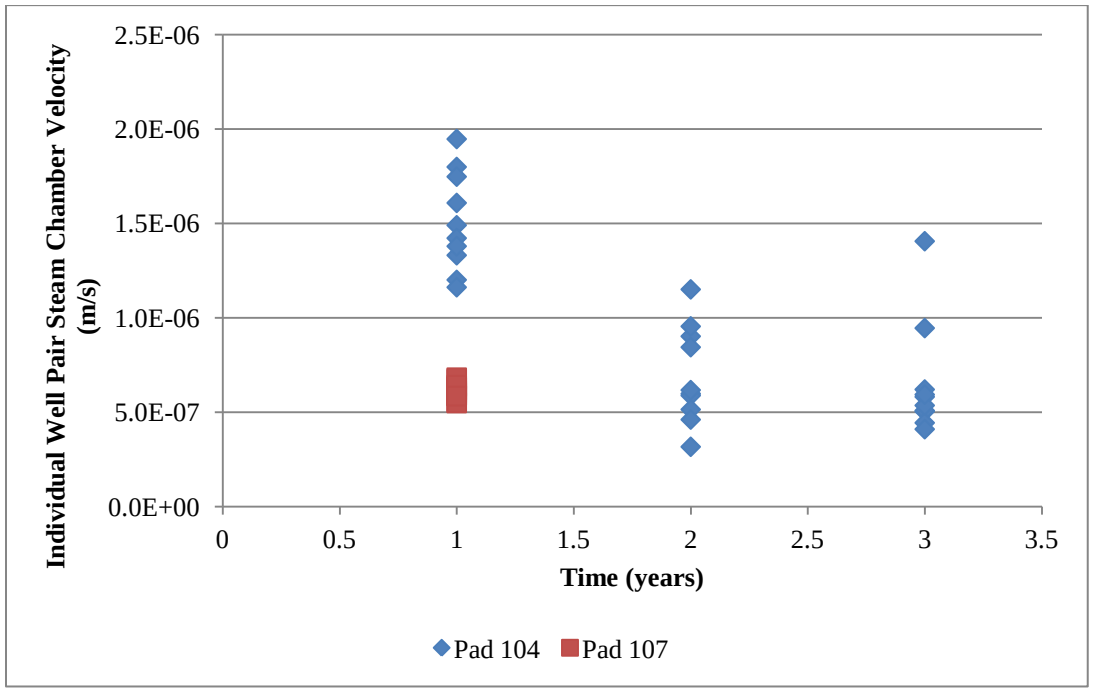

Figure 4.7.2: Steam chamber front velocity for individual well pairs on Pads 104 and 107.

Logarithmic and exponential regression analyses performed on the velocity data reveal reasonable correlations in both cases. The coefficient of determination (r-squared value) of the logarithmic regression case is higher than in the exponential regression case and suggests that the

steam chamber velocity should be a logarithmically declining function with time. A decreasing steam chamber velocity with time has been observed in practical field applications and has been incorporated into various analytical models (Pooladi-Darvish et al. 1995).

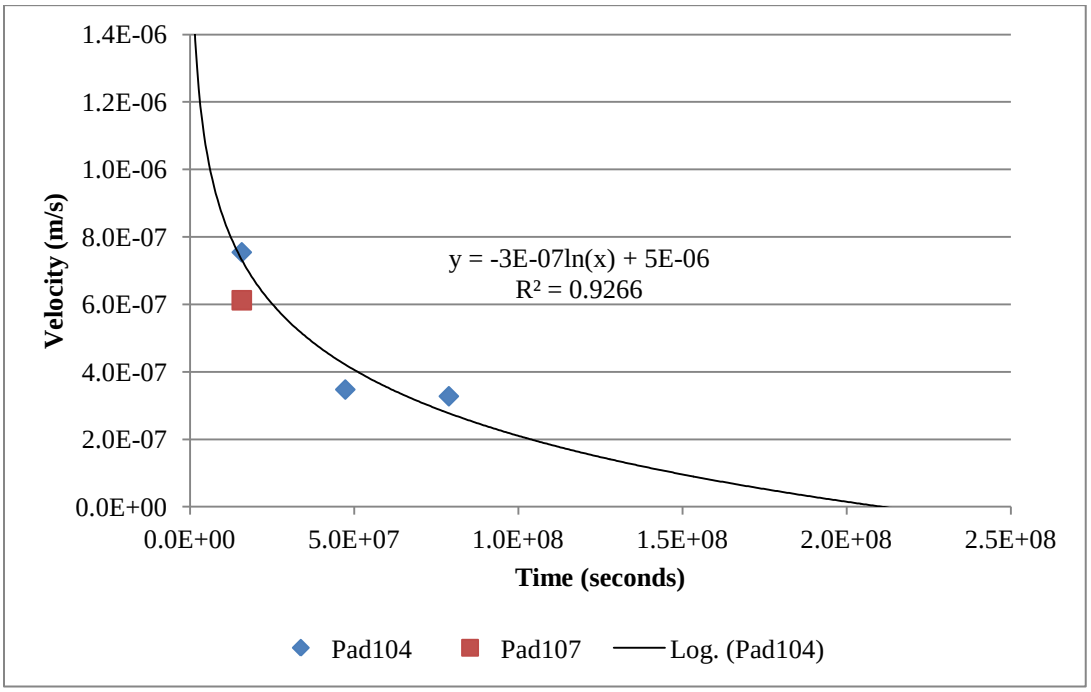

Figure 4.7.3: Average steam chamber velocity for Firebag Pads 104 and 107 including expression for logarithmic regression line of best fit. Note $5x10^7$ s ~ 572 days.

For the logarithmic relationship, the chamber front velocity decreases more rapidly such that at late time, the calculated overburden area (area under the curve) does not reach the full drainage area for the well pair. For the purposes of the current heat consumption model, the exponential relationship is applied even though it has a slightly lower coefficient of determination. As a first order approximation, it is still provides a reasonable fit for the velocity data. It is expected that as more data becomes available this assumption will be validated.

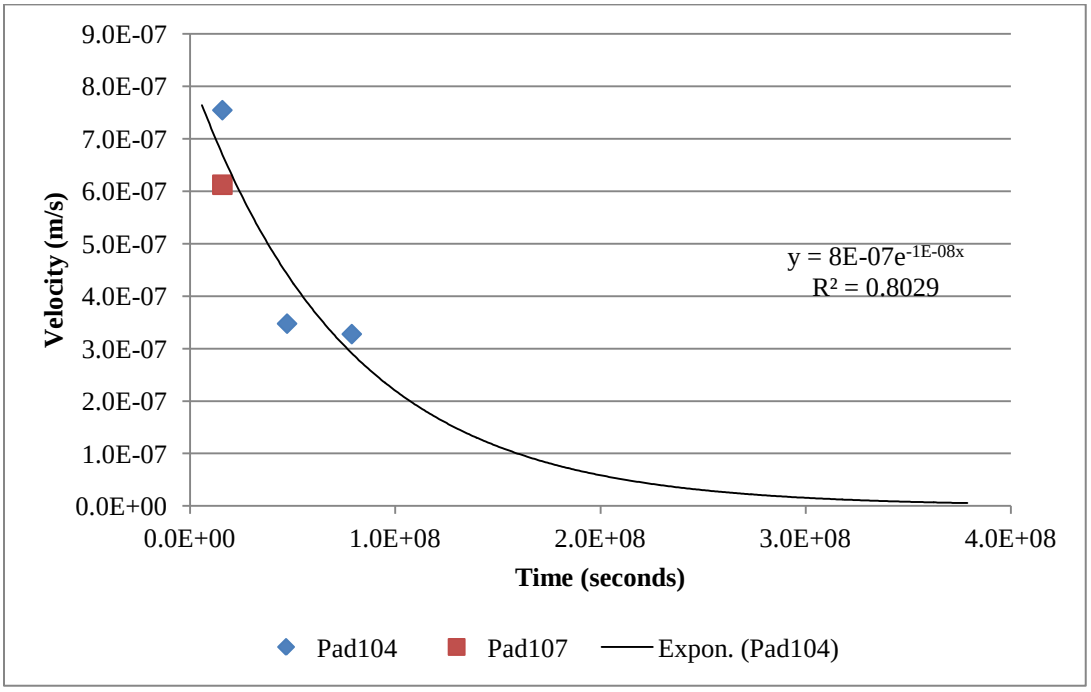

Figure 4.7.4: Average steam chamber velocity for Firebag Pads 104 and 107 including expression for exponential regression line of best fit. Note $1x10^8$ s ~ 1160 days.

A non-linear steam chamber front velocity with time impacts all of the individual components of the original heat consumption models proposed by Reis (1992) and Edmunds and Peterson (2007). Since overburden is exposed more quickly there will be higher overburden heat losses. The calculation for the heat stored ahead of the chamber front will also be impacted since the chamber geometry (velocity and steam chamber angle) is changing. Indirectly, it also affects the heat loss variable (described later in Section 4.11) used to describe the remaining heat losses since these are expressed as a fraction of the overburden heat losses.

The integration of the exponential function with respect to time is straightforward and yields an expression that is used to compute the total overburden area exposed as a function of time:

$$A_{ob}=2L\left[\frac{0.0000007822}{0.00000001245}\left(e^{-0.00000001245t}-1\right)\right] \quad (4.7.1)$$

The plot showing the overburden area exposed as a function of time is shown in Figure 4.7.5 for Firebag Pad 101. The results show that the overburden area asymptotically approaches the full drainage area, which is approximately 159,000 m^2 based on a well length of 993 m and a interwell spacing of 160 meters between adjacent well pairs. The profile of the exposed overburden area is only shown for Pad 101 but is similar for all pads at Firebag because the same exponentially declining expression is used to calculate the incrementally exposed overburden with time.

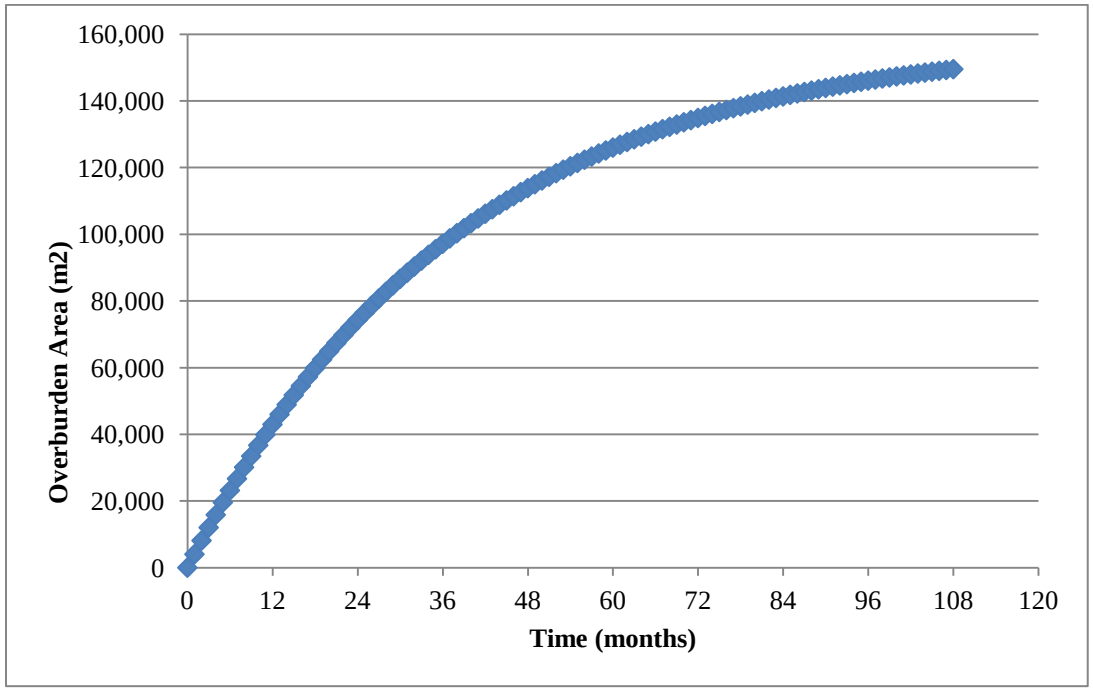

Figure 4.7.5: Exposed overburden area of Firebag Pad 101 as a function of time.

The interwell spacing between adjacent wellpairs on Pad 104 is equal to about 160 meters, whereas the equivalent spacing on Pad 107 is equal to about 90 meters. Although Pad 107 has

only been in operation for one year, there is only enough data to quantify the average velocity for the first year of chamber growth. The velocity of the steam chamber front for Pad 107 appears to be lower than that of Pad 104 by a factor of the well spacing between the two pads. The well spacing ratio of the two pads is equal to 0.56 (90 meters/160 meters) and the ratio of average velocity between the two pads is 0.58. From the match on oil and steam rates for Pad 107, which is the only well pad with significant production at 90 m spacing, it will be shown that this assumption appears to be valid. As more data becomes available for the pads recently on production at Firebag with 90 m well spacing (Pads 106, 108, 116) and 135 meter spacing (Pad 105), it can be determined whether this relationship is valid throughout the life of the wells.

4.8 Temperature

This analytical model calculates the cumulative energy requirements at a defined time before instantaneous values can be calculated from them. This method of calculation implies that variables in the equations do not change throughout the life of the project. However, some values such as steam temperature are a function of pressure and are usually time dependent because it is typical for reservoir pressures to vary as wells are operated. For instance, if the cumulative heat consumption is calculated based on a particular reservoir pressure and the reservoir pressure is later increased, the calculation method will assume that operation has been at the new pressure the entire time. Because of this, large swings in instantaneous steam consumption can occur and do not reflect expected behaviour.

To address this issue, an average steam temperature is used which is an arithmetic average of all previous historical reservoir pressures. The use of an average steam temperature has been

demonstrated by Edmunds and Peterson (2007) to reasonably match performance of CSS where there are alternating cycles of steam and production and reservoir temperatures are variable with time. This solution also addresses the unrealistic case where there is an instant change (either increase or decrease) in reservoir pressure which is not realistic given the volume of active steam chambers.

4.9 Heat Losses Ahead of the Steam Chamber Interface

The steam chamber boundary does not transition sharply from steam temperature to reservoir temperature; there is a temperature gradient that exists that begins at steam temperature within the chamber and decreases to the reservoir temperature at a certain distance outside the steam chamber.

Reis made the observation based on Butler's experimental work and on numerical simulation work that this temperature distribution ahead of the steam chamber interface was constant regardless of position or time. This means that it is also independent of velocity. Therefore the enthalpy ahead of the steam chamber interface proposed by Reis can be applied in this current model even though it is developed using an exponentially decreasing velocity.

Edmunds and Peterson did not quantify the heat stored ahead of the chamber interface. Instead they grouped it with underburden losses and assumed that it was approximately equal to one-third of the overburden heat loss. This was justified empirically by using field data. Miura et al. (2010) also used the same assumption that one-third of the overburden heat loss would be associated with heat stored ahead of the chamber interface. Butler states that the heat energy

stored ahead of the chamber interface is much higher than this and regardless of how it is determined (heat integral, experimental, etc.), it should be approximately equal to the heat losses to the overburden.

When Reis' Equation (2.1.36) is used to calculate heat stored ahead of the steam chamber interface in the current model and is compared to the overburden heat loss, it suggests that the heat ahead of the interface is much higher than one-third of the overburden heat loss as shown in Figure 4.9.1 for Pad 101. In early time, when the chamber interface angle is higher, the heat ahead of the chamber front is much higher (proportionally) when compared to the overburden heat loss. In later times, when the interface angle becomes smaller, it becomes a smaller portion of the total heat loss when compared to the overburden heat losses. The same plot for the other Firebag pads used in this analysis are not shown, but share the same profile as shown in Figure 4.9.1.

It should be noted that Equation 2.1.36 employed in this model to quantify heat ahead of the chamber interface is based on the assumption that the steady state same temperature distribution is applicable. In practice, there will be a transient phase in which ahead of the front builds up asymptotically to reach an equilibrium level before steady state heating can occur.

Butler also presented a method to estimate heat losses ahead of the steam chamber based on Fourier's law of heat conduction as follows:

$$\frac{Q_c}{A} = k_t \frac{T_s - T_R}{u} \qquad (4.9.1)$$

Equation 4.9.1 is given as a heat flux (heat per unit area). To determine the cumulative heat, the area is calculated based on the steam chamber geometry and interface angle. The reservoir thermal conductivity and steam chamber front velocity have both been determined as described earlier in Chapter 3. Since the temperature rise is also known, the heat loss can be calculated ahead of the steam chamber interface. A comparison of the heat ahead of the chamber interface is shown by using the methods presented by Butler and Reis for Firebag Pad 101, shown in Figure 4.9.2.

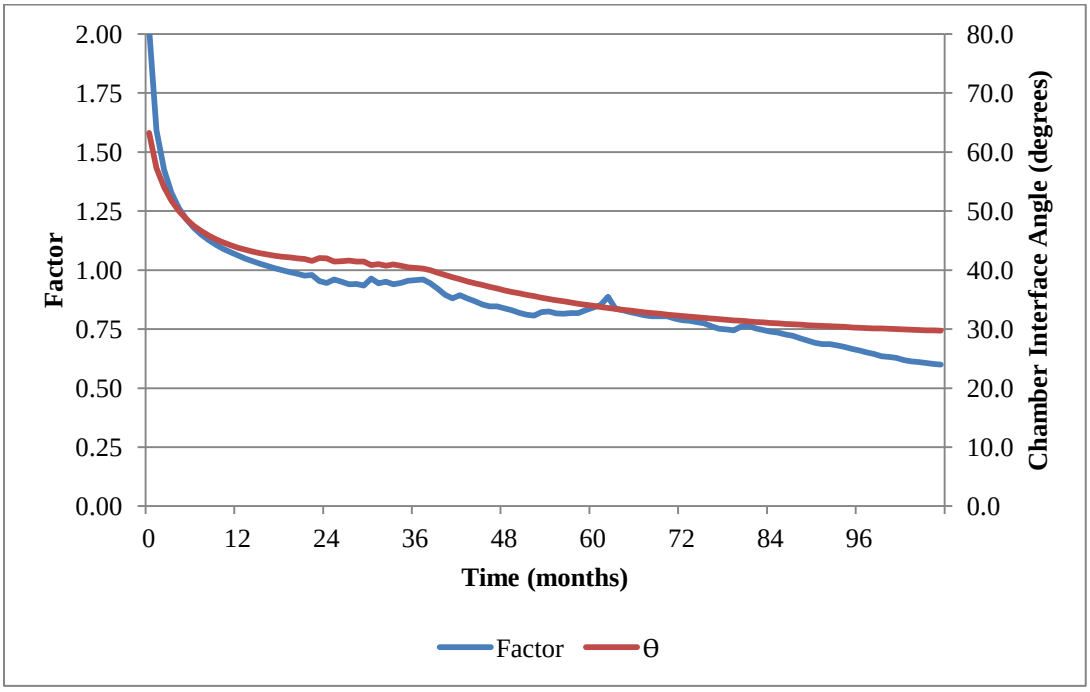

Figure 4.9.1: Enthalpy ahead of steam chamber interface as a factor of overburden heat loss as a function of time and steam chamber interface angle as a function of time for Firebag Pad 101.

The same graph has been generated for the other Firebag pads used in this analysis and although they are not shown, they all have similar profiles and similar trends between the cumulative heat calculated from the two different methods.

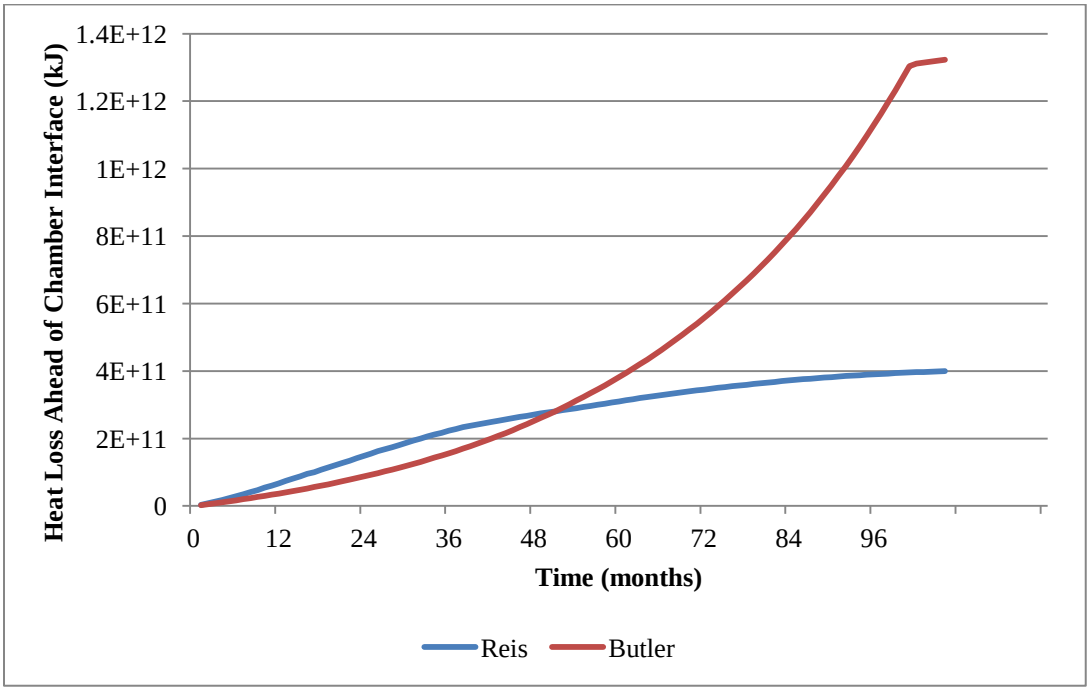

Figure 4.9.2: Comparison of cumulative heat stored ahead of chamber interface as a function of time for Firebag Pad 101.

Due to the exponentially decreasing steam chamber velocity shown at Firebag from time-lapse seismic, Equation 4.9.1 predicts very large amounts of heat ahead of the steam chamber interface in late time. In reality, low steam chamber velocities correspond to late time in the SAGD process when steam chamber coalescence occurs. After coalescence begins, the reservoir area that has an associated temperature gradient decreases and begins to disappear as the reservoir between adjacent steam chambers begins to reach the same temperature. This behavior following chamber coalescence is not captured in Figure 4.9.2 which explains why Equation 4.9.1 results in such high values of heat energy. If these high values are applied to the model to attempt to match Firebag historical performance it results in significant overpredictions of the steam-to-oil ratio, SOR.

Both models shown in Figure 4.9.2 are similar in prediction of heat loss ahead of the steam chamber interface up until approximately 60 months (which roughly corresponds to significant steam chamber coalescence based on current 4D seismic mapping). Although both equations are similar, the equation for the cumulative heat stored ahead of the chamber interface from the Reis model (Equation 2.1.29) appears to be valid over the entire well life and has been incorporated into the current Firebag heat consumption model.

4.10 Overburden Heat Losses

A comparison of heat losses to the overburden as per Reis' work and Edmunds and Peterson is shown in Figure 4.10.1. This reflects the different assumptions used in calculating overburden heat losses. While Miura et al. follows the work of Edmunds and Peterson, Reis approaches the problem differently and the overburden heat loss calculation derived by Reis appears to significantly overestimate the overburden heat losses for the Firebag property.

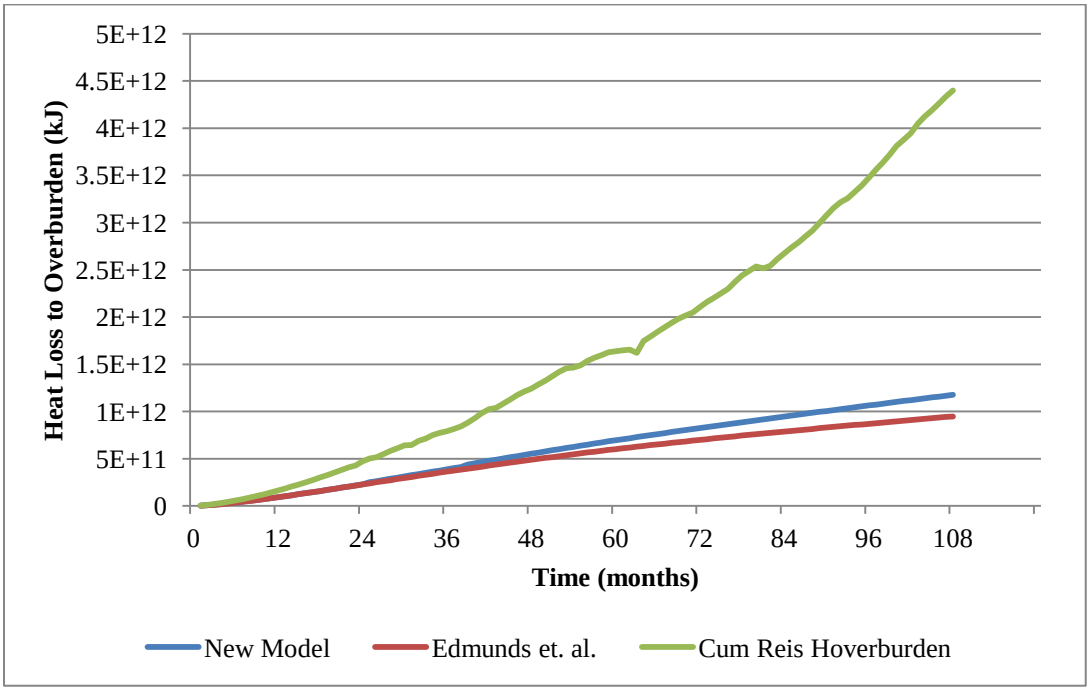

Figure 4.10.1: Comparison of various methods of overburden heat loss calculation as a function of time for Firebag Pad 101.

Steam chamber velocity is in the denominator of the cumulative heat loss expression presented by Reis (see Equation 2.1.36). This results in very high heat losses in late life of the SAGD well pair. The resultant units from Equation 2.1.36 are in kJ/($m^{0.5}$) and do not appear to be consistent with an actual heat value in kJ. Another variable is likely required in the equation to resolve the correct heat loss and may reduce the result of the calculation. In addition, the same reasons associated with chamber coalescence mentioned in the section above also apply. For these reasons the heat loss expression as per Reis is not expected to be realistic for the Firebag property.

The analytical expression for heat losses to the overburden originally derived by Edmunds and Peterson is based on the solution for heat loss to a semi-infinite plane as per Carslaw et al.

(1959). It takes into account the overburden area exposed at any given time, meaning that areas exposed to steam earlier in the well life will have had more time to lose heat while areas exposed to steam later in the well life will not have had as much time to lose heat.

This is done by introducing a variable, *a*, in Equation 2.1.37 which represents the fraction of total heated area at any given time and a variable, λ, which is the time at which the area represented by *a* is exposed. An assumption is made that there is a constant increase in incremental exposed area with time makes it straightforward to evaluate the integral in Equation 2.1.38. The result is a simply a scalar multiple of two-third applied to Equation 2.1.37 by Carslaw et al. (1959). The significance of this factor is that although the steam chamber grows until entire overburden area becomes exposed, only an effective area of two-third is contacted by steam up until the time of coalescence since different areas of the overburden were exposed at different times.

It is mentioned by Edmunds and Peterson that after coalescence of adjacent steam chambers occurs, this factor of two-third will begin increase since the effective area is now the full drainage area. In late time, it would be expected that the cumulative heat loss to the overburden would be similar to a situation where the full drainage area was exposed to steam from the onset of SAGD and the factor would approach a value of 1.

When Miura et al. (2010) adapted the Edmunds and Peterson's model, the assumption of the two-third factor was also applied throughout the life of the well which has been shown to underestimate heat losses after steam chamber coalescence occurs. In addition, geometry was also used to derive a correction factor to reduce the overburden heat losses after coalescence.

This correction was supposed to address the additional overburden exposed to heat after coalescence of steam chambers. However this is not consistent with Equation 2.1.37 used to model the overburden heat loss in which the overburden area is already explicitly defined and would not continue to increase after coalescence. Both of the above reasons will result in an underestimation of heat loss to the overburden.

Although it is similar, the current model for Firebag heat consumption differs from the model proposed by Edmunds and Peterson, Equation 2.1.40, which calculates heat loss based on a constant areal expansion or in other words a constant velocity steam front. The current model assumes the incremental area exposed is not constant with time since the steam front velocity is an exponentially declining function. The integral is given by:

$$H_o=2A\Delta T\sqrt{\frac{k_t C_{vo}}{\pi}}\int_0^1\sqrt{t-e^{ca}}da \qquad (4.10.1)$$

which can be evaluated analytically by using a substitution and partial fraction decomposition, however for convenience of implementation in the model it is evaluated by using a numerical approach in Microsoft Excel™. At any given time, the variable, *c*, in the equation changes because the exponential function that describes the exposed area as a function of time also changes. The resultant effective area is not a constant 2/3, instead it is variable, starting at approximately 2/3 and increasing with time. Thus the current model is valid even after the coalescence of steam chambers.

Figure 4.10.1 shows how the overburden heat loss changes when an exponentially decreasing steam chamber velocity derived for Firebag is compared to the constant steam chamber velocity

assumed by Edmunds and Peterson. Figure 4.10.1 is shown for Pad 101, however the trends between the various methods of calculation of cumulative heat loss are similar to the other Firebag pads used in this analysis.

The original model by Edmunds and Peterson assumes the steam chamber occupies the entire height of the reservoir from the start of SAGD. Therefore it is valid to use the volumetric heat capacity of the overburden to calculate the overburden heat losses from the start of SAGD. The model by Miura et al. (2010) considers a rising chamber phase where the steam chamber height begins at zero (the base of the reservoir). However it does not appear that a distinction is made between overburden and reservoir volumetric heat capacity during this phase and only a single overburden volumetric heat capacity is assumed to have been used.

During the rising chamber phase, the ceiling of the steam chamber is part of the reservoir. It is not until the steam chamber reaches the top of the reservoir that the ceiling of the steam chamber is overburden. Heating the ceiling of the steam chamber when it is still within the reservoir is technically not considered a heat loss since the heat is being used to mobilize bitumen, however it is calculated as part of the overburden heat losses for the purposes of this study. In that regard, it can be seen as a pseudo heat loss.

The volumetric heat capacity of the overburden is higher than that of the reservoir, and this is taken into account in the heat calculation in the current model. During the chamber phase, the volumetric heat capacity of the reservoir is used in the pseudo heat loss calculation. Once the

chamber has reached the top of the reservoir, the volumetric heat capacity of the overburden is used in the heat loss calculation.

Due to reservoir heterogeneities (such as the distribution of muds, shales, and inclined heterolithic strata within the reservoir), undulating depositional surfaces, and non-uniform steam distribution along the length of the horizontal wellpair, it is unlikely that the top of the reservoir is a flat surface; it is also unlikely that the entire chamber will reach the ceiling in a step-wise fashion. In reality, the conformance of the steam chamber above the vertical well will not be perfect and the overburden will likely be exposed gradually. As seen in Figure 4.10.2, the assumptions of a step-change exposure to the overburden results in a sudden increase in the cumulative heat consumption which reflect the sudden change in volumetric heat capacity. Since the instantaneous heat consumption is back calculated from the cumulative heat consumption, there is a large spike in heat consumption. This is merely an artifact of the calculating an instantaneous rate from a cumulative value and does not have any physical significance in practical applications.

If the expression for cumulative heat consumption used in this model is differentiated with respect to time, this calculation artifact can be eliminated. Since the constant (which can be defined as c) representing the effective area has already been calculated from the previous integration shown in equation 4.10.1, the new equation representing instantaneous heat loss to the overburden is shown below:

$$0.5cA\Delta T\sqrt{\frac{k_t C_{vo}}{\pi t}} \qquad (4.10.2)$$

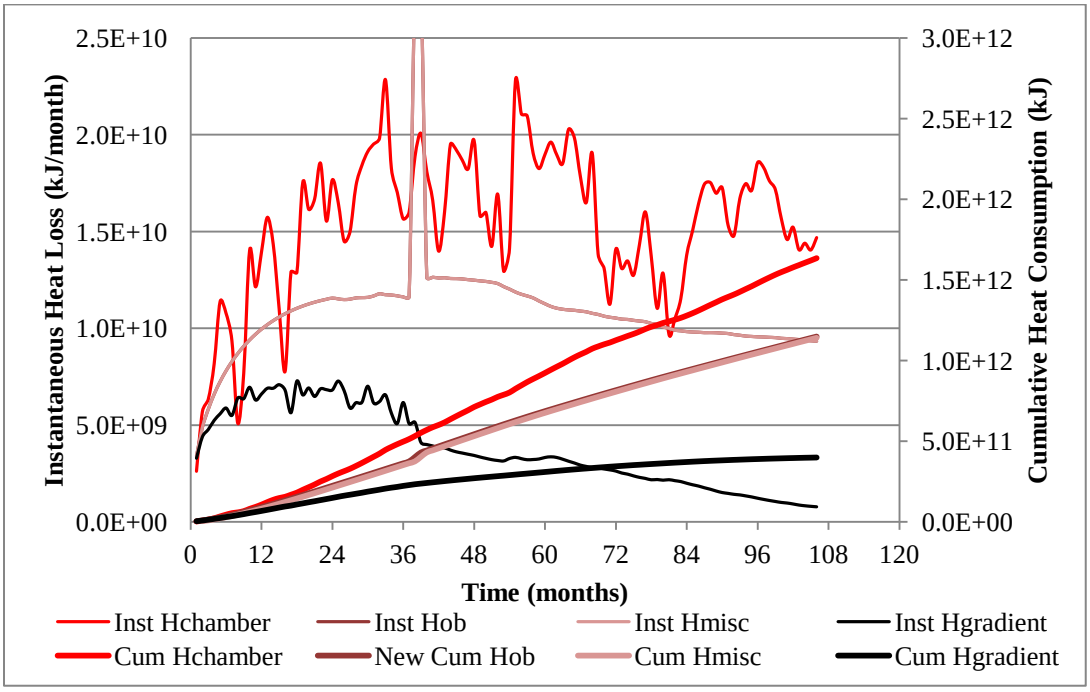

Figure 4.10.2: Comparison of various sources of instantaneous and cumulative heat consumption in the reservoir for Firebag Pad 101.

4.11 Heat Loss Factor

When the approaches by Edmunds and Peterson (2007) and Miura et al. (2010) are applied and compared to actual SAGD field performance at the Firebag property, it becomes apparent that they all underestimate the steam requirements and therefore the steam-to-oil ratios. In addition to the heat losses to overburden, heat consumption within the chamber and ahead of the steam chamber interface, there appear to be additional heat losses associated with production from the Firebag well patterns.

One plausible contribution to additional heat losses at Firebag may be the presence of intraformational mobile water. There are many portions of the reservoir at Firebag that are not at residual water saturation. Experiments conducted by Javad et al. examined the impact of initial

water saturation on thermal efficiency of SAGD and it was found that higher initial water saturations resulted in adverse steam-to-oil ratios. Evidence of this can be seen at outcrops and mine faces as shown in the Suncor Steepbank mine photograph in Figure 4.11.1, where water is seen in both the pay and non pay facies. This mobile water may have an impact at both initial reservoir temperature and at elevated reservoir temperatures.

This introduces another issue related to the heterogeneity of reservoirs that has not been considered in previous models; within the pay zone, there exist non-pay facies (mud and shale) that will impact production and thermal efficiency of SAGD. Using a net pay thickness to calculate the reservoir volume will result in a smaller reservoir volume to be heated since the non pay facies will not be included in this net pay thickness. In this model the net pay thickness is used, however an alternative to this would be to use the gross thickness with an average volumetric heat capacity.

Another contribution is related to the fact that the overburden heat loss and the heat associated with the temperature gradient ahead of the steam chamber interface only consider steady state conductive heat transfer. These portions of the reservoir are not at residual water saturation and not void of mobile water so there will likely be some impact due to convective heat transfer as well. Sharma and Gates (2011) has shown that the heat transfer from steam condensate convection effects ahead of the front is significant.

Figure 4.11.1: Photo of formation water at Steepbank mineface (courtesy of Suncor, 2012).

A third contribution relates to the underburden. Wells cannot be placed directly against the base of the reservoir due to undulation in the underlying structure. There is usually a significant amount of pay that is left below the producers. Although Reis made the assumption that losses to the underburden would be negligible due to the geometry of the steam chamber, in reality there will likely be both conductive and convective heat losses to the underburden.

Lastly, the model developed here assumes that the full drainage area is the well spacing multiplied by well length. In real life applications, there is steam chamber growth beyond the toes and heels of the wells and this is validated with 4D seismic (seefigures 3.7.1, 3.7.2, and

4.7.1). This steam chamber growth has been demonstrated to be significant, especially with the progression of time.

A heat loss factor is used to capture additional heat losses that are a result of all of the above reasons. This heat loss factor is used as a matching factor that is required to match Firebag field history in both early and late time. A convenient way to define this heat loss factor is as a factor of the overburden heat losses which is consistent with how it has been treated in literature. To reliably match historical Firebag performance, it is found that this factor is approximately equivalent to the overburden heat loss for Pads 101, 102, 103, and 104. For Pad 107 a smaller factor of 0.75 was applied to obtain a match; this is likely due to the fact that Pad 107 has narrower spacing between adjacent well pairs (90 meters versus 160 meters). The profile of this heat loss factor appears to be time independent and can be seen in plot in the previous section.

4.12 Results

The appropriate input parameters for Firebag pads 101, 102, 103, 104, and 107 as described above were input into the heat consumption model and resultant profiles were generated for the steam injection. Similar to the oil drainage model results described in Chapter 3, each pad and macro chamber prediction in the steam consumption model is based on the properties for an average equal weighted well pair on the respective pad or macro chamber. The groupings for the macro steam chamber level are described Section 3.7.

The steam injection values from the model were compared to historical steam injection values and a satisfactory match was obtained on both an instantaneous and cumulative basis. In

addition, instantaneous and cumulative steam oil ratios were also generated from the steam consumption model and compared to historical data. Again, satisfactory matches were obtained. The historical values (instantaneous and cumulative) for steam and steam oil ratio have been normalized to first production date for each pad in the same way it was done for the historical oil production values.

The same comments made in the oil drainage model results in Chapter 3 related to operational issues apply to the heat consumption model as well. The noise that can be associated with operation of the wells is not matched by the instantaneous values generated by the model but the general trends are. The cumulative values are more telling in terms of the closeness of the match; the values predicted by the model are very close to the historical values.

Due to the lack of pressure history in the early life of the Firebag property, exact values are unknown. Those values that have been used are simply extrapolations from the earliest pressure data. For this reason, less emphasis should be placed on the match in the oil rate in early time. This only impacts the first two years of Pads 101 and 102.

As can be seen in Figures 4.12.1 to 4.12.24, closer matches are obtained for steam-to-oil ratio on the macro steam chamber level than at the pad level. This suggests that there is likely movement of fluids between pads and this is captured when modeling it on a larger scale.

The model prediction is a close match to actual field performance over the entire duration of SAGD operation. It matches on both a pad level and a larger macro chamber level. This provides

confidence that the model is sufficiently capturing the heat transfer and fluid flow physics that govern the SAGD process. The ability to accurately forecast the thermal efficiency of the SAGD process has large implications for facility design, the budgeting of steam for future pads, and determining the steam costs which aids in the economic analysis decision making process.

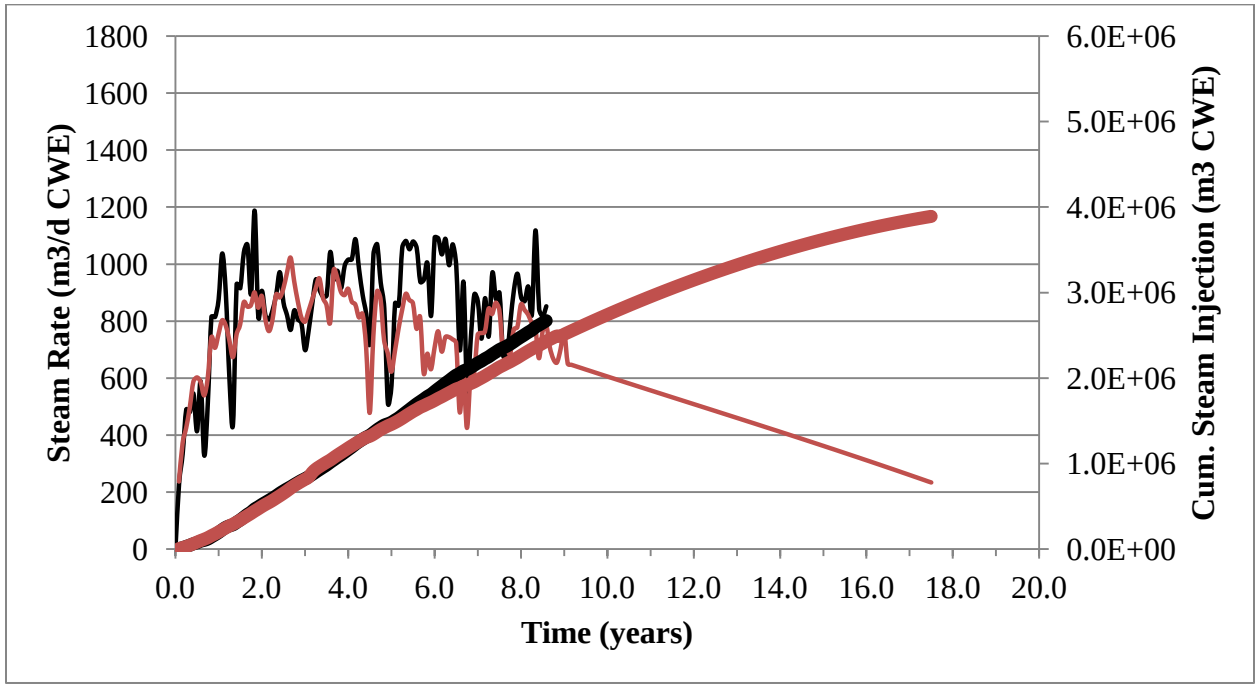

Figure 4.12.1: Comparison of instantaneous and cumulative steam injection model output with historical values for Firebag Pad 101.

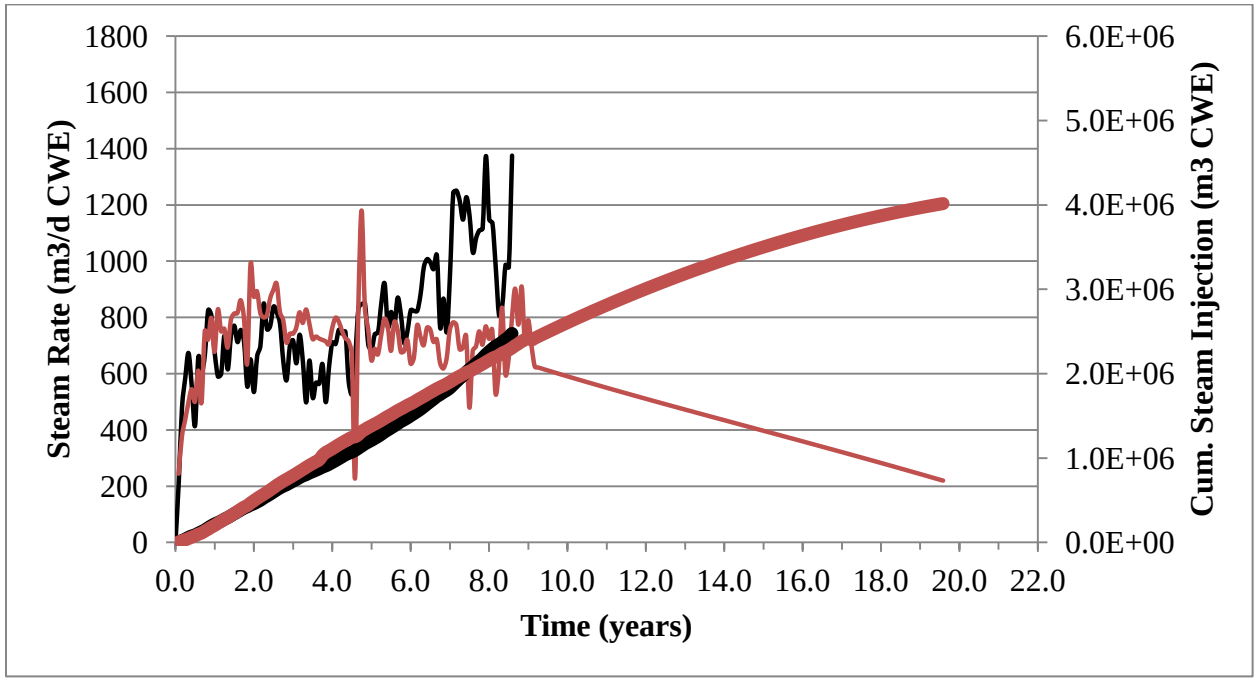

Figure 4.12.2: Comparison of instantaneous and cumulative steam injection model output with historical values for Firebag Pad 102.

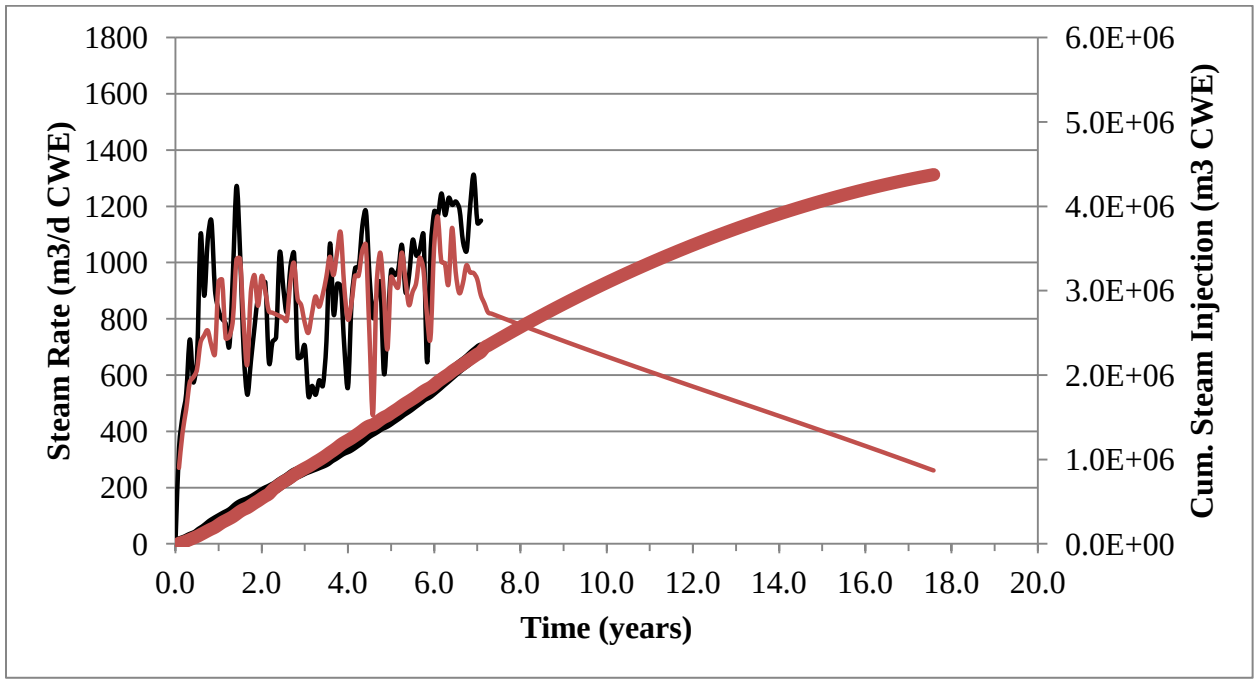

Figure 4.12.3: Comparison of instantaneous and cumulative steam injection model output with historical values for Firebag Pad 103.

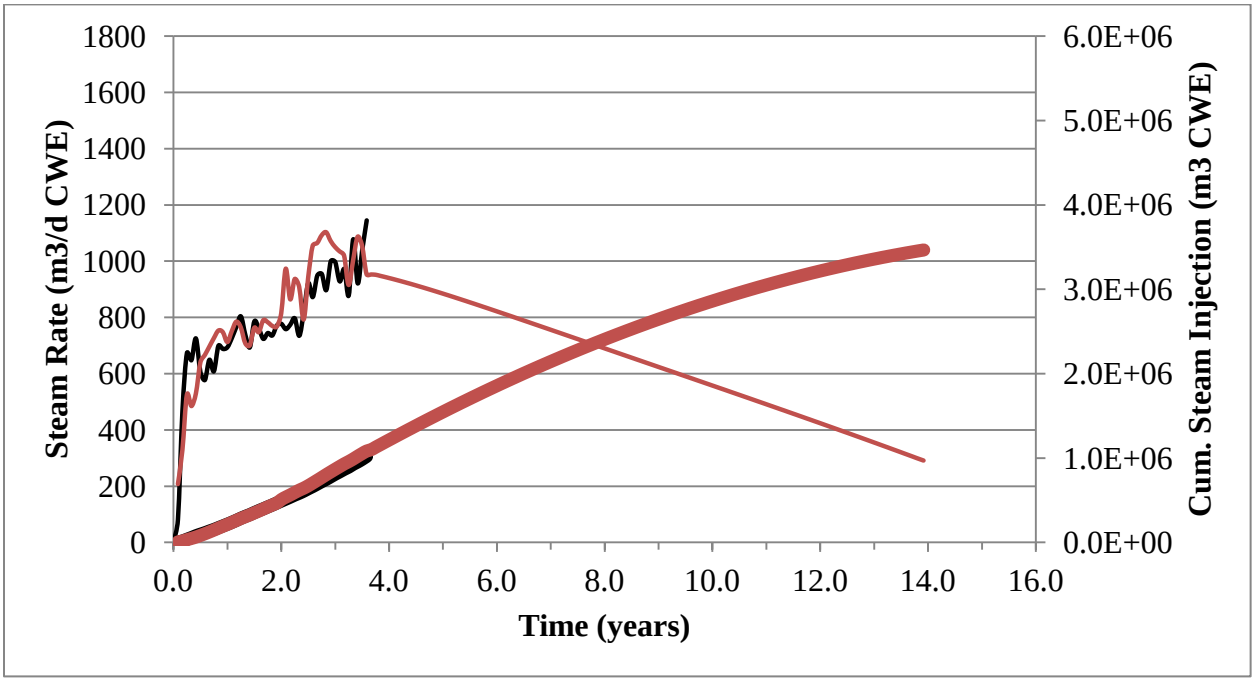

Figure 4.12.4: Comparison of instantaneous and cumulative steam injection model output with historical values for Firebag Pad 104.

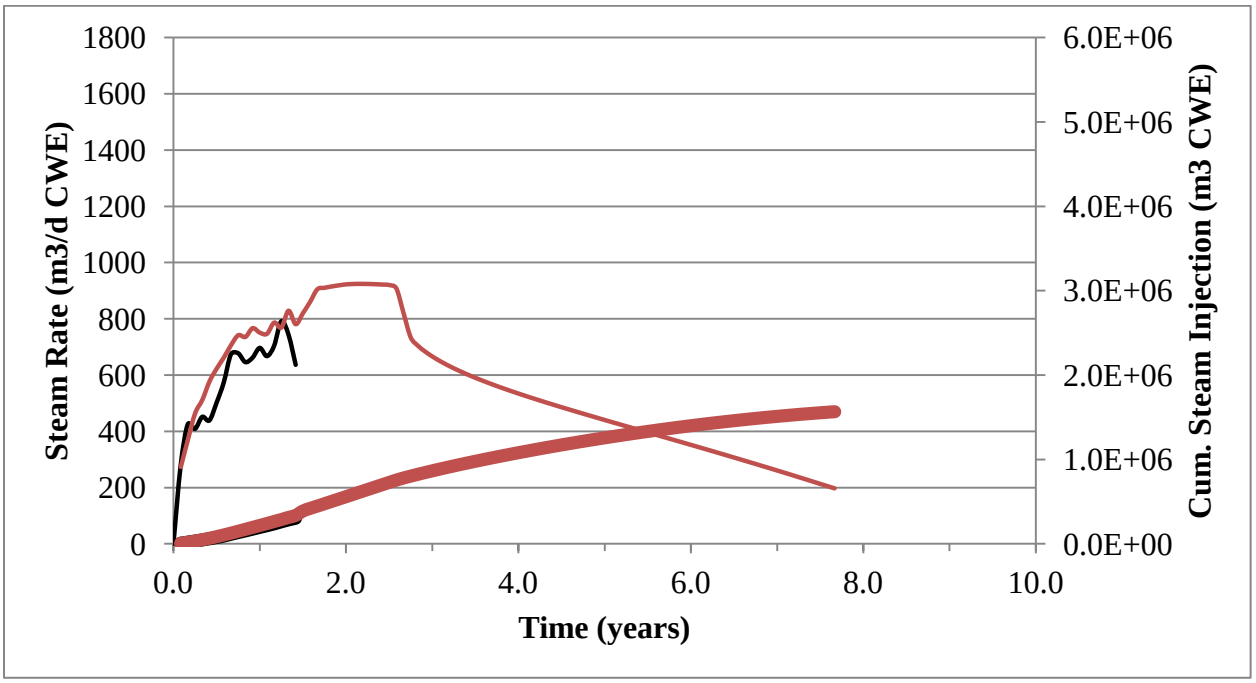

Figure 4.12.5: Comparison of instantaneous and cumulative steam injection model output with historical values for Firebag Pad 107.

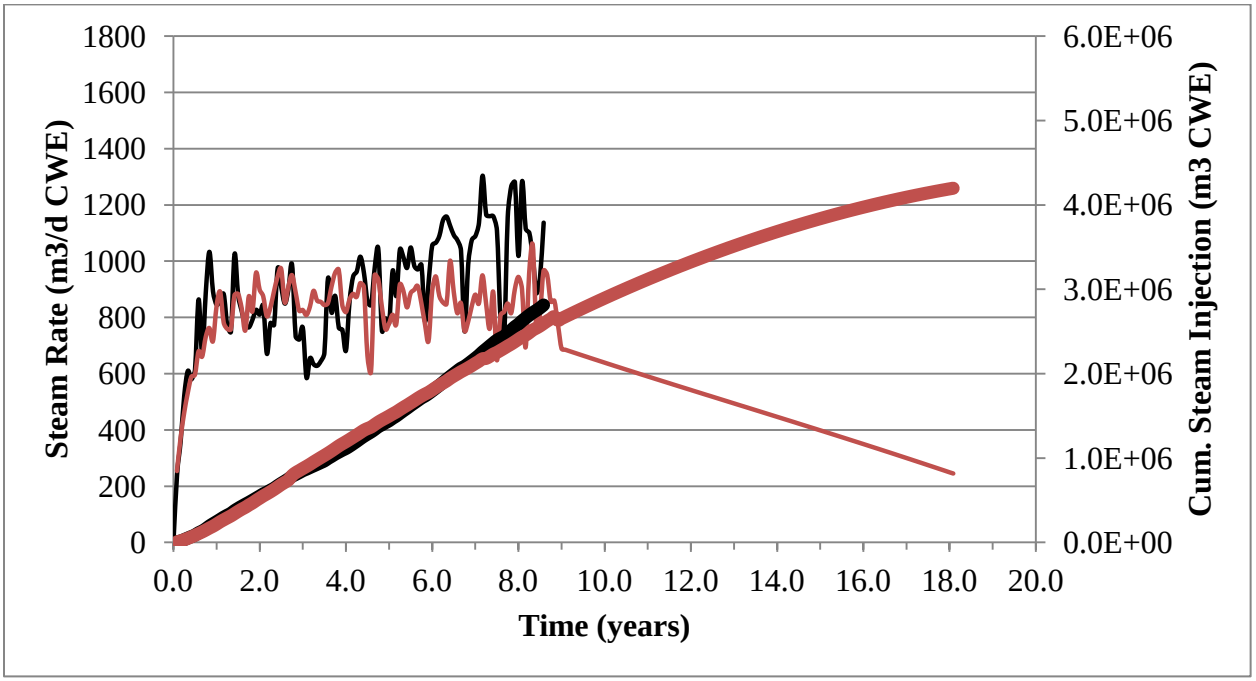

Figure 4.12.6: Comparison of instantaneous and cumulative steam injection model output with historical values for Firebag northeast macro level steam chamber.

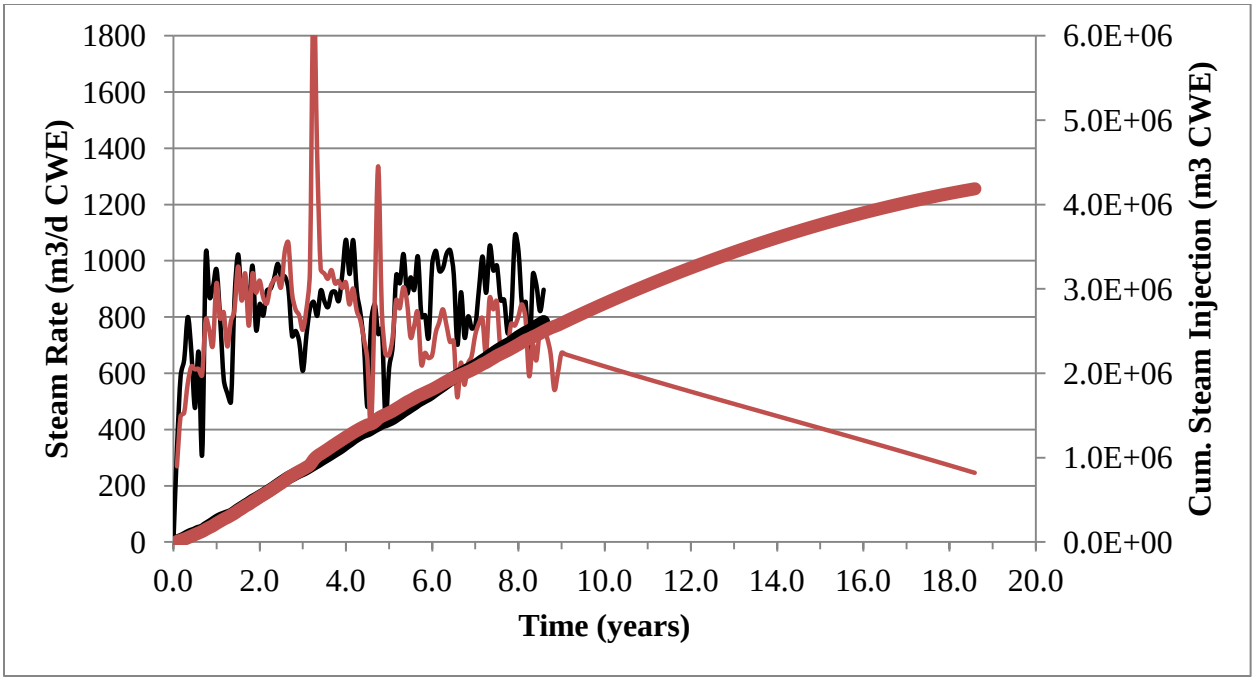

Figure 4.12.7: Comparison of instantaneous and cumulative steam injection model output with historical values for Firebag south macro level steam chamber.

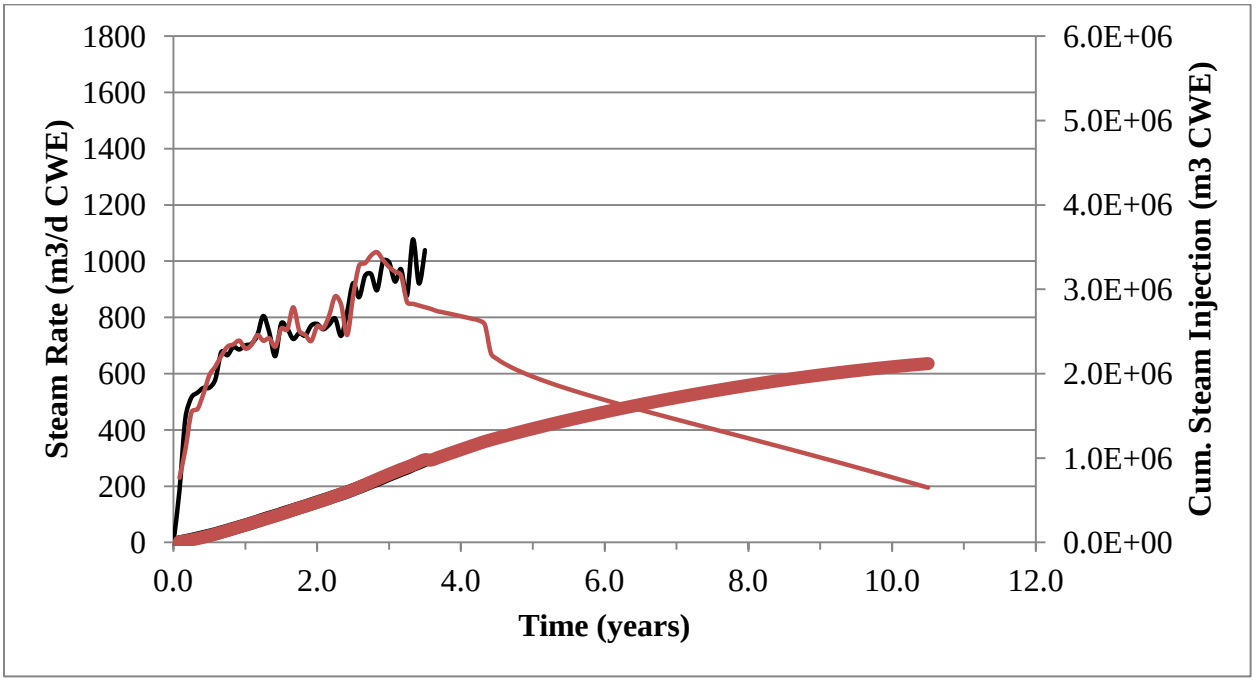

Figure 4.12.8: Comparison of instantaneous and cumulative steam injection model output with historical values for Firebag west macro level steam chamber.

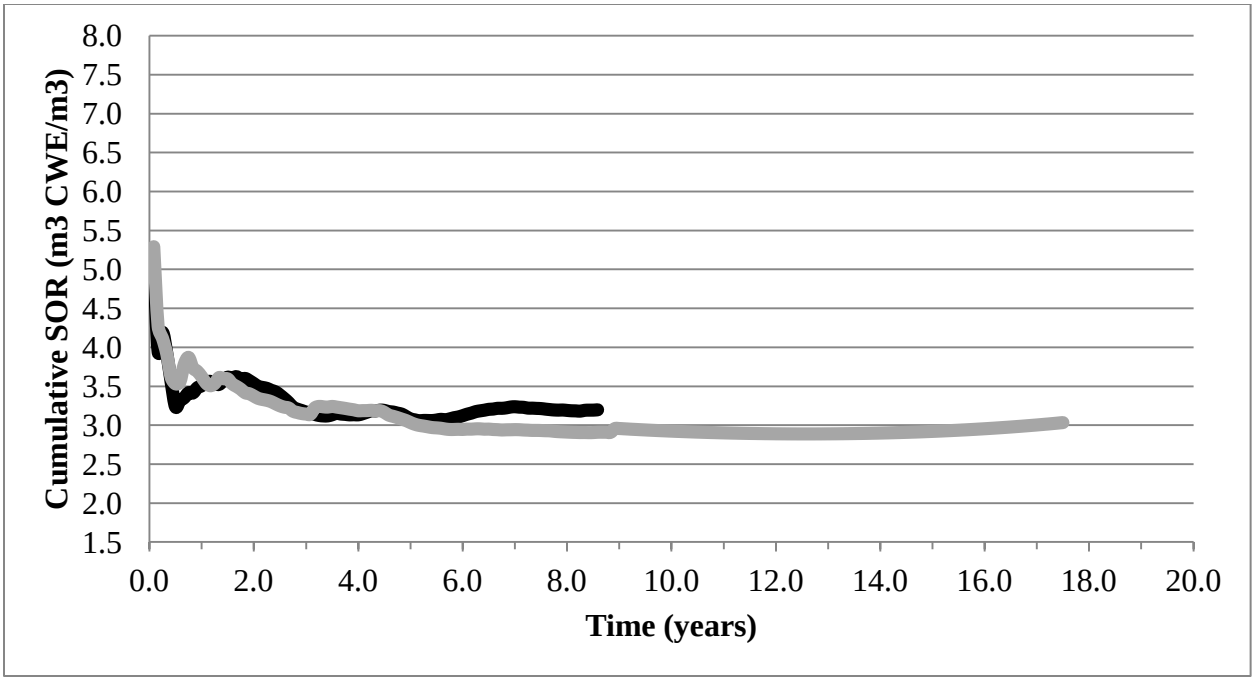

Figure 4.12.9: Comparison of cumulative steam oil ratio from steam injection model with historical values for Firebag Pad 101.

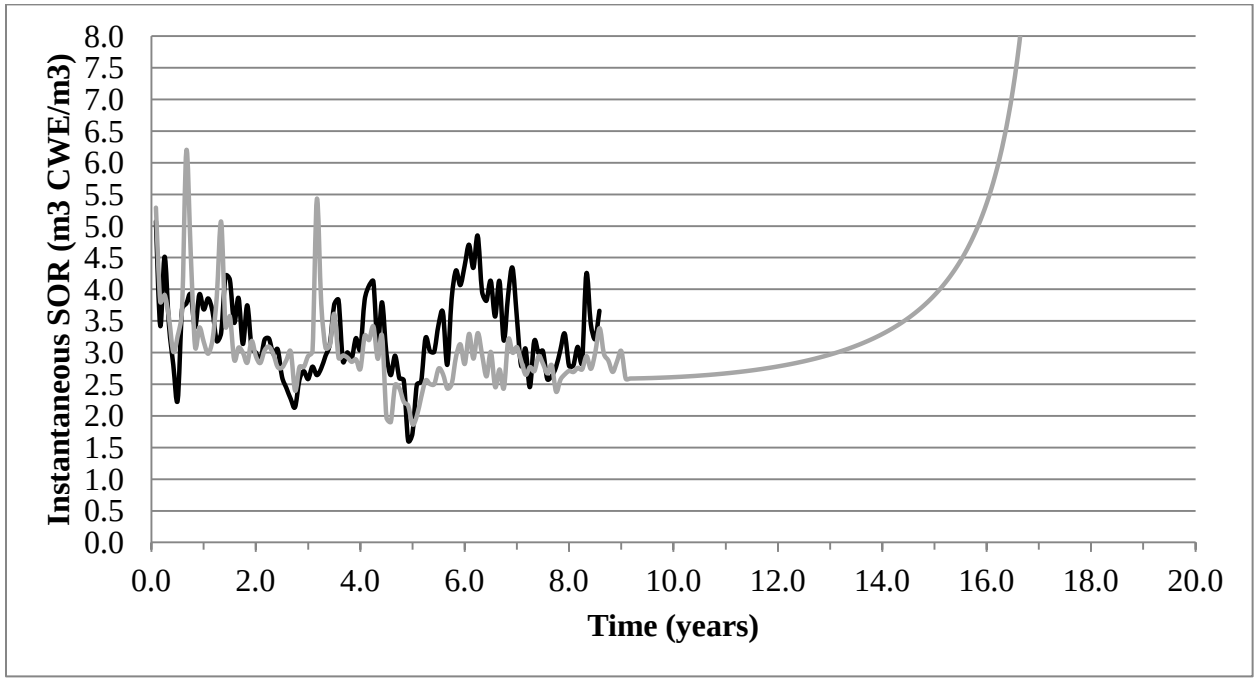

Figure 4.12.10: Comparison of instantaneous steam oil ratio from steam injection model with historical values for Firebag Pad 101.

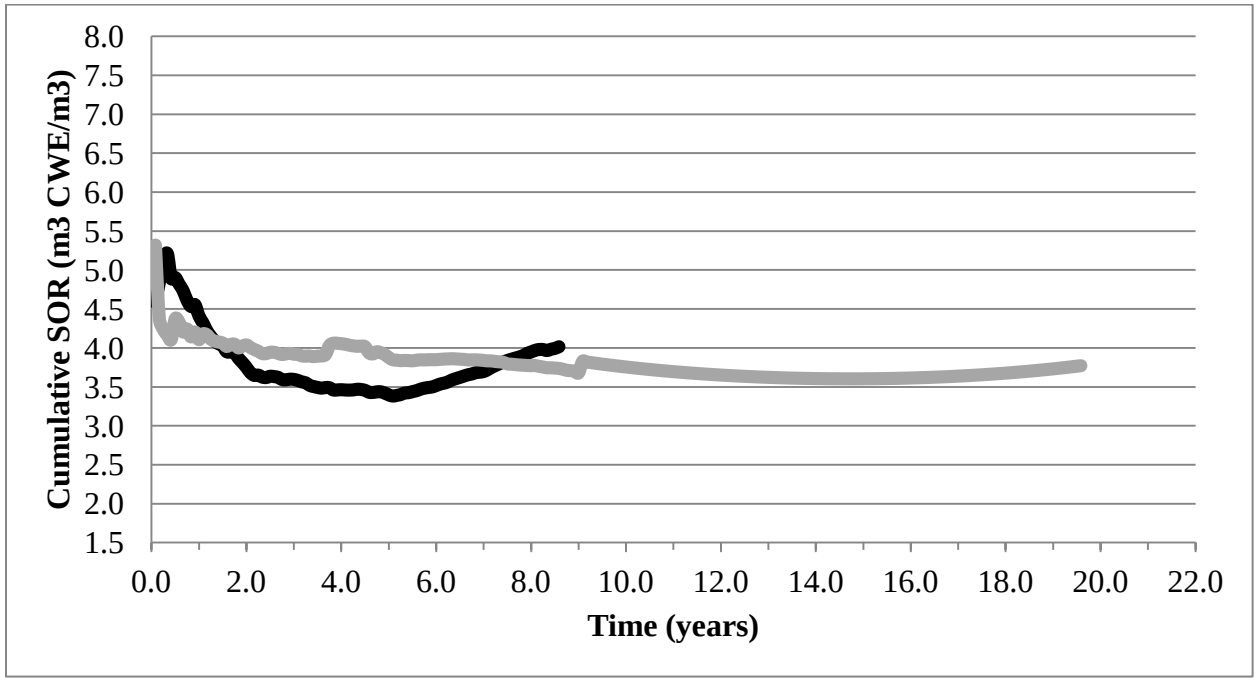

Figure 4.12.11: Comparison of cumulative steam oil ratio from steam injection model with historical values for Firebag Pad 102.

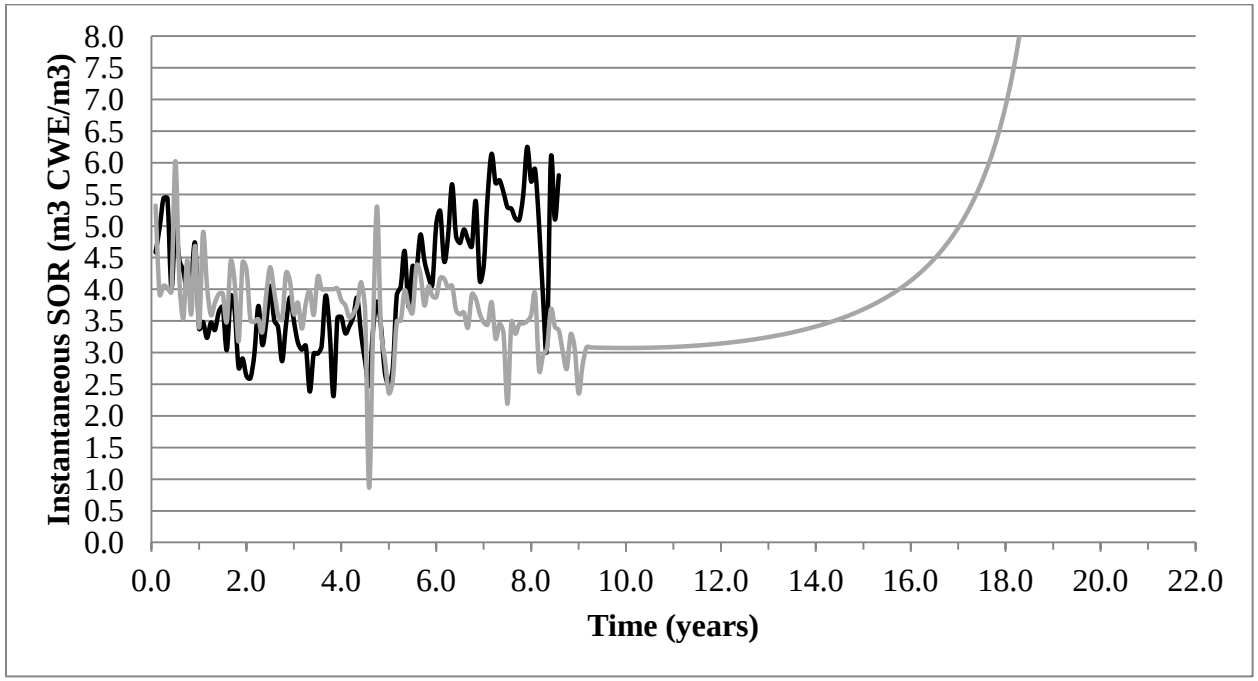

Figure 4.12.12: Comparison of instantaneous steam oil ratio from steam injection model with historical values for Firebag Pad 102.

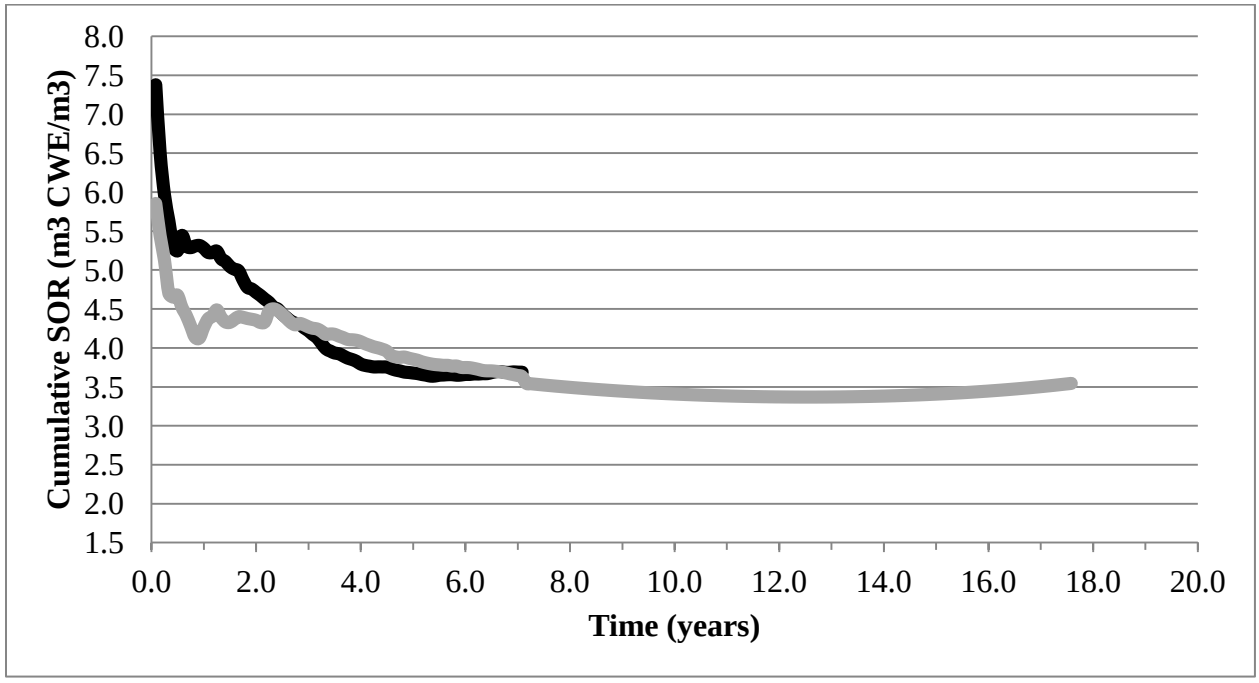

Figure 4.12.13: Comparison of cumulative steam oil ratio from steam injection model with historical values for Firebag Pad 103.

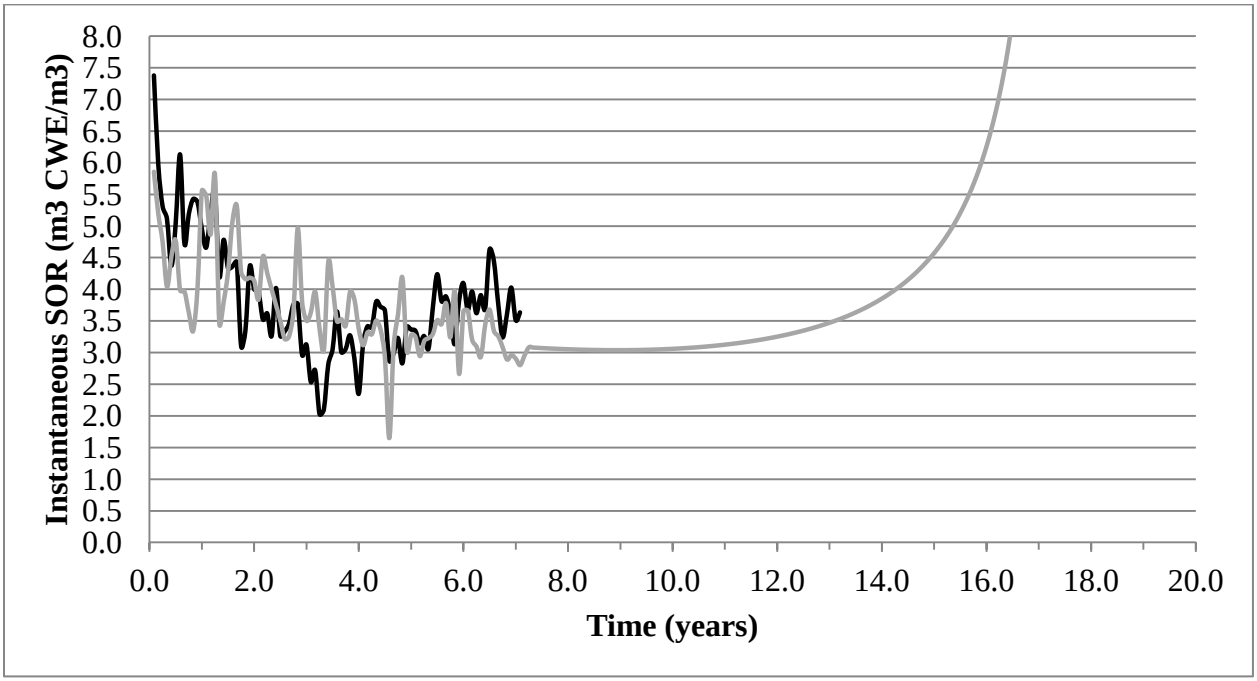

Figure 4.12.14: Comparison of instantaneous steam oil ratio from steam injection model with historical values for Firebag Pad 103.

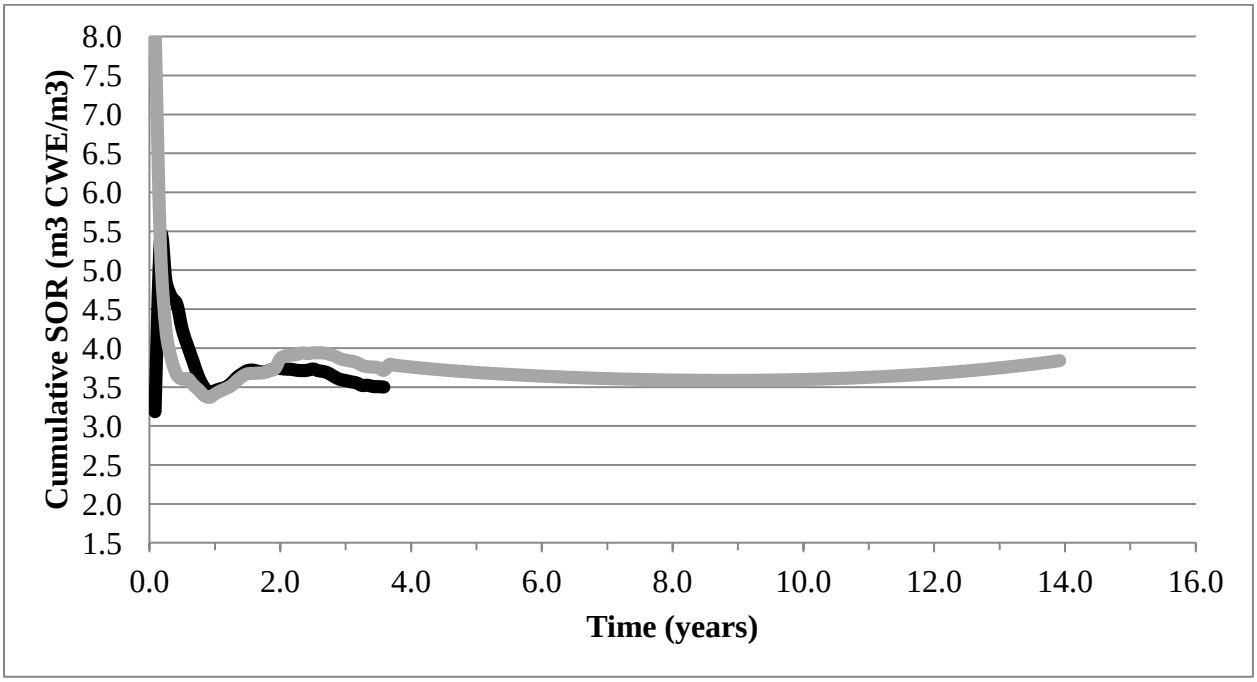

Figure 4.12.15: Comparison of cumulative steam oil ratio from steam injection model with historical values for Firebag Pad 104.

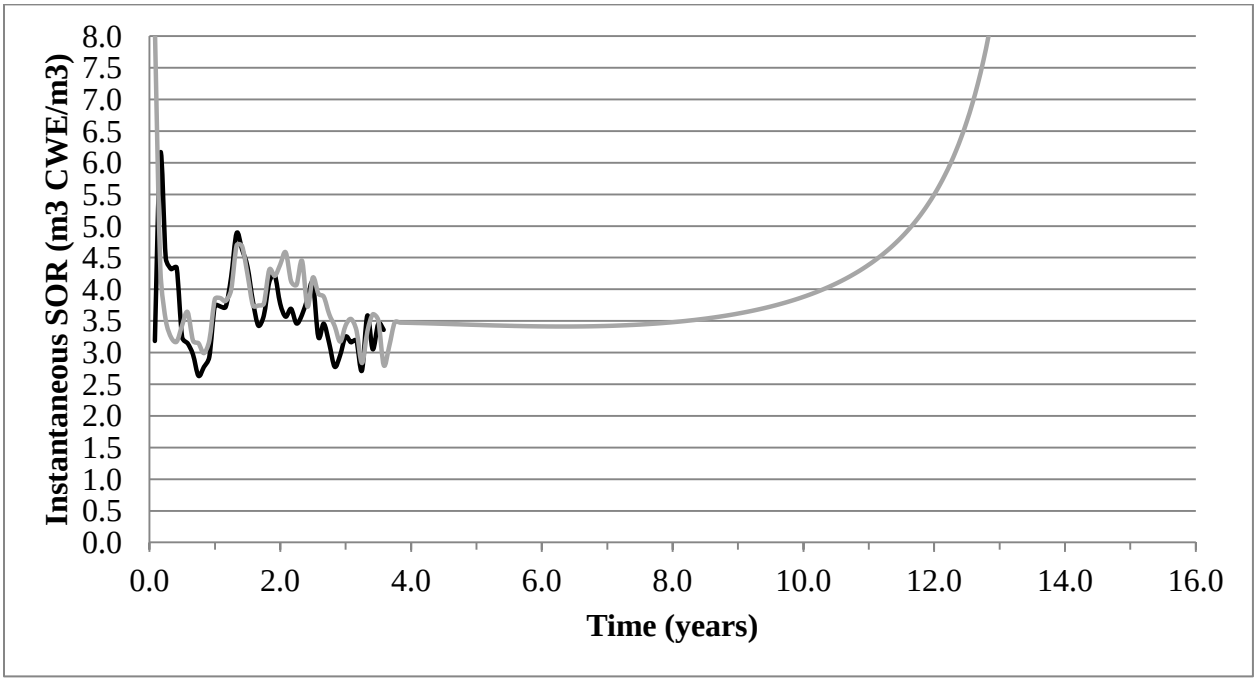

Figure 4.12.16: Comparison of instantaneous steam oil ratio from steam injection model with historical values for Firebag Pad 104.

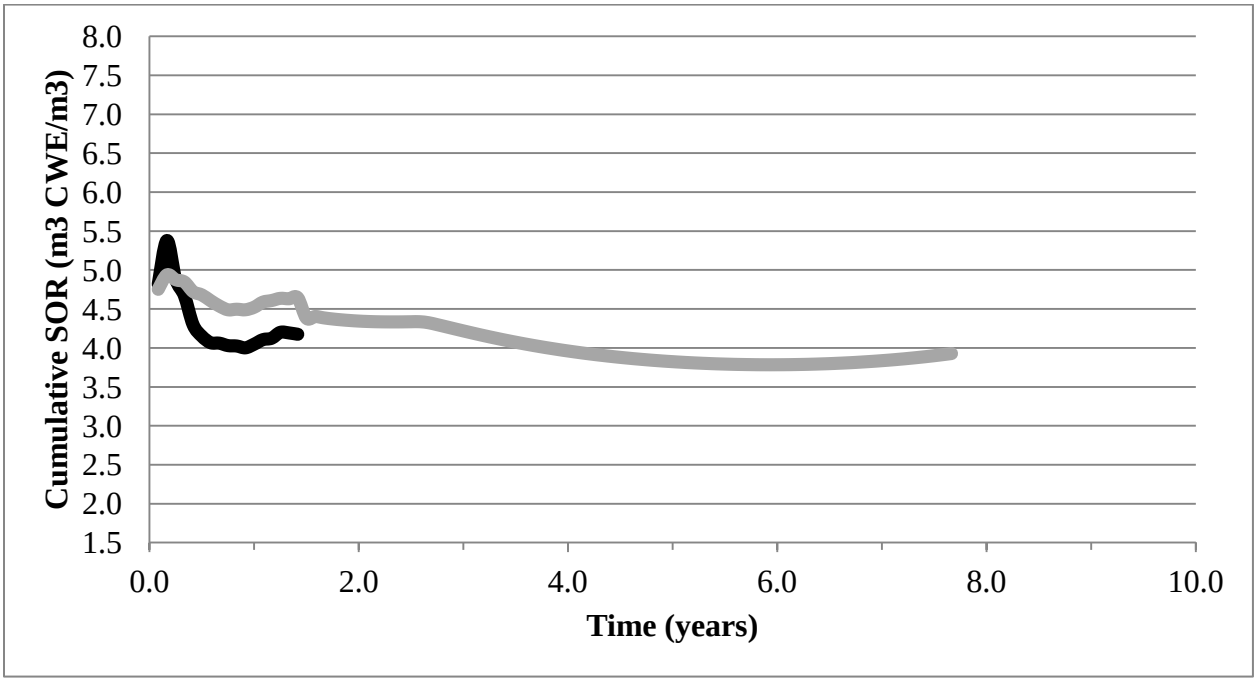

Figure 4.12.17: Comparison of cumulative steam oil ratio from steam injection model with historical values for Firebag Pad 107.

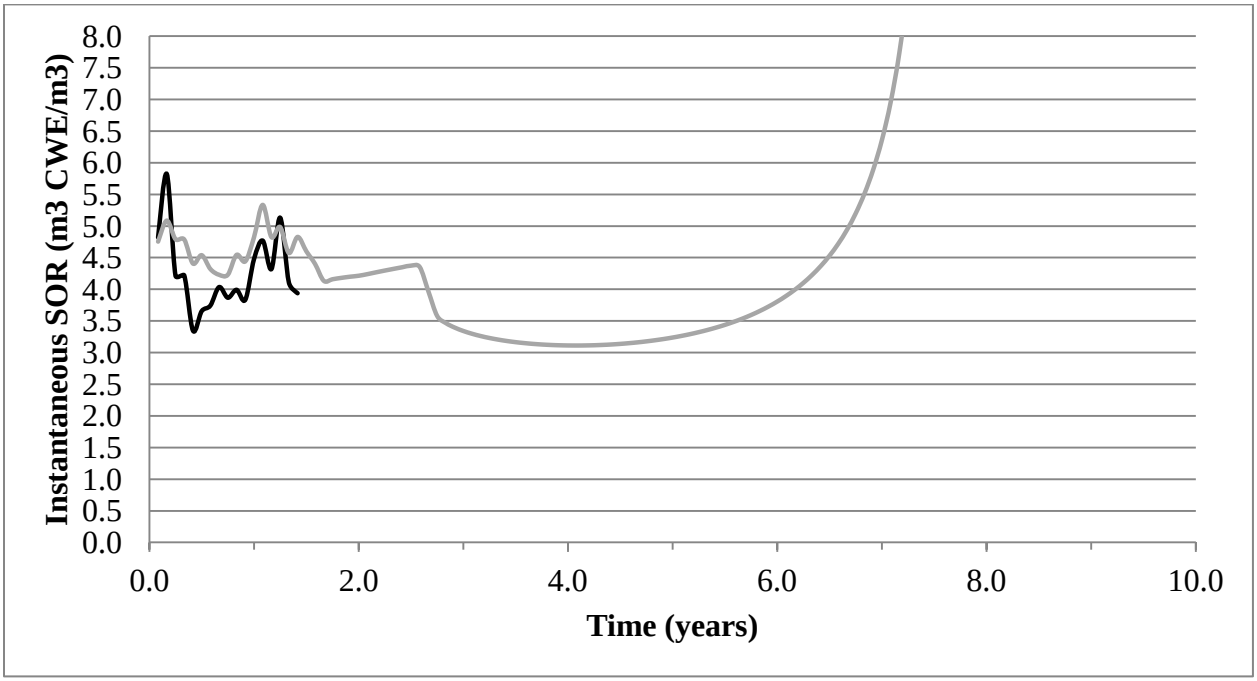

Figure 4.12.18: Comparison of instantaneous steam oil ratio from steam injection model with historical values for Firebag Pad 107.

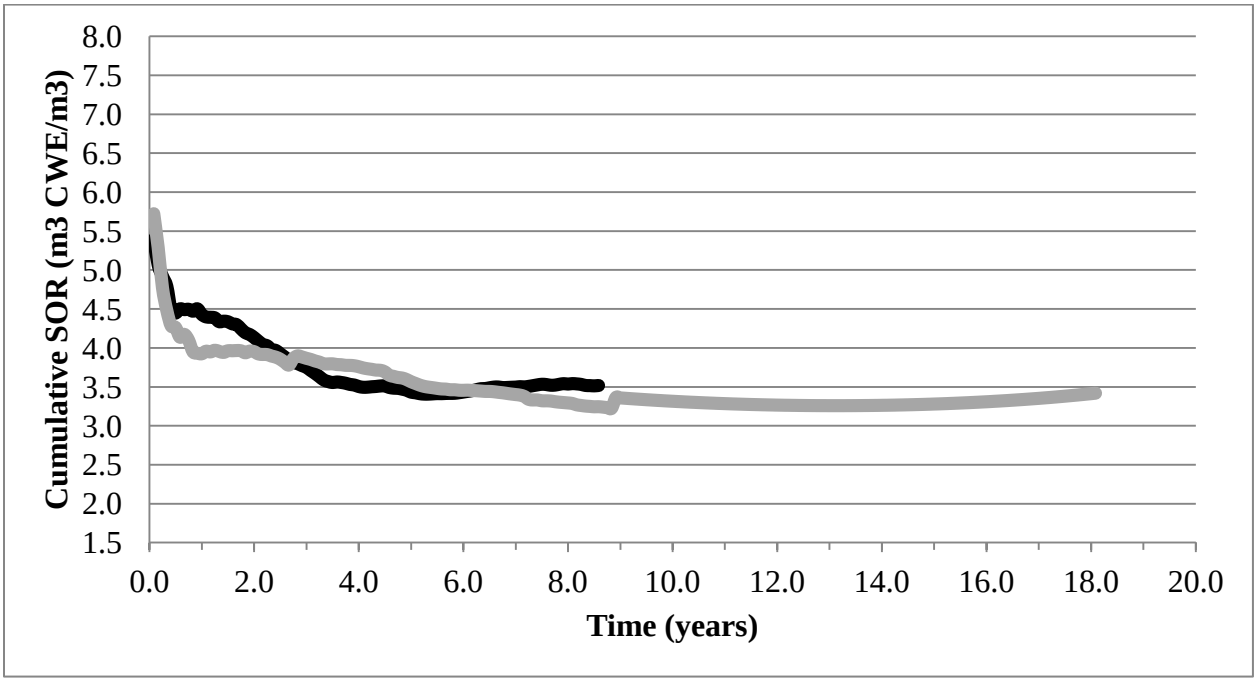

Figure 4.12.19: Comparison of cumulative steam oil ratio from steam injection model with historical values for Firebag northeast macro level steam chamber.

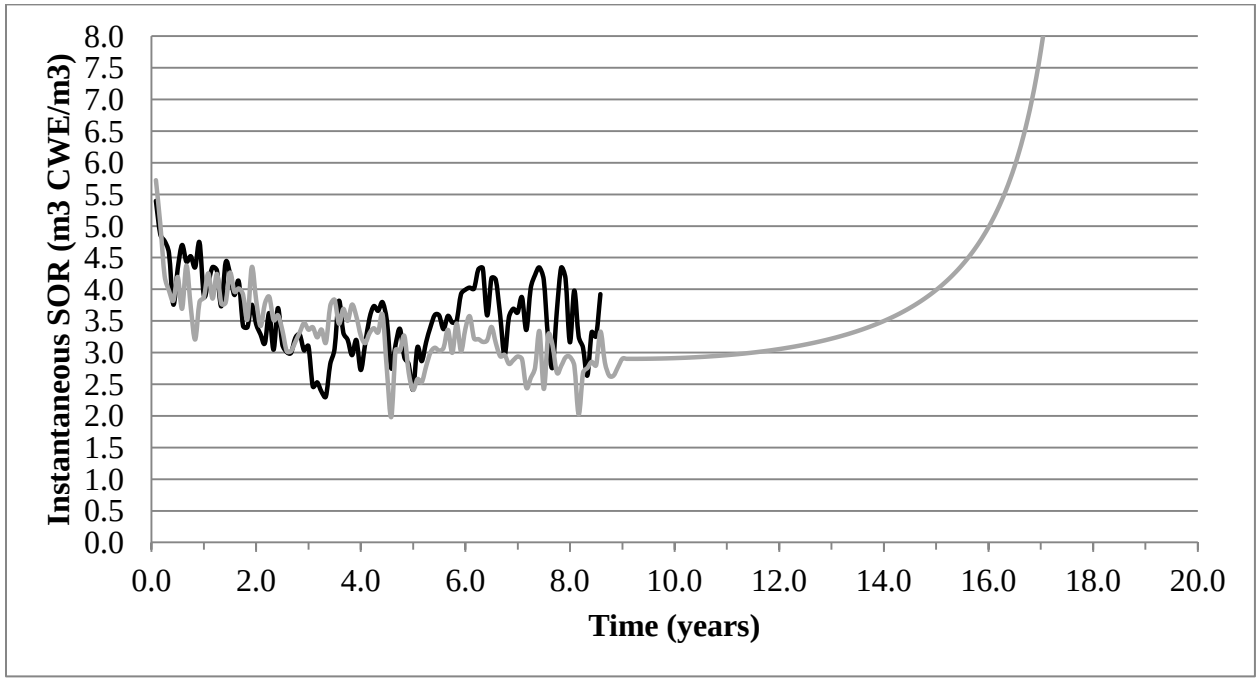

Figure 4.12.20: Comparison of instantaneous steam oil ratio from steam injection model with historical values for Firebag northeast macro level steam chamber.

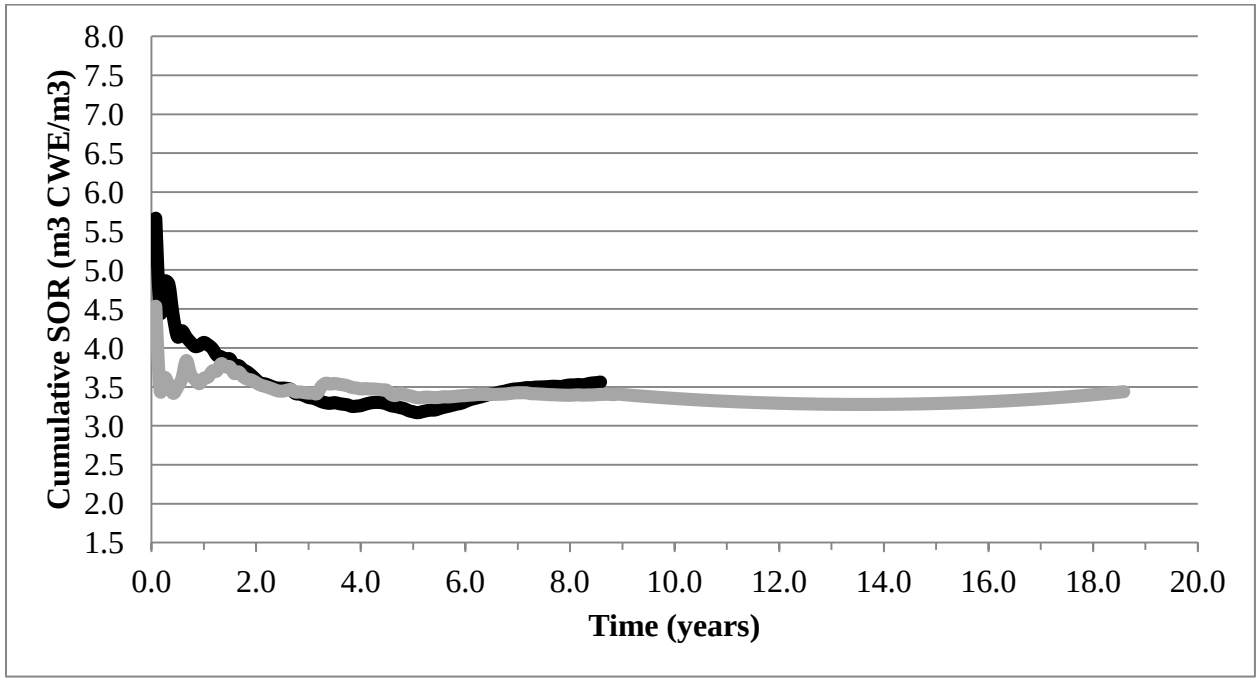

Figure 4.12.21: Comparison of cumulative steam oil ratio from steam injection model with historical values for Firebag south macro level steam chamber.

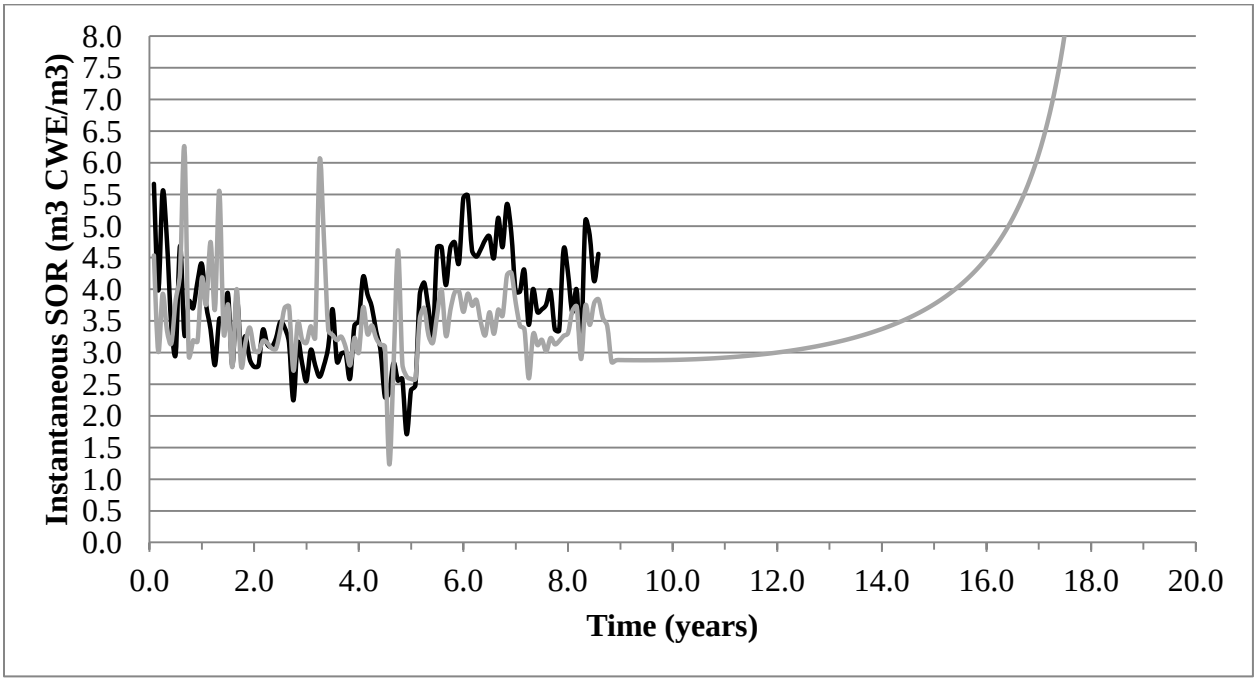

Figure 4.12.22: Comparison of instantaneous steam oil ratio from steam injection model with historical values for Firebag south macro level steam chamber.

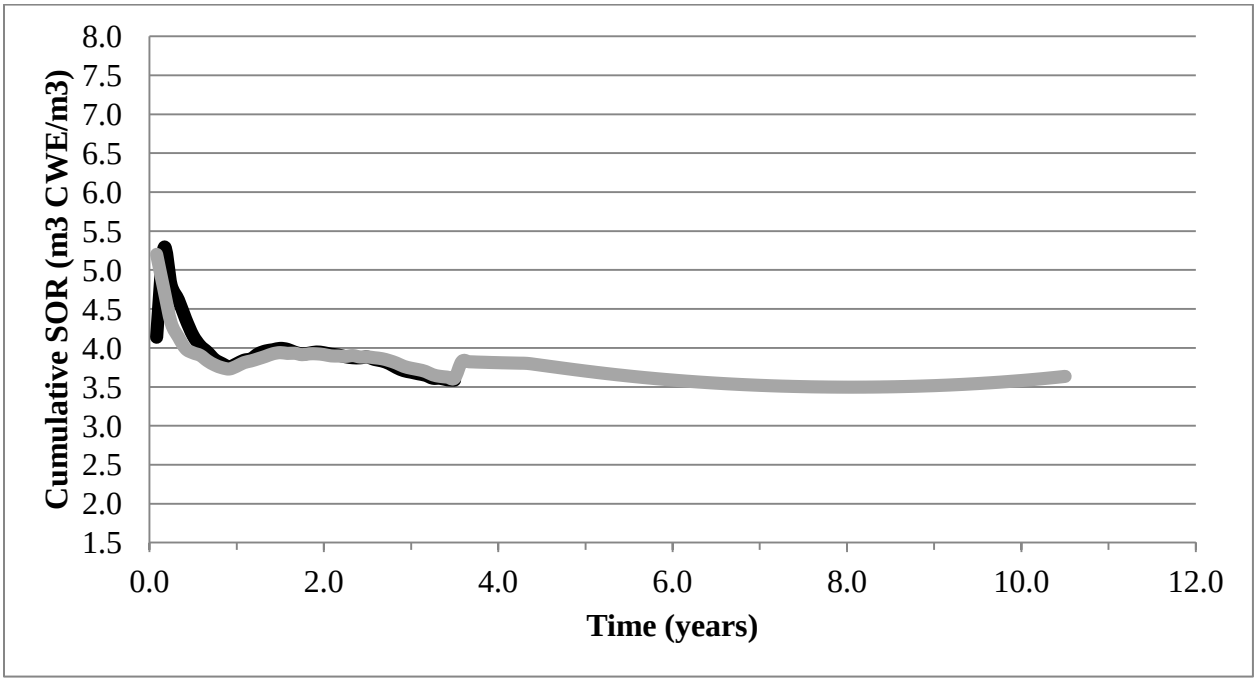

Figure 4.12.23: Comparison of cumulative steam oil ratio from steam injection model with historical values for Firebag west macro level steam chamber.

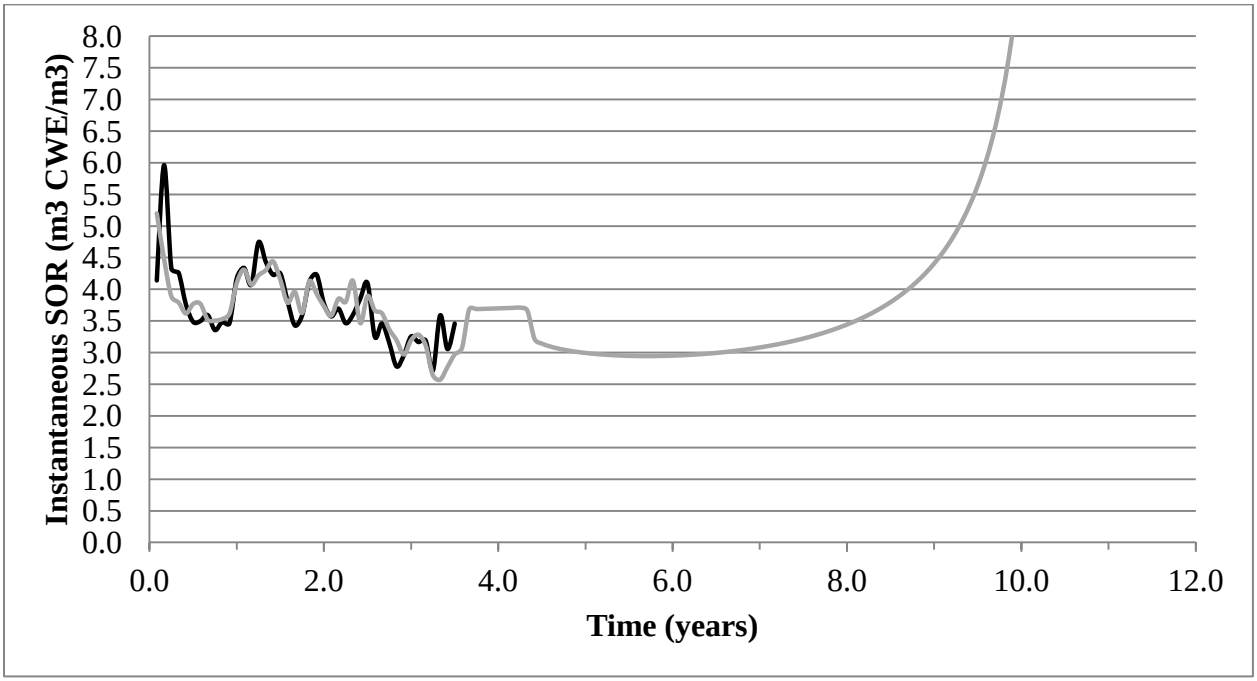

Figure 4.12.24: Comparison of instantaneous steam oil ratio from steam injection model with historical values for Firebag west macro level steam chamber.

CHAPTER 5: CONCLUSIONS AND RECOMMENDATIONS

An analytical model has been developed in this paper to predict SAGD performance. The novelty of the model used here lies in the use of extensive historical performance data from the Firebag SAGD operations to understand and quantify the analytical model parameters with the highest uncertainty. This link of the model parameters to log, core, lab, and seismic helps to increase confidence in the both the model input parameters and the model predictions.

Since there a large amount of actual oil production and steam injection data was available, there was a reasonably good understanding of what the outputs from the completed model should be. This allowed for the quantification of the model parameters with the highest amount of

uncertainty, which were effectively used as model calibration parameters. This provided insight into in-situ permeability and the amount of heat energy consumed by sources in the reservoir that are not well understood.

The oil drainage portion of the model was based on the model originally developed by Butler et al. (1981) with analytical equations to describe each of the three phases of SAGD – the initial rising chamber phase, the lateral chamber growth phase (LINDRAIN), and the depletion phase. Although these equations are based on experimental work, they have been shown in this work to be applicable, with adjustment and calibration, at a field level.

The analytical model for oil drainage prediction appears to be reasonably accurate in predicting oil drainage rates even though the model assumes that steady state heating occurs by conduction only. The additional heating by convection on the SAGD process is significant, however it has been shown (Sharma and Gates, 2011) that convection heating near the steam chamber interface actually has a negative impact on oil rate is due to relative permeability effects.

The steam consumption portion of the analytical model was based on the model originally developed by Reis (1992) in which the various components of heat consumption within the reservoir were considered in order to determine the steam injection requirements. These components included the heat consumption associated with the steam chamber expansion, the heat ahead of the steam zone, and the heat lost to the overburden.

Several simplifcations and enhancements to the Reis (1992) model were made by Edmunds and Peterson (2007) and Miura et al. (2010). Those changes which helped to improve the predictive capability of the SAGD process were also included in the current work. In addition, further improvements were made to the existing models in literature. The first was the calculation steam chamber shape factor based on a fluid material balance, instead of an assumed shape factor. The second was the improvement of the overburden heat loss calculation through the determination of steam chamber velocity as a function of time using 4D seismic.

In the development of the steam consumption model, it was found that the heat losses quantified in the existing models in literature significantly underestimate the steam requirements at Firebag. The additional heat loss term that was incorporated into the current model to account for the additional heat loss indicates that the underestimation of heat consumption was approximately equivalent to the calculated overburden heat loss.

The end result was a reasonably good match on steam injection rate as well as on the instantaneous and cumulative basis for the steam oil ratio in the field. The match was better when large-scale chambers (made up of multiple well pads) within the Firebag reservoir were considered which accounted for inter-chamber communication and fluid mobility between individual pads. This is an especially important consideration for steam since it has a much higher mobility in the reservoir than the liquid phases (oil and water).

Overall conclusions of this study are:

1. With the proper inputs and model calibration, a simple analytical model that honours the governing physics of energy balance, material balance, and gravity drive is sufficient to accurately predict the performance of the SAGD process.
2. Studies performed at a lab scale can vary considerably from actual field values. In this work, it is shown that values for residual oil saturation and chamber front velocity derived from 4D seismic analysis are significantly different at a field scale when compared to typical lab scale results.
3. There are significant heat losses that are not accounted for in existing models in literature, and these are postulated to be due to convection from mobile water, steam chamber development past the toes and heels of the wells, thermal inefficiencies due to non-pay facies in the reservoir, and heat losses to the underburden.
4. The model confirms that inter-chamber communication between pads needs to be taken into account in order to more accurately model SAGD performance.

Recommendations for future work include:

1. Further study to quantify the individual contributions for the heat loss term in the model. It is expected that major contributors would be the underburden heat losses and convection losses due to mobile water in the reservoir.
2. Updating the correlations used to determine residual oil saturation and chamber velocity as successive 3D seismic shots are available in the future in order to validate and refine the assumptions used in this model.
3. Understanding later life SAGD performance. The case study used to validate this model is based on the Suncor Firebag operation, which, based on cumulative recovery to date,

has several years of operation left in it's current pads. As this SAGD operation becomes more mature, the model should be tested against the late life performance to ensure that it is still valid.

4. Application of this model to other SAGD operations to ensure that it is robust enough to accurately predict the performance of reservoirs with different properties and operating conditions.

REFERENCES

Butler, R.M., McNab, G.S., and Lo, H.Y., Theoretical Studies on the Gravity Drainage of Heavy Oil During In-Situ Steam Heating, Canadian Journal of Chemical Engineering, Vol. 59, No. 4, August 1981.

Butler, R.M., Stephens, D.J., The Gravity Drainage of Steam-Heated Heavy Oil to Parallel Horizontal Wells, Journal of Canadian Petroleum Technology, p.90-96, (April-June 1981).

Butler, R.M., New Interpretation of the Meaning of the Exponent "m" in the Gravity Drainage Theory for Continuously Steamed Wells, Proc. 2nd World Cong. Chem Eng., 2, 430-433, (Montreal, Oct. 1981)

Butler, R.M., Rise of interfering steam chambers, Journal of Canadian Petroleum Technology, p.70-75 (May-June 1987)

Butler, R.M., Thermal Recovery of Oil and Bitumen; Gravdrain Inc., 1998

Cardwell, W.T. and Parsons, R.L., Gravity Drainage Theory, Trans. AIME 146 28-53 (1942).

Carslaw, H.S., and Jaeger, J.C., Conduction of Heat in Solids, Oxford Univ. press., p. 288, 1959.

Deutsch, C.V., "Estimation of Vertical Permeability in the McMurray Formation", Journal of Canadian Petroleum Technology, Vol. 49, No. 12, 10-18.

Doan et al., "Performance of the SAGD Process in the Presence of a Water Sand – A Preliminary Investigation", Petroleum Society, Presented at the 1999 CSPG and Petroleum Society Joint Convention, Digging Deeper, Finding a Better Bottom Line, in Calgary ,Alberta, Canada, June 1999.

Edmunds, N., "On the difficult Birth of SAGD", Journal of Canadian Petroleum Technology, Vol. 38, No. 1, 14-17.

Edmunds, N., Chhina, H., "Economic Optimum Operating Pressure for SAGD Projects in Alberta", Journal of Canadian Petroleum Technology, Vol. 40, No. 12, 13-17.

Edmunds N., Peterson, J., "A Unified Model for Prediction of CSOR in Steam-Based Bitumen Recovery", Petroleum Society, Presented at the 8th Canadian International Petroleum Conference, Calgary, Alberta, Canada, June 2007.

Energy Resources Conservation Board (June, 2012), "ST98-2012: Alberta's Energy Reserves 2011 and Supply/Demand Outlook 2012-2021", Retrieved February 11, 2013 from http://www.ercb.ca/data-and-publications/statistical-reports/st98

Farouq Ali, S.M., “Practical Heavy Oil Recovery”, Course Text for ENCH647 Thermal Recovery Methods, (October 2010)

Gotawala, D.R., Gates, I.D., “Steam Fingering at the Edge of a Steam Chamber in a Heavy Oil Reservoir”, The Canadian Journal of Chemical Engineering, Vol. 86, 1011-1022, December 2008.

Ito, Y., Suzuki, S., “Effect of Reservoir Parameter on Oil Rates and Steam Oil Ratios in SAGD Projects”, Presented at the 7th Unitar International Conference on Heavy Oil and Tar Sands, Beijing, China, October 1998.

Javad, S., Oskouei, P., Maini, B., Moore, R.G., Mehta, S.A., “Effect of Mobile Water-Saturation on Thermal Efficiency of Steam-Assisted Gravity-Drainage Process”, SPE Paper 138846, SPE Latin American & Caribbean Petroleum engineering Conference, Lima, Peru, December 2010.

Kato, A., Onozuka, S., Nakayama, T., “Elastic Property Changes in a Bitumen Reservoir During Steam Injection”. The Leading Edge 27 (9): 1158-1175. doi:10.1190/1.2978979, 2008.

Miura, K., Wang, J., “An Analytical Model to Predict Cumulative Steam Oil Ratio in Thermal Recovery SAGD Process”, Presented at the Canadian Unconventional Resources & International Petroleum Conference, Calgary, Alberta, Canada, October 2010.

Nasr, T.N., Law, D., Golbeck, H., Korpany, G., “Counter-current Aspect of the SAGD Process”, Petroleum Society, Presented at the 49th Annual Technical Meeting of the Petroleum Society in Calgary, Alberta, Canada, June 1998.

Reis, J.C., “A Steam-Assisted Gravity Drainage Model for Tar Sands: Linear Geometry”, Journal of Canadian Petroleum Technology, Vol. 31, No. 10, December 1992.

Sharma, J., Gates, I.D., “Convection at the Edge of a Steam-Assisted-Gravity-Drainage Steam Chamber”, SPE Journal, September 2011, Pgs 503-512.

Somerton, W.H., “Some Thermal Chracteristics of Porous Rocks,” Trans. AIME, 213 (1958) 275.

Su, Y., Wang, J., and Gates, I.D. SAGD Well Orientation in Point Bar Oil Sands Deposit Affects Performance. Engineering Geology, 157:79-92, 2013.

Sun, F., Personal Communication, September 26, 2012.

Suncor Energy, (May 15-16, 2012). “Suncor Firebag 2012 ERCB Performance Presentation Commercial Scheme Approval No. 8870”. Retrieved February 9, 2013, from http://www.ercb.ca/data-and-publications/activity-and-data/insitu-progress

Suncor Energy, (May 4-5, 2011). “Suncor Firebag 2011 ERCB Performance Presentation Commercial Scheme Approval No. 8870”. Retrieved February 12, 2013, from http://www.ercb.ca/data-and-publications/activity-and-data/insitu-progress

Suncor Energy, (May 11-12, 2010). “Suncor Firebag 2010 ERCB Performance Presentation Commercial Scheme Approval No. 8870”. Retrieved February 12, 2013, from http://www.ercb.ca/data-and-publications/activity-and-data/insitu-progress

Tanaka, M., Endo, K., Onozuka, S.: “Estimation of Steam Chamber Extent Using 4D Seismic”, Journal of Canadian Petroleum Technology, Vol. 49, No. 5, May 2010.

The Oil Sands Developers Group. (2013). Steam Assisted Gravity Drainage. Retrieved from http://www.oilsandsdevelopers.ca/index.php/oil-sands-technologies/in-situ/the-process-2/steam-assisted-gravity-drainage-sagd/

Tikhomirov, V.M., “Thermal Conductivity of rocks, and Its Relation to the Liquid Saturation, Density, and Temperature”, Neftyanoe Khoz., 46 (April 1968) 36.

Walls, E., Palmgren, C., Kisman, K., “Residual Oil Saturation Inside the Steam Chamber During SAGD”, Journal of Canadian Petroleum technology, Vol. 42, No. 1, 39-47, January 2003.

Vanegas, J.W., Deutsch, C.V., Cunha, L.B.: “Uncertainty Assessment of SAGD Performance Using a Proxy Model Based on Butler’s Theory, SPE, Presented at the 2008 SPE Annual Technical Conference and Exhibition, Denver, Colorado, USA, September 2008.

Zhang W., Youn, S., Doan, Q.: “Understanding Reservoir Architectures and Steam-Chamber Growth at Christina Lake, Alberta, by Using 4D Seismic and Crosswell Seismic Imaging”, SPE Reservoir Evaluation & Engineering, October 2007, Pgs 446-452.